Variation of the Electronic Functionality of Self-Seeded Germanium Nanowires Through Synthesis Determined Core-Shell Interface States

Stephen Connaughton

A thesis submitted to the University of Dublin, Trinity College,

in application for the degree of *Doctor of Philosophy*

School of Physics

Trinity College Dublin
2015

Declaration

I declare that this thesis has not been submitted as an exercise for a degree at this or any other university and it is entirely my own work.

I agree to deposit this thesis in the University's open access institutional repository or allow the Library to do so on my behalf, subject to Irish Copyright Legislation and Trinity College Library conditions of use and acknowledgment.

_____

Stephen Connaughton

To Maureen and Michael Connaughton

Acknowledgements

Firstly I would like to thank my supervisor Professor Vojislav Krstić for all that he has taught me over the past 5 years. I would also like to thank Professor John Donegan for his help at the end of my project.

Collaboration is vital in any Ph.D, and especially in this one as I relied on others to provide samples for me. For this reason I would like to sincerely thank Dr. Richard Hobbs, Dr. Olan Lotty and Prof. Justin Holmes. In addition of course I did not work in isolation within the group. Niall Kinahan, Tarek Lutz, Stefan Hansel, Peter Gleeson and Maria Koleśnik all gave me invaluable help during my first years. Great thanks also goes to Olga Varona of Intel, who worked on this project with me for several months. In later years I must thank Eleanor Holmes and Akshara Verma in particular for the regular bitchin' coffee. A lot of my time in CRANN has been taken up with setting up/fixing/maintaining the machines, and for that Mike Finneran has always offered constant and indispensable help. Finally I am very grateful to Kyle Ballantine, my Mathematica guru.

Great thanks goes to Sinéad, without whose support the past 5 years would have been unbearable, and without whose help this thesis may never have been submitted. I also must thank my parents, Michael and Maureen, who have seen me through 22 long years of school. Perhaps I will get a real job soon. When I think back on my years as a Ph.D. student I will of course always be reminded of José Caridad, who was my collaborator, colleague and friend. I learned a lot from you both in the lab and the pub, much of it still baffling.

Kind thanks goes to various others who have been friends over the years. In particular I would like to thank Brendan and Zara for many fun nights and parties, simply too many to remember. There are some ex-members of the group that I have not yet thanked, but they are certainly not forgotten. Firstly James: I would like to thank you for all of your help as we tried to work out what we were doing in the early days and for the uncountable good memories since the first year of undergrad. The Dooleyfests have been a highlight of the past 5 years. Of course I also couldn't mention those trips without also thanking Rónán and the eponymous Dooley. To Andrea a.k.a Dj Pani: there are many great nights to thank you for, but I would especially like to thank you and Canly for your hospitality during our trip to Milan. The group was a lot more fun with Robert "prime" in it. I hope that we may find ourselves working together again soon. I feel like I have been accepted as an honorary member of the Duesberg group over the past 2 years. Thanks must therefore go to Toby and Nina especially for the Halloween parties, Niall for the small inland ocean of beer I must owe you, Maria for the various baked goods, Hugo for always bigging up the Bray massive, Kay and Hye-Yong for the house parties and dancing lessons, and also to Christian, Riley, Chanyong and Ehsan. Finally of course thanks to Georg himself for the many stories.

Very special thanks must go to others in CRANN and AML, who have helped to make my time here enjoyable and fruitful. I would like to especially mention, Ciarán Fowley, Darragh Crotty, Sandip Battacharya, Alan Bellew, Dave McCloskey and Chris Murray for the many laughs inside and outside the lab and Kiril Borisov for helping to ensure that I didn't end up jobless.

Knowing me there are people that I have unfortunately forgotten to mention. If you find that you are in this latter group I am sorry. There were quite simply too many people to recall all of them. Please feel free to call, e-mail, harass and harangue me for my oversight.

Table of Contents

Table of Figures

List of Tables

Summary

Bottom up grown germanium nanowires may have an important role to play in future electronic devices. While the electrical properties of nanowires grown using a metallic seed as a catalyst have been extensively reported we study self-seeded nanowires in this thesis. Such wires are core-shell in nature and are grown without any intentional doping. Self-seeded nanowires have been previously proposed as an attractive alternative to conventionally grown wires due the alleviation of complications arising from unintentional doping from the metallic seed. The results in this thesis demonstrate that the electrical properties of the self-seeded, core-shell nanowire are dominated by doping from the interfaces states which is in turn dependent on the details of the nanowire growth.

We first examine the room-temperature electrical properties of two sets of wires grown under different growth conditions. A significant difference in electrical behaviour was seen. One batch showed a *p*-type gate response and memristive behaviour, while the other showed little or no gate effect, and low resistivity. It is proposed that the observed behaviour results from differences in the density of the charge traps located at the interface between the core and the shell of the nanowire, leading to a difference in the nanowire doping. The difference stems from a change in the structural and chemical properties of the shell which is caused by the altered growth conditions. A model is developed in this thesis to explain how the interface states lead to the observed memristive behaviour. In contrast a high density of surface states leads to the observed gate voltage invariance and low resistive response.

We then examine the change in resistivity with nanowire diameter. A complicated experimental relationship is found. The resistivity falls by more than an

order of magnitude as the diameter is lowered from 40 nm to 20 nm. After this a monotonic relationship is no longer seen. Instead a peak-like feature is measured at a diameter of approximately 14 nm. The results are modelled and two separate regimes are found. Above diameters of 20 nm the mobile holes in the wire are confined to an annular region close to the surface of the wire due to the electrostatic attraction of the electrons in the interface states. In this region we model the change in resistivity as resulting from the change in the carrier concentration arising from the difference in scaling between the surface of the wire and the volume of the annular region to which the mobile holes are confined. Below 20 nm diameters we model the mobility using the one-dimensional Kubo-Greenwood formula. Unlike previous applications of this formula to nanowires we take into account explicitly the effects of the aforementioned diameter dependent carrier concentration arising from the surface state doping. The peak-like feature is reproduced by the theory.

Finally we examine the temperature dependence of the nanowires. It is found that most of the nanowires display Efros-Shklovskii variable range hopping conduction due to the mobile holes hopping from one trapped electron to another. From this we extract the surface state density and find excellent agreement with previous results. The most highly conducting wires display a range of metallic and dirty-metal behaviours at different temperature ranges.

1. Introduction

1.1 Historical context

Since the development of the transistor by John Bardeen, Walter Brattain and William Shockley at Bell labs in 1947 semiconductor technology has become central to almost every facet of life. The original transistor was a point contact bipolar junction transistor (BJT), an image of which is shown in Figure 1.1 (a), which was built using a crystal of *n*-type germanium [1]. Germanium was the focus of much of the early work due to its superb electrical properties. At room temperature the mobility of holes in bulk germanium, 1900 $cm^2V^{-1}s^{-1}$ [2], is the highest of any semiconducting material [3]. It is more than 4 times the value in silicon of 450 $cm^2V^{-1}s^{-1}$ [2]. The electron mobility in germanium is 3900 $cm^2V^{-1}s^{-1}$, which is 2.5 times the value in silicon of 1500 $cm^2V^{-1}s^{-1}$

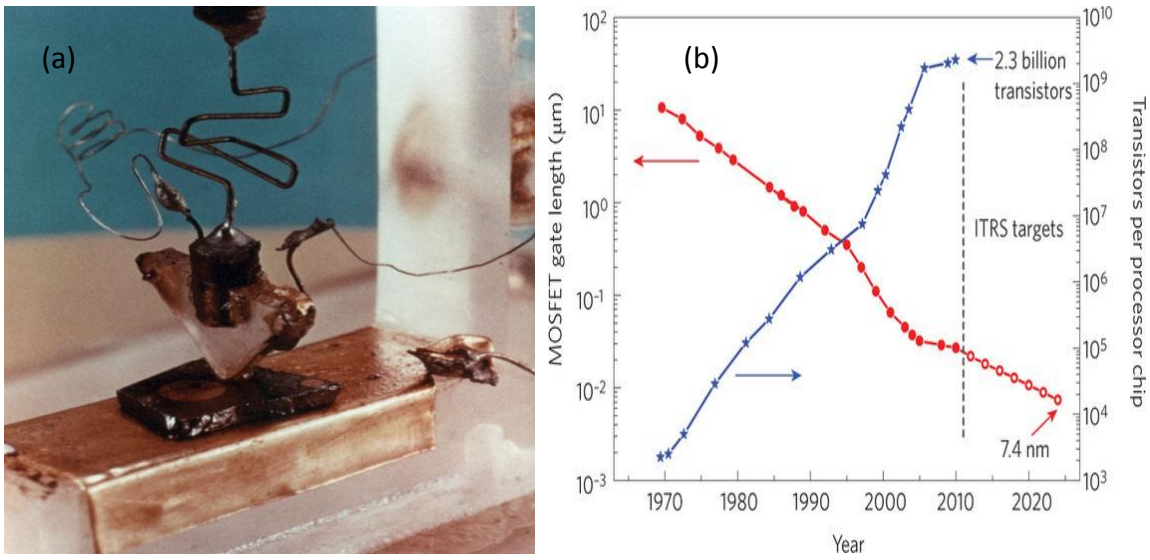

Figure 1.1 (a) A picture of the first transistor ever made. (b) A graph depicting Moore's law. In (a) the germanium is the dark material sitting directly under the semi-transparent triangle. Either side of the triangle is covered in a thin film of gold, which has a small gap made in it at the apex of the triangle. The two gold sides are the emitter and collector contacts. At the top of the insulating triangle a spring can be seen which pushes the contacts into the germanium. Underneath the germanium is the metallic gate. (b) shows two versions of Moore's law. The blue line shows the number of transistors on a single processor chip and the red line shows the gate length of a device from 1970 to 2010. Data points after that are projections. The change in the rate of increase of the number of transistors per chip in 2005 is associated with the introduction of hafnium oxide and the move from geometric to equivalent scaling

[2]. In spite of this it is silicon that dominates the semiconducting industry today. The group led by Shockley in Bell labs were originally trying to create a field-effect-transistor (FET) [1], a design concept patented as early as 1921 by Julius Edgar Lilienfeld [4]. The first attempts to make such devices proved unsuccessful. This was due to the fact that there exists at the surface of silicon and germanium states that trap mobile electrons and screen out the applied electric field [5]. It was this insight by Bardeen that led the group to develop the point contact BJT, which in fact relied on the existence of such states to operate [1].

The great breakthrough for silicon came in 1959 when it was discovered that a thermally grown layer of silicon dioxide greatly reduced the number of charge traps at the silicon surface [6]. This allowed the development of the first working field effect transistor, the metal-oxide-semiconductor field effect transistor (MOSFET), which was patented in the following year [7]. A thermally grown layer of germanium oxide did not passivate the surface, and so was unsuitable for use in MOSFETs. As MOSFETs were cheaper and easier to produce in integrated circuits than other transistors they became dominant and so too did silicon [8], a fact that remains true to this day.

There are indications that silicon may soon fall out of favour due to the relentless drive towards the miniaturisation of transistors. As famously pointed out by Moore in 1965 [8] the size of a transistor halves approximately every 18 months[1]. This trend has continued for almost 50 years, as shown in Figure 1.1 (b). This shrinking brought many benefits. Smaller devices were cheaper due to the fact that more could

[1] In fact Moore originally stated: “The complexity for minimum component cost has increased at a rate of a factor of two per year… Certainly over the short term this rate can be expected to continue, if not to increase” We state 18 months here as this is how it is now normally presented as it has proven to be the case over the longer term.

be fit onto a single chip, and they were faster for the simple reason that it took less time for a charge carrier to traverse the distance from the source to the drain electrode. Transistors followed this trend until about the year 2000, a period of time the international technology roadmap for semiconductors (ITRS) refers to as the “era of geometric scaling” [9]. After this time continued scaling by simply shrinking device lengths was no longer feasible, and we entered an era of “equivalent scaling” [9]. That is to say that the underlying transistor design was changed to bring in device performance enhancements. In the near future this may include changing the channel material from silicon to a high mobility material, such as germanium.

One area that has already undergone significant redesign is the gate oxide. By 2006 the gate dielectric was approximately 1.2 nm thick. Further scaling beyond this was not possible without unacceptably large leakage currents, due to the fact that electrons could tunnel through such a thin barrier. Therefore transistors chip manufacturers changed to using materials with a higher dielectric constant, such as hafnium oxide [10]. $Hf0_2$ has a dielectric constant of 25 [11] compared to 3.9 in SiO_2 [12], allowing gate control to be maintained with a thicker oxide and was introduced to commercial devices in 2007 by Intel [13]. Germanium nanowire devices with HfO_2 dielectrics have already been demonstrated, further suggesting that germanium may be utilised in future electronic devices [14].

Another major challenge facing the semiconductor industry is lithography. Extreme ultraviolet lithography has been described as the “official hope” of the industry, but it is not clear that the traditional top-down approach to making devices will continue to be cost effective for much longer [9]. Instead the ITRS roadmap

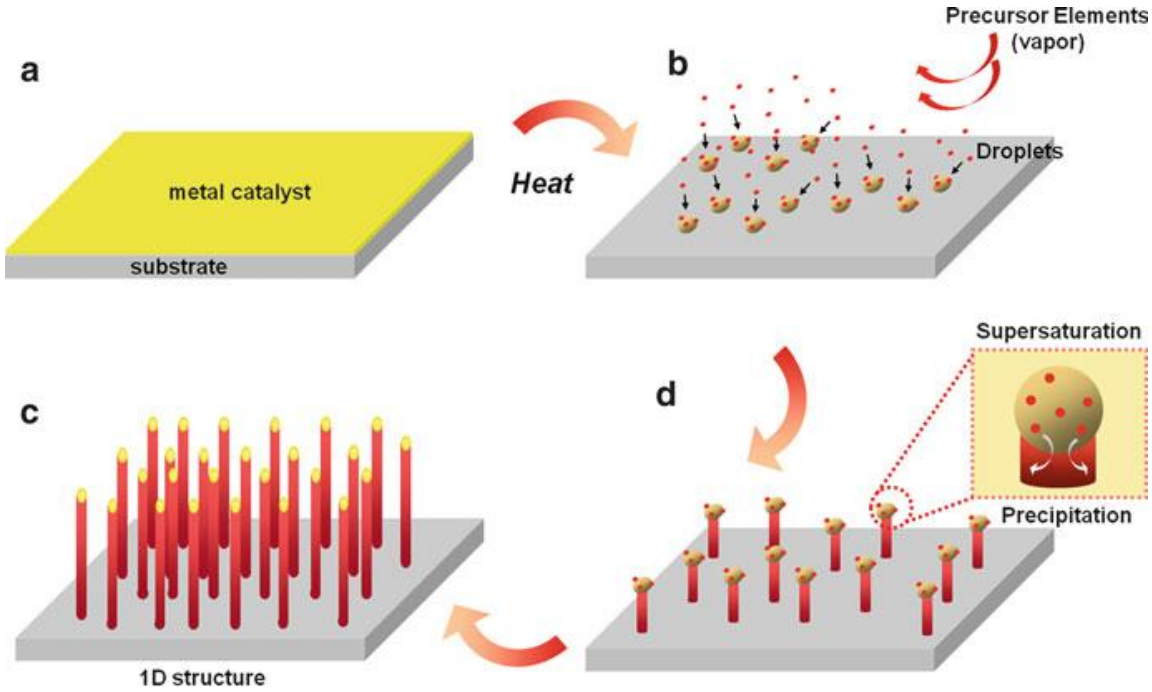

Figure 1.2 Schematic illustration of the VLS process. First a thin film of the seed material is deposited on the substrate, as shown in **a**. This is heated so that the catalyst melts and form liquid droplets. The precursor gas is passed over the substrate. This is shown in **b.** The precursor becomes incorporated into the droplet. A supersaturated solution is formed, causing the precursor to precipitate out, as shown in the inset of **d.** The precipitated precursor solidifies into a nanowire, which grows out from the seed, leading to nanowires capped with the seed catalyst as shown in **c** and **d.**

suggests that bottom up grown high mobility nanowires may be needed to continue device scaling after 2021 [9].

These technological challenges in the semiconductor industry have spurred research into the growth and characterisation of semiconducting nanowires [15, 16]. This has of course included work on field effect transistors [17-23], but it has also been suggested that nanowires may find a use in optoelectronic [15, 24-28], chemical sensing [15, 29-31] and spin based applications [32-35], for example. In addition the hard confinement of carriers in these structures allow the study of fundamental quantum effects, such as quantised conduction [36, 37] and coulomb blockade [38].

1.2 Germanium nanowires

Chemically derived semiconducting nanowires are most commonly grown using the vapour-liquid-solid (VLS) mechanism and its related derivatives such as vapour-solid-solid and solution-solid-solid. VLS growth was first described in 1964 [39] to explain the growth of silicon whiskers with diameters of the order of microns. In the 90s it was suggested that this mechanism could be used to grow wires with nanoscaled diameters [40, 41]. The starting point of growth for a nanowire using this technique is a metallic seed on the substrate, frequently gold. The substrate is then heated and a gas containing the desired nanowire material is flowed through the chamber. The metallic particles liquefy and absorb the seed material from the vapour until a supersaturated mixture is formed from which the semiconductor precipitates. This is shown schematically in Figure 1.2, which is taken from [42]. The advantage of this technique is that it allows growth of nanowires of a wide range of materials, and allows size control of the nanowires by control of the initial seed diameters and growth times. To make functional nanowire devices it will be necessary to control the doping of the nanowires. This can in principle be achieved by incorporating dopant atoms into the precursor gas from which the nanowire is grown [42]. This is however complicated by the fact that the number of dopants in a wire, N has a standard distribution of $\sqrt{N}$ [43]. For a 10 nm × 10 nm × 1 μm wire with a nominal doping of 10^{18} cm^{-3} this represents a margin of error of 10 %. This can result in unwanted variation in the device parameters such as the threshold voltage [43]. Furthermore dopants in the channel can act as scattering centres impeding channel mobility. It has therefore been suggested that the best doping profile for a nanowire is to confine the dopants to an atomic layer at the surface of the nanowire, a scheme known as delta doping (δ-doping) [44, 45]. The

careful control of the doping is complicated in the case of VLS grown wires due to the fact that seed atoms become incorporated either into or onto the nanowire and can cause unintentional doping [46-52].

A further complication is the surface states that plagued early research into field effect transistors. Due to the high surface to volume ratio of a nanowire these surface effects can dominate the electronic properties of the nanowires. This problem is especially acute in the case of germanium wires due to the high density of surface states – 10^{14} cm^{-2} as compared to 10^{12} cm^{-2} for silicon for example [53].

As a result there has been a lot of effort put in to determine if the observed electrical properties of germanium nanowires are due to the intentional dopants, unintentionally incorporated seed atoms or surface states. Hanrath *et al*. [54] grew nominally intrinsic Ge nanowires using a Au seed. The wires showed *p*-type behaviour when a gate was applied, which was attributed to doping from electron traps at the surface of the wire. Doping from the Au seed was not ruled out however. Wang *et al.* [14] demonstrated the difference in band bending, electrical response and Fermi level pinning in *n*-doped and *p*-doped wires grown by a VLS method, which they attribute to the presents of surface states. Zhang *et al*. [46] attempted to quantify the relative influence of surface states in Au seeded VLS grown wires and bulk impurities using atom probe tomography. They grew *n*-doped, nominally intrinsic and surface state enhanced wires. It was demonstrated that the surface traps played a major role in the electrical properties, with the *n*-doped samples showing reduced conductivity with respect to the intrinsic samples due to electrons becoming trapped at the interface. From an estimation of the mobility in their wires they calculated the total number of

occupied surface states to be of the order of 10^{11} - 10^{12} cm^{-2} for an intrinsic wire. However, the effect that the difference in growth conditions had on this density was not discussed.

In this thesis we circumvent the issues arising from dopants by using intrinsic, seedlessly grown germanium nanowires. This allows us to determine the role that surface states play in the electronic properties of nanowires with diameters in the range from 10 – 40 nm. This thesis demonstrates that the surface states in self-seeded nanowires determine the electrical properties completely and furthermore that a change in the growth conditions alters the details of the interface and so impacts majorly on the electrical properties. In Chapter 2 we will detail the theoretical background of electronic transport in semiconducting nanowires as well as the theoretical background of the effects we see such as memristance and variable range hopping transport. In Chapter 3 we will describe the nanowire material that we measure in more detail and describe our experimental set up. Chapter 4 will show the results of electrical measurements of wires at room temperature and compare and contrast the results from wires grown under different conditions. We will show that the wires show either *p*-type doping and memristance or a quasi-metallic behaviour. A model for the specific memristive response that we observe in our wires will also be developed in this chapter. Chapter 5 will discuss the diameter dependence of the resistivity of quasi-metallic nanowires. A non-monotonic relationship is found. The results are modelled taking into account the variation in carrier concentration arising from the difference in scaling of the surface and the volume. The change in mobility is modelled using the Kubo-Greenwood formula for wires with diameters below 20 nm. Chapter 6 will show the temperature dependence of these wires. We find that the high

resistance wires with a gate effect show variable range hopping behaviour, while the low resistivity samples show quasi-metallic behaviour in agreement with the results of Chapter 4. Finally Chapter 7 will be present the conclusions and discuss future work.

References

[1] J. Bardeen, Semiconductor research leading to the point contact transistor, Great Solid State Physicists of the 20th Century, (2003) 234.
[2] S.M. Sze, Semiconductor Devices: Physics and technology, John Wiley & Sons, New York, 2002.
[3] R. Pillarisetty, Academic and industry research progress in germanium nanodevices, Nature, 479 (2011) 324-328.
[4] J.S.E. LILIENFELD, Method and apparatus for controlling electric currents, in, Google Patents, America, 1930.
[5] J. Bardeen, Surface States and Rectification at a Metal Semi-Conductor Contact, Physical Review, 71 (1947) 717-727.
[6] M.M. Atalla, E. Tannenbaum, E. Scheibner, Stabilization of Silicon Surfaces by Thermally Grown Oxides*, Bell System Technical Journal, 38 (1959) 749-783.
[7] K. Dawon, Electric field controlled semiconductor device, in: U.P. Office (Ed.), USA, 1963.
[8] G.E. Moore, Cramming more components onto integrated circuits, in, McGraw-Hill New York, NY, USA, 1965.
[9] I. Roadmap, International Technology Roadmap for Semiconductors, 2013 edn, Executive Summary. Semiconductor Industry Association, (2013).
[10] A. Huang, Z. Yang, P.K. Chu, Hafnium-based high-k gate dielectrics, Advances in Solid State Circuits Technologies, (2010) 333-350.
[11] M. Balog, M. Schieber, M. Michman, S. Patai, Chemical vapor deposition and characterization of HfO2 films from organo-hafnium compounds, Thin Solid Films, 41 (1977) 247-259.
[12] S.M. Sze, Physics of Semiconductor Devices, Wiley, New York, 1981.
[13] X. Duan, Y. Huang, R. Agarwal, C.M. Lieber, Single-nanowire electrically driven lasers, Nature, 421 (2003) 241-245.
[14] D. Wang, Y.-L. Chang, Q. Wang, J. Cao, D.B. Farmer, R.G. Gordon, H. Dai, Surface Chemistry and Electrical Properties of Germanium Nanowires, Journal of the American Chemical Society, 126 (2004) 11602-11611.
[15] C.M. Lieber, Nanoscale science and technology: building a big future from small things, Mrs Bulletin, 28 (2003) 486-491.
[16] V.G. Dubrovskii, G.E. Cirlin, V.M. Ustinov, Semiconductor nanowhiskers: Synthesis, properties, and applications, Semiconductors, 43 (2009) 1539-1584.
[17] J. Xiang, W. Lu, Y. Hu, Y. Wu, H. Yan, C.M. Lieber, Ge/Si nanowire heterostructures as high-performance field-effect transistors, Nature, 441 (2006) 489-493.
[18] D. Wang, Q. Wang, A. Javey, R. Tu, H. Dai, H. Kim, P.C. McIntyre, T. Krishnamohan, K.C. Saraswat, Germanium nanowire field-effect transistors with SiO 2 and high-κ HfO 2 gate dielectrics, Applied Physics Letters, 83 (2003) 2432-2434.

[19] L. Zhang, R. Tu, H. Dai, Parallel core-shell metal-dielectric-semiconductor germanium nanowires for high-current surround-gate field-effect transistors, Nano letters, 6 (2006) 2785-2789.
[20] G. Zheng, W. Lu, S. Jin, C.M. Lieber, Synthesis and Fabrication of High-Performance n-Type Silicon Nanowire Transistors, Advanced Materials, 16 (2004) 1890-1893.
[21] G. Liang, J. Xiang, N. Kharche, G. Klimeck, C.M. Lieber, M. Lundstrom, Performance Analysis of a Ge/Si Core/Shell Nanowire Field-Effect Transistor, Nano Letters, 7 (2007) 642-646.
[22] Y. Li, F. Qian, J. Xiang, C.M. Lieber, Nanowire electronic and optoelectronic devices, Materials today, 9 (2006) 18-27.
[23] J. Goldberger, A.I. Hochbaum, R. Fan, P. Yang, Silicon Vertically Integrated Nanowire Field Effect Transistors, Nano Letters, 6 (2006) 973-977.
[24] Y. Ahn, J. Park, Efficient visible light detection using individual germanium nanowire field effect transistors, Applied Physics Letters, 91 (2007) 162102-162102-162103.
[25] A.B. Greytak, C.J. Barrelet, Y. Li, C.M. Lieber, Semiconductor nanowire laser and nanowire waveguide electro-optic modulators, Applied Physics Letters, 87 (2005) -.
[26] S. Gradečak, F. Qian, Y. Li, H.-G. Park, C.M. Lieber, GaN nanowire lasers with low lasing thresholds, Applied Physics Letters, 87 (2005) -.
[27] M. Björk, B. Ohlsson, T. Sass, A. Persson, C. Thelander, M. Magnusson, K. Deppert, L. Wallenberg, L. Samuelson, Nanoletters 2, 87 (2002), Appl. Phys. Lett, 80 (2002) 1058.
[28] W. Lu, C.M. Lieber, Nanoelectronics from the bottom up, Nature materials, 6 (2007) 841-850.
[29] F. Patolsky, G. Zheng, O. Hayden, M. Lakadamyali, X. Zhuang, C.M. Lieber, Electrical detection of single viruses, Proceedings of the National Academy of Sciences of the United States of America, 101 (2004) 14017-14022.
[30] F. Patolsky, G. Zheng, C.M. Lieber, Nanowire-Based Biosensors, Analytical Chemistry, 78 (2006) 4260-4269.
[31] G. Zheng, F. Patolsky, C.M. Lieber, Nanowire biosensors: a tool for medicine and life science, Nanomedicine : nanotechnology, biology, and medicine, 2 (2006) 277.
[32] E.-S. Liu, J. Nah, K.M. Varahramyan, E. Tutuc, Lateral Spin Injection in Germanium Nanowires, Nano Letters, 10 (2010) 3297-3301.
[33] S.A. Wolf, D.D. Awschalom, R.A. Buhrman, J.M. Daughton, S. von Molnár, M.L. Roukes, A.Y. Chtchelkanova, D.M. Treger, Spintronics: A Spin-Based Electronics Vision for the Future, Science, 294 (2001) 1488-1495.
[34] R. Jansen, Silicon spintronics, Nature materials, 11 (2012) 400-408.
[35] I. Žutić, J. Fabian, S. Das Sarma, Spintronics: Fundamentals and applications, Reviews of Modern Physics, 76 (2004) 323-410.
[36] I. van Weperen, S.R. Plissard, E.P.A.M. Bakkers, S.M. Frolov, L.P. Kouwenhoven, Quantized Conductance in an InSb Nanowire, Nano Letters, 13 (2012) 387-391.
[37] M. Wawrzyniak, J. Martinek, B. Susła, Conductance quantization in nanowires formed at the metal-semiconductor interface, in: Journal of Physics: Conference Series, IOP Publishing, 2009, pp. 012035.
[38] W. Lu, J. Xiang, B.P. Timko, Y. Wu, C.M. Lieber, One-dimensional hole gas in germanium/silicon nanowire heterostructures, Proceedings of the National Academy of Sciences of the United States of America, 102 (2005) 10046-10051.

[39] R.S. Wagner, W.C. Ellis, VAPOR-LIQUID-SOLID MECHANISM OF SINGLE CRYSTAL GROWTH, Applied Physics Letters, 4 (1964) 89-90.
[40] H. Omi, T. Ogino, Self-assembled Ge nanowires grown on Si(113), Applied Physics Letters, 71 (1997) 2163-2165.
[41] A.M. Morales, C.M. Lieber, A Laser Ablation Method for the Synthesis of Crystalline Semiconductor Nanowires, Science, 279 (1998) 208-211.
[42] G.-C. Yi, Vapor–Liquid–Solid Growth of Semiconductor Nanowires, Springer, Berlin Heidleberg, 2012.
[43] T. Mizuno, J. Okumtura, A. Toriumi, Experimental study of threshold voltage fluctuation due to statistical variation of channel dopant number in MOSFET's, Electron Devices, IEEE Transactions on, 41 (1994) 2216-2221.
[44] A.B. Greytak, L.J. Lauhon, M.S. Gudiksen, C.M. Lieber, Growth and transport properties of complementary germanium nanowire field-effect transistors, Applied Physics Letters, 84 (2004) 4176-4178.
[45] P. Xie, Y. Hu, Y. Fang, J. Huang, C.M. Lieber, Diameter-dependent dopant location in silicon and germanium nanowires, Proceedings of the National Academy of Sciences, 106 (2009) 15254-15258.
[46] S. Zhang, E.R. Hemesath, D.E. Perea, E. Wijaya, J.L. Lensch-Falk, L.J. Lauhon, Relative Influence of Surface States and Bulk Impurities on the Electrical Properties of Ge Nanowires, Nano Letters, 9 (2009) 3268-3274.
[47] J. Hannon, S. Kodambaka, F. Ross, R. Tromp, The influence of the surface migration of gold on the growth of silicon nanowires, Nature, 440 (2006) 69-71.
[48] S. Kodambaka, J.B. Hannon, R.M. Tromp, F.M. Ross, Control of Si nanowire growth by oxygen, Nano letters, 6 (2006) 1292-1296.
[49] J.E. Allen, E.R. Hemesath, D.E. Perea, J.L. Lensch-Falk, Z. Li, F. Yin, M.H. Gass, P. Wang, A.L. Bleloch, R.E. Palmer, High-resolution detection of Au catalyst atoms in Si nanowires, Nature Nanotechnology, 3 (2008) 168-173.
[50] M.I. den Hertog, J.-L. Rouviere, F. Dhalluin, P.J. Desré, P. Gentile, P. Ferret, F. Oehler, T. Baron, Control of gold surface diffusion on Si nanowires, Nano letters, 8 (2008) 1544-1550.
[51] S.H. Oh, K.v. Benthem, S.I. Molina, A.Y. Borisevich, W. Luo, P. Werner, N.D. Zakharov, D. Kumar, S.T. Pantelides, S.J. Pennycook, Point defect configurations of supersaturated Au atoms inside Si nanowires, Nano letters, 8 (2008) 1016-1019.
[52] S. Barth, M.M. Koleśnik, K. Donegan, V. Krstić, J.D. Holmes, Diameter-Controlled Solid-Phase Seeding of Germanium Nanowires: Structural Characterization and Electrical Transport Properties, Chemistry of Materials, 23 (2011) 3335-3340.
[53] R.H. Kingston, Review of Germanium Surface Phenemena, Journal of Applied Physics, 27 (1956) 101.
[54] T. Hanrath, B.A. Korgel, Influence of Surface States on Electron Transport through Intrinsic Ge Nanowires, The Journal of Physical Chemistry B, 109 (2005) 5518-5524.

2. Theory of Electrical Transport in Nanowires

In this chapter we expound the theoretical background necessary to understand the results presented in the remainder of the thesis. We shall first look in section 2.1 at the principles of electrical measurements and the physical meaning of resistivity and mobility which we aim to measure. The details of our experimental set up will not be discussed here, but will be the subject of Chapter 3. In Section 2.2 we will discuss some of the basic theory of electrons in a solid. We saw in section 1.1 that surface states can have a great impact on the performance of semiconductor field-effect transistors. In Section 2.3 we therefore explore the theoretical background to the origin of these states. The formation and electrical characteristics of Schottky barriers will be detailed in Section 2.4. Particular attention will be paid to the role of interface states in determining the height of the Schottky barrier, which will be discussed in detail in Section 2.4. In Section 2.5 we discuss the use of the Kubo-Greenwood formula to calculate the mobility in germanium nanowires. We will use this theory to help to explain the diameter dependence of the resistivity which we measure, as will be shown in Chapter 5. The general properties of memristance will then be discussed in Section 2.6. The distinction between memristors, memristive systems and memristive devices will be discussed. This will be of importance when we develop a model for memristance in our devices, which will be elucidated in Chapter 4. Finally section 2.6 deals with the temperature dependence of nanowires which we shall use in the discussion of our low temperature measurements in Chapter 6.

2.1 Resistivity, Mobility and Basic Measurement Principles

In this section we will examine the Drude model of electrical conduction, first proposed by Paul Drude in 1900 [1, 2], 3 years after the discovery of the electron by Thompson [3]. In particular we will examine the definition of electrical resistivity and mobility .We will then examine the methods used to measure resistivity and mobility.

2.1.1 Definition of Resistivity and Mobility

When an electric field, $\boldsymbol{E} = \{E_x, E_y, E_z\}$, is applied to a material the free electrically charged particles in that material will experience a force, $\boldsymbol{F} = \{F_x, F_y, F_z\}$, causing them to drift in the direction of the applied field. We can write [4]:

$$F_\beta = qE_\beta = \frac{m_{\alpha\beta} v_{D,\alpha}}{\tau}, \qquad \text{Eq. 2.1}$$

where q is the charge of the particle, $v_{D,\alpha}$ is the drift velocity, τ is the typical time between scattering events and α and β are indicies labelling direction, (x, y, z). $m_{\alpha,\beta}$ is a component of the second rank mass tensor, relating the component of the field applied in the β direction to the component of the drift velocity in the α direction [1].

Eq. 2.1 is the free electron model, where it is assumed that between collisions with the crystal lattice the electron's movements are unaffected by the presence of the surrounding material. In reality the crystal lattice will create an electric field which will alter the movement of the free electrons. The net effect of this field is included by replacing the mass with the effective mass, $m_{\alpha\beta} \rightarrow m^*_{\alpha\beta}$. More details about the

[1] The drift velocity of the charge carriers may not be in the same direction as the applied electric field if the crystal is not cubic or there is also an applied magnetic field, for example. In this case the off-diagonal elements of m_{ij} will be non-zero. If the drift velocity is in the direction of the applied field the tensors are still necessary to allow for the fact that in general materials may be anisotropic, such that the effective mass will depend on the direction of the applied field (i.e. $m_{xx} \neq m_{yy}$).

effective mass will be given in Section 2.2.2. This is termed the nearly-free electron model [4]. Using this we may rearrange Eq. 2.1 to give:

$$v_{D,\alpha} = \frac{q\tau E_\beta}{m^*_{\alpha\beta}} = \mu_{\alpha\beta} E_\beta, \qquad \text{Eq. 2.2}$$

where $\mu_{\alpha\beta} = q\tau / m^*_{\alpha\beta}$ is a component of the mobility tensor. The drift velocity is related to the current density as [4]:

$$j_\alpha = nq v_{D,\alpha}, \qquad \text{Eq. 2.3}$$

where n is the carrier concentration. The current density is the total current, I, per cross sectional area, A. Combining Eq. 2.2 and Eq. 2.3 gives:

$$j_\alpha = nq\mu_{\alpha,\beta} E_\beta = \sigma_{\alpha\beta} E_{\beta,} \qquad \text{Eq. 2.4}$$

where σ_{ij} is a component of the conductivity tensor, $\hat{\sigma}$ [4]. The resistivity tensor, $\hat{\rho}$, is simply the inverse of the conductivity tensor [4]:

$$\hat{\rho} = \hat{\sigma}^{-1} = \frac{1}{det(\hat{\sigma})} adj(\hat{\sigma}). \qquad \text{Eq. 2.5}$$

In our measurements we always measure the current in the same direction as we apply the electric field. As such we measure only one component of the conductivity, resistivity or mobility tensors. For this reason we consider these quantities to be scalar and subsequently drop the subscripts for simplicity [2].

In semiconductors the current will in general be carried by both electrons and holes. The electrons and holes may have different drift velocity, mobility and concentration. All equation given above and subsequent equation derived in the

[2] The tensors will be reintroduced briefly in Section 2.5 when we discuss the Kubo and Kubo-Greenwood formulae.

coming sections should therefore contain both electrons and holes. For example Eq. 2.4 is more correctly written as:

$$j = nq\mu_e E + pq\mu_h E = \sigma_e E + \sigma_h E, \qquad \text{Eq. 2.6}$$

where n and p are the concentration of electrons and holes respectively, and the subscripts e and h are used to differentiate between the mobility and conductivity of the electrons and the holes.

The electron and hole concentrations must obey the law of mass action, which states that the product of the electron and hole concentrations must be equal to the intrinsic carrier concentration squared [4]. For germanium the intrinsic carrier concentration is of the order of 10^{13} cm^{-3} [4]. We shall show in Chapter 4 that the hole concentration in our nanowires is of the order of 10^{19} cm^{-3}. This implies that the electron concentration is of the order of 10^{7} cm^{-3}. Due to the fact that there is 12 orders of magnitude difference between the hole and electron concentrations we ignore the holes in our calculations and use the simplified equations as presented in this chapter.

2.1.1 Measuring Resistivity

In practise we do not measure the resistivity of a wire, but rather we measure its resistance, R. These quantities are related by the active channel length of the device, L, and the cross sectional area of the wire [4]:

$$R = \frac{\rho L}{A}. \qquad \text{Eq. 2.7}$$

From Eq. 2.4, Eq. 2.5, Eq. 2.7 and the definition of the current density it can be shown that the resistance relates the applied voltage, $V = LE$, to the current as:

$$V = IR. \qquad \text{Eq. 2.8}$$

The most basic way to measure the resistance of a nanowire is in a two-point configuration: here two electrical contacts are placed on the nanowire, which we label the source and the drain electrode. A voltage, V_{SD}, is applied across these two contacts and the resulting current is measured. In this configuration the measured resistance, R_{2P}, is not the actual resistance of the nanowire, R_{NW}, but rather this resistance plus the total contact resistance, R_C [5]:

$$R_{2p} = \frac{V_{SD}}{I} = R_{NW} + R_C. \qquad \text{Eq. 2.9}$$

I is the measured current. The active channel length is measured from the outside of the source to the outside of the drain electrode as shown in Figure 2.1 (a) for the case of a side contacted quasi one dimensional wire [6]. The basic electrical set up is also shown in Figure 2.1 (a), but will be discussed in more depth in Chapter 3. Only the outermost contacts are used for a two point measurement. The contact resistances come from the details of the interface between the electrodes and the nanowire. The Schottky barrier at the interface will make a major contribution to this (*cf.* Section 2.4). In order to get around the problem of decoupling the resistance of the nanowire and the total contact resistance four-point measurements are made. In this case two additional contacts are placed on the wire between the source and drain contacts. The voltage drop across these inner contacts, V_{4p}, is recorded. This is shown in Figure 2.1 (a). Assuming that the current in the voltage probes is negligible the resistance of the nanowire is given by:

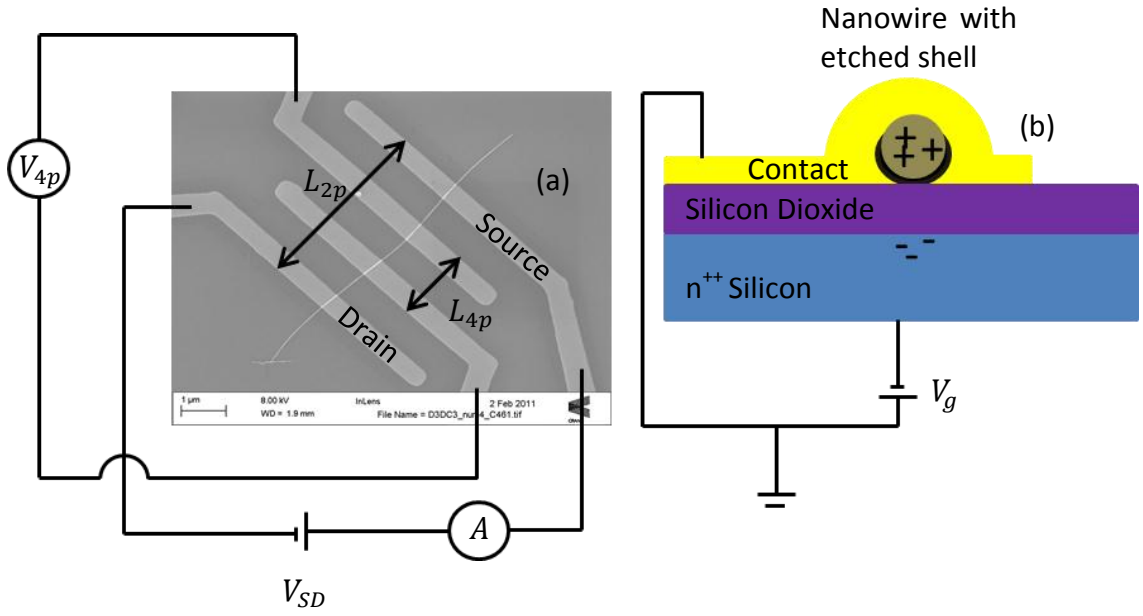

Figure 2.1 Schematic diagram of nanowire field effect transistor (a) shows a scanning electron microscope image of a 4-point nanowire device. The source and drain electrodes are indicated, as are the active channel length for both the 2 point and the 4 point case. The basic electrical circuit is indicated. In the case of a 2 point measurement the two middle contacts and the associated circuitry would be missing. (b) Drawing of the principle cross section of a nanowire field effect transistor arrangement. The silicon is doped to the point of metallicity. The applied gate voltage is indicated, as is the metal contact and the shell, which has been etched away at the top of the nanowire. We depict the situation where a negative gate voltage is applied. This results in an accumilation of negative charge at the interface between the silicon and the oxide, which induces a positive charge in the germanium nanowire. We may consider this as a capacitor, with the n^{++} Si as one plate, the Ge nanowire as the other seperated by the SiO_2 dielectric.

$$R_{NW}^{(4p)} = \frac{V_{4p}}{I}. \qquad \text{Eq. 2.10}$$

The active channel length for a four point measurement, L_{4p}, is the distance from the outside of the two inner contacts [6] as shown in Figure 2.1 (a).

2.1.2 Measuring Field Effect Mobility

From Eq. 2.4 it can be seen that:

$$\sigma = ne\mu, \qquad \text{Eq. 2.11}$$

where we now replace q with e, the charge of the electron. In order to extract the mobility in the channel of a field effect transistor the gate is modelled as a capacitor with the gate electrode as one plate and the active channel, in our case the nanowire,

acting as the other plate [5]. This is apparent from the cross section of the device depicted in Figure 2.1 (b). The gate capacitance, C_g is related to the carrier concentration by:

$$C_g = \frac{dQ}{dV_g} = LAe\frac{dn}{dV_g}, \quad \text{Eq. 2.12}$$

where Q is the charge on each plate of the capacitor, V_g is a the gate voltage. Differentiating both sides of Eq. 2.11 with respect to the applied gate voltage gives:

$$\frac{d\sigma}{dV_g} = \frac{dn}{dV_g}e\mu, \quad \text{Eq. 2.13}$$

where we have assumed that the mobility is constant with the applied gate voltage. Solving this equation for dn/dV_g and putting it back into Eq. 2.12 we find:

$$C_g = \frac{d\sigma}{dV_g}\frac{LA}{\mu}. \quad \text{Eq. 2.14}$$

Solving for the mobility gives:

$$\mu = \frac{d\sigma}{dV_g}\frac{AL}{C_g}. \quad \text{Eq. 2.15}$$

In practise we do not measure the conductivity directly, but rather measure the resistance. From Eq. 2.5, Eq. 2.5 and Eq. 2.8 we can write:

$$R_{NW} = \frac{V_{4P}}{I} = \frac{L}{\sigma A} \quad \text{Eq. 2.16}$$

and therefore that:

$$\sigma = \frac{IL}{V_{4p}A}. \quad \text{Eq. 2.17}$$

These equations are only valid for 4-point measurements, or else the contact resistance must be included. Finally differentiating Eq. 2.17 with respect to the gate voltage and putting the result into Eq. 2.15 we find:

$$\mu = \frac{dI}{dV_g}\frac{L^2}{C_g V_{4p}}. \qquad \text{Eq. 2.18}$$

This is a more useful equation than Eq. 2.15 as it relates the measured current and 4-point voltage to the mobility. Eq. 2.18 shows that the mobility may be found by measuring the rate of change of the current with the gate voltage with constant source drain voltage applied. This rate of change is known as the transconductance [5]. Equivalently we may measure the conductivity at different gate voltages, calculating the mobility from the slope of the conductivity plotted against the gate voltage, as shown by Eq. 2.15.

The biggest challenge faced in using Eq. 2.12 is correctly determining the gate capacitance. For back-gated nanowires and nanotubes devices a cylinder on plane model is usually used which reads [7]:

$$C_g = \frac{2\pi\varepsilon_{ox}\varepsilon_0 L}{\cosh^{-1}\left(\frac{h+r}{r}\right)}, \qquad \text{Eq. 2.19}$$

where ε_{ox} and ε_0 are the dielectric constant of the gate oxide and of free space, respectively, h is the thickness of the oxide and r is the radius of the nanowire. If $h \gg r$ Eq. 2.13 can be simplified to:

$$C_g = \frac{2\pi\epsilon_{ox}\epsilon_0 L}{\ln\left(\frac{2h}{r}\right)}. \qquad \text{Eq. 2.20}$$

For our samples this introduces an error of approximately 2 %. Eq. 2.19 is only strictly valid if the oxide completely surrounds the wire, the wire is effectively metallic so that the induced charge resides only on the surface, and the distance between the contacts is infinite so that the distortion of the electric field may be neglected [8]. These assumptions are clearly not valid for a back gated semiconducting nanowire and so the capacitance is normally overestimated, resulting in the measured value for the mobility being too low (see Eq. 2.12) [8].

Furthermore in deriving Eq. 2.12 it is assumed that all the charge induced by the gate is mobile, and so contributes to the current. This will not be the case if there are a large number of charge traps present, such as those located on the germanium surface [9, 10]. In this case at least part of the charge on the gate electrode will be compensated by charges trapped in these surface states which do not contribute to the current flow. This is normally modelled by defining two capacitances, C_{int} and C_{acc}. C_{int} is the capacitance of the interface and C_{acc} is the capacitance of the free carrier, the subscript standing for accumulation. The two capacitors are connected in parallel, so the total gate capacitance is given by: $C_g = C_{int} + C_{acc}$. The final expression for the mobility is then given by replacing C_g in Eq. 2.12 with C_{acc}. This can be written as [11]:

$$\mu_{Intrinsic} = \frac{dI}{dV_g}\frac{L^2}{C_g V_{Sd}}\left(1 + \frac{C_{int}}{C_{acc}}\right) = \frac{d\sigma}{dV_g}\frac{AL}{C_g}\left(1 + \frac{C_{int}}{C_{acc}}\right). \qquad \text{Eq. 2.21}$$

Here we have labelled the mobility as intrinsic to differentiate it from the measured, or extrinsic, mobility given by Eq. 2.12. $C_{int} = eD_{it}$ where D_{it} is the density of interface states [11]. C_{acc} can be approximated as ϵ_{Ge}/t_{acc}. where ϵ_{Ge} is the dielectric constant of germanium and t_{acc} is the distance between the accumulated charge and the

surface of the nanowire due to quantum mechanical confinement [11]. If we assume that t_{acc} is 1 nm we find that the term $C_{int}/C_{acc} = D_{it} \times 10^{-14}$, where D_{it} is in units of $eV^{-1}\,cm^{-2}$. On the germanium surface the interface trap density has been found to be as large as 10^{14} $ev^{-1}\,cm^{-2}$ [12], suggesting that the mobility calculated using Eq. 2.12 could be wrong by a factor of 2. Nonetheless the contribution of the surface states to the capacitance is usually ignored due to the fact that t_{acc} is impossible to measure experimentally. We shall also use Eq. 2.12 in analysing our results in Chapter 4, but it is important to remember that in the case where there is a large density of surface states that this represents a lower bound to the true mobility.

2.2 Electrons in a Periodic Potential

We shall now develop the theory of electrons in solids arising from quantum theory. Firstly we will look at the origin of Bloch waves, followed by the details of parabolic bands in germanium. The details of the valence band will be described as will the non-parabolic correction necessary in low dimensional structures. Finally we will examine some salient details of the density of states. Many of the equations and ideas from this section will be used in Chapter 5 when we calculate the mobility of our nanowires.

2.2.1 Bloch Waves

Let us assume that we have a particle in a Bravais lattice, defined by a set of points at positions $\boldsymbol{R}$. We may then define a set of reciprocal lattice vectors $\boldsymbol{G}$, such that $e^{i\boldsymbol{G}.\boldsymbol{R}} = 1$**.** The potential, $V(\boldsymbol{r})$, of this lattice will be periodic in real space, $V(\boldsymbol{r}+\boldsymbol{R}) = V(\boldsymbol{r})$. We may express the potential as a Fourier expansion in terms of the reciprocal lattice vectors as [4, 13]:

$$V(\boldsymbol{r}) = \sum_{\boldsymbol{G}} V_{\boldsymbol{G}} \exp(i\boldsymbol{G}.\boldsymbol{r}). \qquad \text{Eq. 2.22}$$

The wavefunction, $\Psi_{\mathbf{k}}(\boldsymbol{r})$**,** may in general also be written as a Fourier series in terms of its wavevector $\boldsymbol{k}$ [4, 13]:

$$\Psi_k(\boldsymbol{r}) = \sum_{\boldsymbol{k}} C_{\boldsymbol{k}} \exp(i\boldsymbol{k}.\boldsymbol{r}) \qquad \text{Eq. 2.23}$$

where $\boldsymbol{k}$ will take a discrete set of values depending on the boundary conditions considered. The time-independent Schrödinger equation is given by [4, 13]:

$$\left[-\frac{\hbar^2}{2m}\nabla^2 + V(\boldsymbol{r})\right]\Psi(\mathbf{r}) = E\Psi(\mathbf{r}), \qquad \text{Eq. 2.24}$$

where ∇^2 is the Laplace operator, and $\hbar$ is Planck's constant divided by 2π. To find the allowed values of the coefficients in Eq. 2.23, we put Eq. 2.22 and Eq. 2.23 into Eq. 2.24 resulting in [4, 13]:

$$\sum_{\boldsymbol{k}} \frac{\hbar^2 k^2}{2m} C_{\boldsymbol{k}}\, e^{i\boldsymbol{k}.\boldsymbol{r}} + \sum_{\boldsymbol{k},\boldsymbol{G}} C_{\boldsymbol{k}} V_{\boldsymbol{g}} e^{i(\boldsymbol{G}+\boldsymbol{k}).\boldsymbol{r}} = E \sum_{\boldsymbol{k}} C_{\boldsymbol{k}} e^{i\boldsymbol{k}.\boldsymbol{r}}. \qquad \text{Eq. 2.25}$$

Due to the fact that $\boldsymbol{G}$ is a reciprocal lattice vector and we are summing over all $\boldsymbol{k}$ we may replace $\boldsymbol{k}$ in the second term of Eq. 2.25 with $\boldsymbol{k} - \boldsymbol{G}$ [4, 13][3]. Doing this and rearranging we find [4, 13]:

$$\sum_{\boldsymbol{k}} e^{i\boldsymbol{k}.\boldsymbol{r}} [\left\{\frac{\hbar^2 k^2}{2m} - E\right\} C_{\boldsymbol{k}} + \sum_{\boldsymbol{G}} V_{\boldsymbol{G}} C_{\boldsymbol{k}-\boldsymbol{G}}] = 0. \qquad \text{Eq. 2.26}$$

If this is to be valid at every point in the crystal it must be true for all values of $\boldsymbol{k}$. Therefore the term in the square brackets must disappear, giving [4, 13]:

[3] i.e. $\sum_k \boldsymbol{k} = \sum_k \boldsymbol{k} - \boldsymbol{G}$

$$\left\{\frac{\hbar^2 k^2}{2m} - E\right\} C_{\boldsymbol{k}} + \sum_{\boldsymbol{G}} V_{\boldsymbol{G}} C_{\boldsymbol{k}-\boldsymbol{G}} = 0. \qquad \text{Eq. 2.27}$$

This equation defines coefficients that are to be used in Eq. 2.23. It is important to note that the only coefficients that appear here are the ones that differ by an integer number of reciprocal lattice vectors. This allows us to rewrite Eq. 2.23 as [4, 13]

$$\Psi_k(\boldsymbol{r}) = \sum_{k-G} C_{k-G} e^{i(\boldsymbol{k}-\boldsymbol{G}).\boldsymbol{r}} = \left(\sum_{G} C_{k-G} e^{-i\boldsymbol{G}.\boldsymbol{r}}\right) e^{i\boldsymbol{k}.\boldsymbol{r}} \qquad \text{Eq. 2.28}$$

$$= u_k(\boldsymbol{r}) e^{i\boldsymbol{k}.\boldsymbol{r}}$$

The final expression is Bloch's theorem [14], which states that in any periodic lattice the wavefunction of a single electron will have the form of a plane wave multiplied by a function with the periodicity of the lattice [4].

2.2.2 Parabolic Bands and Effective Mass

Eq. 2.27 can be rearranged to give:

$$E = \frac{\hbar^2 k^2}{2m} + C_{\boldsymbol{k}}^{-1} \sum_{\boldsymbol{G}} V_{\boldsymbol{G}} C_{\boldsymbol{k}-\boldsymbol{G}}. \qquad \text{Eq. 2.29}$$

If we now examine the case when $V_G \approx 0$, we find that the second term is nearly constant. It is usual to treat it as a constant, $E^{(Min,P)}$, with a value equal to its true value at $k = 0$, $E^{(Min,P)} = C_0^{-1} \sum_{\boldsymbol{G}} V_{\boldsymbol{G}} C_{0-\boldsymbol{G}}$ [4, 13]. Eq. 2.29 then predicts a parabolic relationship between k and E, which is found to be approximately true near to $k = 0$. The effect of the fact that the second term is not constant is taken into account by replacing the mass with a new effective mass [4, 13]. This is the justification for the

[4] The periodicity of $u_k(\boldsymbol{r})$ can be seen by replacing $\boldsymbol{r}$ with $\boldsymbol{r} + \boldsymbol{R}$, $\sum_G C_{k-G} e^{-i\boldsymbol{G}.\boldsymbol{r}} \rightarrow \sum_G C_{k-G} e^{-i\boldsymbol{G}.(\boldsymbol{r}+\boldsymbol{R})} = \sum_G C_{k-G} e^{-i\boldsymbol{G}.\boldsymbol{r}} e^{-i\boldsymbol{G}.\boldsymbol{R}} = \sum_G C_{k-G} e^{-i\boldsymbol{G}.\boldsymbol{r}}$, from the definition of $\boldsymbol{G}$.

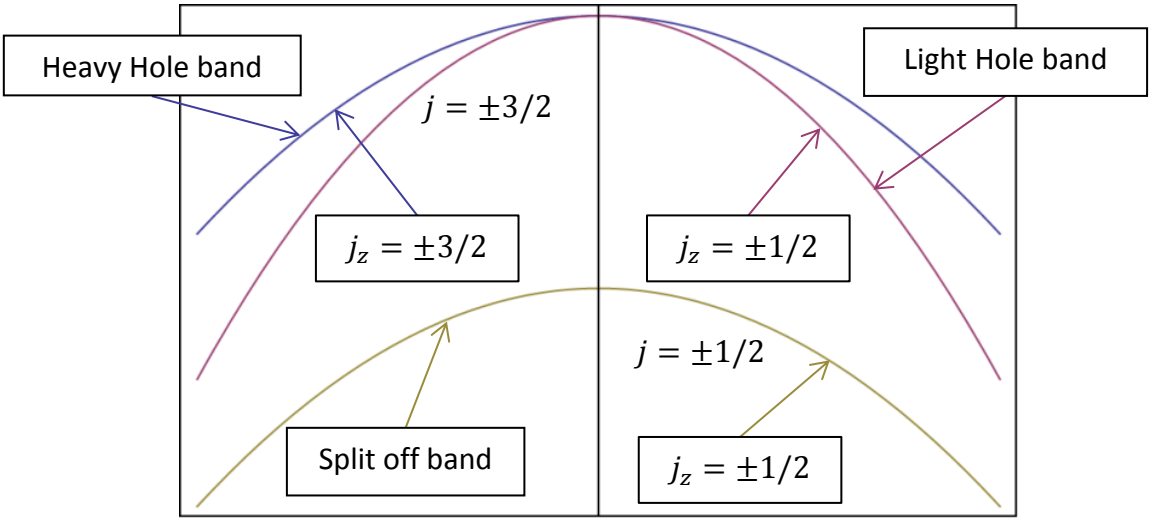

Figure 2.2 A depiction of the three bands at the top of the valence band in germanium The split off band has a total angular momentum of $j = \pm 1/2$ while the heavy and light hole bands have a value of $j = \pm 3/2$. The split off band lies below the other bands due to spin orbit coupling. The projection of the total angular momentum along the z axis is different for the heavy and light hole band, with $J_z = \pm 3/2$ and $J_z = \pm 1/2$ respectively. At the Γ point both bands are degenerate, but the degeneracy is lifted away from this point.

nearly free electron model that we introduced in Eq. 2.2. Eq. 2.29 can then be rewritten:

$$E = \frac{\hbar^2 k^2}{2m^*} + E^{(Min,P)}. \qquad \text{Eq. 2.30}$$

The effective mass is defined as [4, 13]:

$$\frac{1}{m^*} = \frac{1}{\hbar^2}\frac{d^2E}{dk^2} \qquad \text{Eq. 2.31}$$

which follows from Eq. 2.30.

2.2.3 Heavy Holes, Light Holes and the Split off Band

In germanium holes have three effective masses associated with them. This is due to the fact that the valence band derives ultimately from a *p*-orbital with an orbital angular momentum quantum number, $l = 1$ [13]. The total angular momentum quantum number is given by , $|l - s| < j < l + s$, where s is the electron spin quantum number equal to $1/2$ [13]. The total angular momentum is therefore $3/2$ or $1/2$, giving

rise to two bands, which we label $p_{1/2}$ and $p_{3/2}$. The spin-orbit interaction causes the $p_{1/2}$ band to have a lower energy than $p_{3/2}$ band, and it is therefore called the split-off band [13]. In germanium the split off band lies 0.295 eV below the $p_{3/2}$ band [15]. The projection of the total angular momentum along the z axis can take 4 values for the $p_{3/2}$ band, $j_z = +\frac{3}{2}, +\frac{1}{2}, -\frac{1}{2}, -\frac{3}{2}$. These four bands are degenerate at $k = 0$, but the degeneracy is lifted away from this point [13]. This gives rise to two bands - the heavy hole band with $j_z = \pm 3/2$ and the light hole band with $j_z = \pm 1/2$ [13]. The names are derived from the fact that the effective mass in each band is different. This is depicted in Figure 2.2.

2.2.4 Non-parabolicity in Nanostructures

It is known that for low dimensional systems however that the bands are no longer well described as parabolic, even near $k = 0$, as a result of the raising of the suband edges due to quantum confinement [16]. This is normally accounted for by introducing an extra term, α, known as the non-parabolicty parameter into Eq. 2.30 [16]:

$$E = U_i + \frac{-1 + \sqrt{1 + 4\alpha\left(\frac{\hbar^2 k^2}{2m} + E_i^{(Min,P)} - U_i\right)}}{2\alpha}, \qquad \text{Eq. 2.32}$$

where U_i is the total potential energy in the subband i. It can be shown that Eq. 2.30 is recovered when $\alpha \to 0$. α is a material dependent parameter. It takes different values for light holes, heavy holes, holes in the split off band and electrons, as well as depending on energy [17].

2.2.5 Density of States

The density of states, $g_m(E)$, is defined as the number of states per unit energy, per unit volume:

$$g_m(E) = \frac{1}{V}\left(\frac{dk}{dE}\right). \quad \text{Eq. 2.33}$$

If the material is modelled as a free electron gas in an infinite potential well the density of states can be calculated to be [13]:

$$g_m^{(3D)}(E) = \frac{1}{2\pi^2}\left(\frac{2m^*}{\hbar^2}\right)^{3/2}\sqrt{E} \quad \text{Eq. 2.34}$$

in three dimensions and [18]:

$$g_m^{(1D)}(E) = \frac{1}{\pi}\left(\frac{m^*}{\hbar^2}\right)^{\frac{1}{2}}\left(\frac{\Theta(E - E^{(Min,P)})}{\sqrt{E - E^{Min,P}}}\right) \quad \text{Eq. 2.35}$$

in one dimension [5], where $\Theta(E)$ is the Heaviside step function. In one dimension there is an infinity at the minimum of the parabolic band. The emergence of this singularity is important for the discussion of Fermi level depinning in Section 2.4.2.

It should also be noted in both three dimensions and one the density of states is proportional to the effective mass. For this reason the heavy hole band is normally more important than the light hole band in transport, despite the greater mobility of the light holes (see Eq. 2.2 and Section 5.3.6]) [13].

We may also calculate the density of states in one dimension starting from the non-parabolic bands given by Eq. 2.32. In this case we find the following expressions [16, 19]:

$$k(E) = \hbar^{-1}\sqrt{2m^*[E - E_i^{(Min,P)} + \alpha(E - U_i)^2} \quad \text{Eq. 2.36}$$

[5] In one dimension the units are per unit length, not per unit volume

$$v_i(E) = \frac{1}{\hbar}\frac{dE}{dk} = \frac{[1 + 2\alpha(E - U_i)]^{-1}\hbar k(E)}{m^*} \quad \text{Eq. 2.37}$$

$$g_m^{(NP)} = \frac{\Theta\left(E - E_i^{(Min,NP)}\right)2g}{\pi\hbar v_i(E)}, \quad \text{Eq. 2.38}$$

where $v_i(E)$ is the group velocity of the carrier in subband i at energy E and g is the valley degeneracy. These expressions are valid for either the conduction band or the valance band. In the case of the valance band there are no valleys and so $g = 1$. It should be noted that the effective mass will no longer be constant as the bands are no longer parabolic. The effective mass that appears in Eq. 2.37 is the effective mass for the parabolic band.

2.3 Origin of Surface States

The value of the wavevector $\boldsymbol{k}$ may be either real or imaginary [20]. If we make the replacement $\boldsymbol{k} \rightarrow \boldsymbol{k} + i\boldsymbol{\kappa}$ in Eq. 2.28, which defines Bloch functions, we find:

$$\psi_{\boldsymbol{k}}(\boldsymbol{r}) = [e^{i\boldsymbol{k}\cdot\boldsymbol{r}}u_{\boldsymbol{k}}(\boldsymbol{r})].\boldsymbol{e}^{-\boldsymbol{\kappa}\cdot\boldsymbol{r}}. \quad \text{Eq. 2.39}$$

The term in square brackets is the same as the right hand side of Eq. 2.28, but the second term increases exponentially in one direction, while decreasing exponentially in the opposite direction. Clearly a wavefunction that increases infinitely has no physical relevance in the bulk of a crystal, however it may exist at the surface, decaying away from the surface into the interior. It can be shown that such wavefunctions have energies that lie in the band gap of the semiconductor [20].

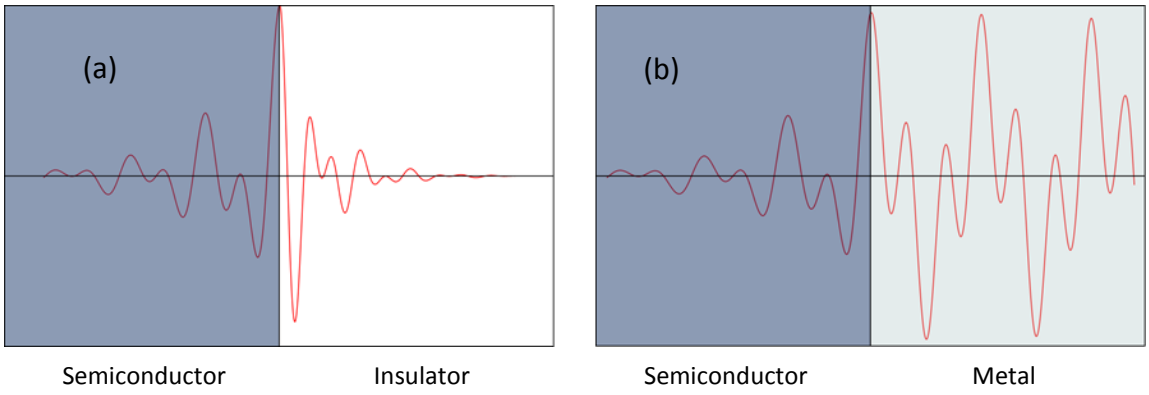

Figure 2.3 Representation of the wavefunction at the surface that give rise to surface states. (a) shows the wavefunction at a semiconductor/insulator interface.The wavefunction decays exponentially in both directions away from the interface, resulting in strong localisation of the electron at the interface between the materials. This is the same situation for an intrinsic surface state i.e. at the semiconductor/vaccuum interface. (b) shows a metal induced gap state. On the right an extended Bloch wave in the metal is shown, which decays exponentially in the semiconductor. It is important to note that the wavefunction and its derivitive are continuous at the boundry in both cases and that the periodicity of the Bloch waves in each material is different.

Outside of the crystal the wavefunction may take any form in principle, subject to the requirement that it and its derivative be continuous across the surface. In general this results in wavefunctions with a discreet set of $\boldsymbol{\kappa}$ for a given value of $\boldsymbol{k}$ [21]. If the semiconductor crystal is in contact with an insulator, for example, the wavefunction may join to a corresponding surface state in the band gap of the insulator, decaying exponentially both into the semiconductor and into the insulator. An example of a wavefunction of this type is shown in Figure 2.3 (a). Such states are strongly localised at the interface between the semiconductor and the insulator and are therefore referred to as interface states.For a free semiconductor surface the state on the surface may result from an unsatisfied bond on a surface atom. These are referred to as dangling bonds.

In the case that the semiconductor is contacted by the metal the surface states may join to the extended Bloch waves within the metal [21, 22]. Such states are called

metal induced gap states and are often described as the decay of the metal wavefunction into the semiconductor. Metal induced gap states can be either donors or acceptors [20, 21]. In general the states closer to the valence band are donors and those closer to the conduction band are acceptors [21]. The energy at which the states change from being mostly donors to mostly acceptors is known as the charge neutrality level [23, 24]. This energy is important in the discussion of Schottky barrier heights and Fermi level pinning as we shall discuss in Section 2.4.2. If the Fermi level is above this energy the surface will have a net negative charge, or it will be positively charged if it is below it. In germanium the charge neutrality has been measured to be 0.09 ± 0.07 eV above the valence band [23]. Due to the fact that it is so close to the valence band the Fermi level most often lies above it, leading to a negatively charged surface with free holes inside the bulk.

2.4 Schottky Barrier

We will now examine the details of Schottky barriers at metal/semiconductor interfaces. Schottky barriers should play a major role in the determination of the contact resistance of our devices, which we introduced in Section 2.1.1. We will look at the formation of the barriers and then discuss the barrier heights and Fermi level pinning. We will finally look at the way that Schottky barriers are modelled. This discussion will be useful when we develop a model for the memristive response in our devices in Chapter 4.

2.4.1 Origin of Schottky barrier

Consider the case where a metal and an *n*-doped semiconductor - that is a semiconductor which contains an excess of electrons due to the addition of donor

atoms - are isolated from each other, as shown in Figure 2.4 (a). The work function of the metal is the potential required to take an electron from the Fermi level to the vacuum level [25]. It is denoted as ϕ_m in Figure 2.4. The electron affinity of the semiconductor is the energy between the bottom of the conduction band and the vacuum level at the surface [25], and is shown in Figure 2.4 as χ_S. If the metal and semiconductor are connected the thermodynamic requirement for the Fermi level to be equal in the two materials causes charge carriers to flow from the one material into the other [26]. This scenario is shown in Figure 2.4 (b). In the case of an *n*-type semiconductor electrons will flow from the semiconductor to the metal. These electrons will accumulate in a thin layer at the surface of the metal, typically in a region under a nanometer from the surface [25]. This surface charge on the metal will repel the mobile electrons in the semiconductor, leaving behind a positively charged depletion region at the semiconductor surface. This results in band bending at the semiconductor surface as shown in Figure 2.4 (b). The total charge in the depletion region is directly related to the amount of band bending [25]. In equilibrium the total charge on the metal surface, Q_M must equal the total charge in the depletion region of the semiconductor, Q_S [25]:

$$Q_M + Q_S = 0 \qquad \text{Eq. 2.40}$$

This separation of charge will result in an electric field, E, being formed between the two materials, resulting in the voltage drop across the interface of $V_i = \delta E$ shown in Figure 2.4 (b), where δ is the distance between the surface of the metal and that of the semiconductor. In Figure 2.4 (c) we depict the situation as the gap between the two materials is almost closed, so that there is only a small insulating gap between them,

while an intimate contact is shown in Figure 2.4 (d). In reality an insulating layer usually exists, but is sufficiently thin that electrons can tunnel through easily. As a result it is usually difficult and unnecessary to distinguish between Figure 2.4 (c) and Figure 2.4 (d) in most practical situations [25]. In Figure 2.4 (d) the barrier height ϕ_b is shown. It is defined as the difference between the bottom of the conduction band at the surface and the Fermi level [25].

2.4.2 Schottky Barrier Height and Fermi Level Pinning

In 1939 Schottky and Mott proposed that the barrier height should be given by [25]:

$$\phi_b = \phi_M - \chi_S \qquad \text{Eq. 2.41}$$

for the case of an *n*-type semidunductor. With reference to Figure 2.4 it is then easy to see the origin of Eq. 2.41, if we remember that as $\delta \to 0$ the voltage drop must also disappear [25]. For a *p*-type semiconductor the corresponding equation is [25]:

$$\phi_b = E_g - (\phi_M - \chi_S), \qquad \text{Eq. 2.42}$$

where E_g is the band-gap of the semiconductor. Eq. 2.41 and Eq. 2.42 suggest that the barrier height for any given semiconductor should be entirely determined by the work function of the contacting metal. In many cases however it was found that the barrier height was in fact independent of the metal used [27]. This fact was explained by Bardeen in 1947 as resulting from the existence of surface states on the semiconductor [27].

In section 2.4.1 we described the fact that in the case of an *n*-type semiconductor there exists a region of negative charge on the surface of the contacting metal which is compensated by an equal positive charge on the semiconductor surface

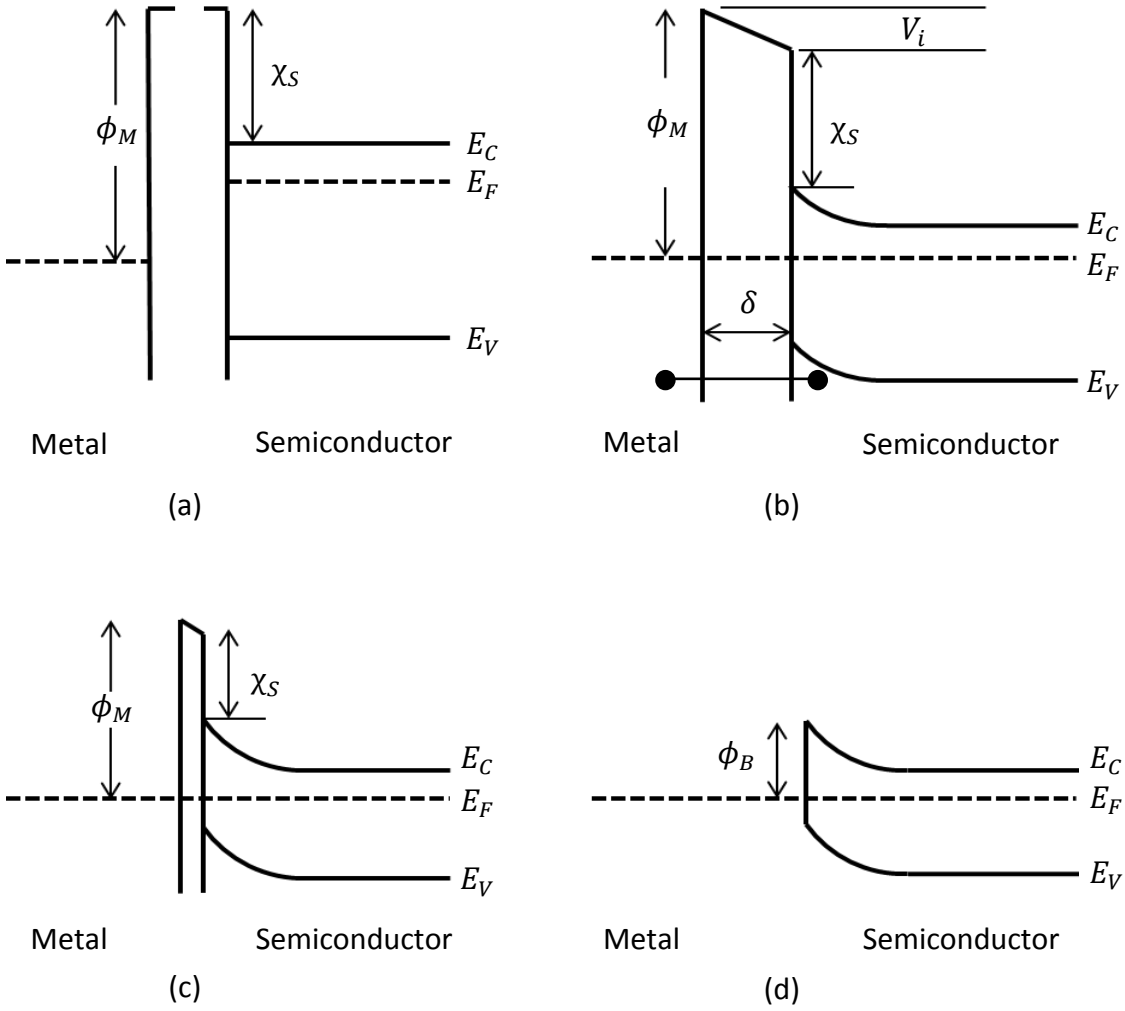

Figure 2.4 Schematic depiction of the formation of a Schottky barrier. (a) shows the situation when the metal and the semiconductor are seperated by a large distance. The work function of the metal and the electron affinity of the semiconductor are shown, as are the position of the bottom of the conduction band, E_C, the top of the valence band E_V and the Fermi level E_F in both materials. An *n*-type semiconductor is shown. (b) depicts the situation after electrons are alowed to freely move between the two materials, such as through the connecting wire shown at the bottom of the image. The transfer of charge from the semiconductor to the metal causes the Fermi level to be constant throughout the entire device. The resulting voltage drop across the interface is shown. (c) shows the situation when the seperation between two surfaces is greatly reduced, and (d) depicts intimate contact. (c) may be the most physically relevent situation as a thin layer of oxide often resides on the semiconductor surface. The barrier, ϕ_B is indictaed in (d).

resulting from a depletion region in the semiconductor. In the presence of charged surface states however, we must include the surface state charge, Q_{SS}, as well. The neutrality condition that must be met is then [25]:

$$Q_m + Q_{SS} + Q_S = 0 \qquad \text{Eq. 2.43}$$

As we discussed in Section 2.3 there exists an energy in the band gap known as the charge neutrality level. It is usual to define the height of the charge neutrality level relative to the top of the valence band as we have shown Figure 2.5. If this coincides with the Fermi level the surface is neutral [21]. In the case where the Fermi level is above the charge neutrality level the surface will have a negative charge. This situation is depicted in Figure 2.5. In Figure 2.5 (a) we depict the bands of the semiconductor surface and metal surface when there is a large gap between the two materials, just as we did in Figure 2.4 (a). We are effectively setting $Q_M = 0$ in Eq. 2.43. Due to the fact that the surface is negatively charged, there must exist a depletion region with associated band bending to satisfy the neutrality condition (Eq. 2.43), even in the absence of a metal contact [27]. When the metal and semiconductor are brought into contact the Fermi levels must align due to the transfer of electrons from the semiconductor to the metal just as they did in the case without surface states. In this case however the electron may originate from a surface state. If this happens the term $Q_M + Q_{SS}$ in Eq. 2.43 will be unchanged and so there does not need to be an increase in the charge in the depletion region to compensate. The greater of density of surfaces states relative to the density of states in the semiconductor, the greater the proportion of the charge that will originate from these states [25]. In the limit of an infinite density of states at the surface all of the charge will originate from surface states and so the band bending will be determined entirely by the details of the semiconductor surface, with the choice of metal being irrelevant [25]. This is equivalent to saying that the Fermi level of the semiconductor will not be changed after the contact is formed, and so this phenomena is referred to as Fermi level pinning. It is depicted in Figure 2.5. It

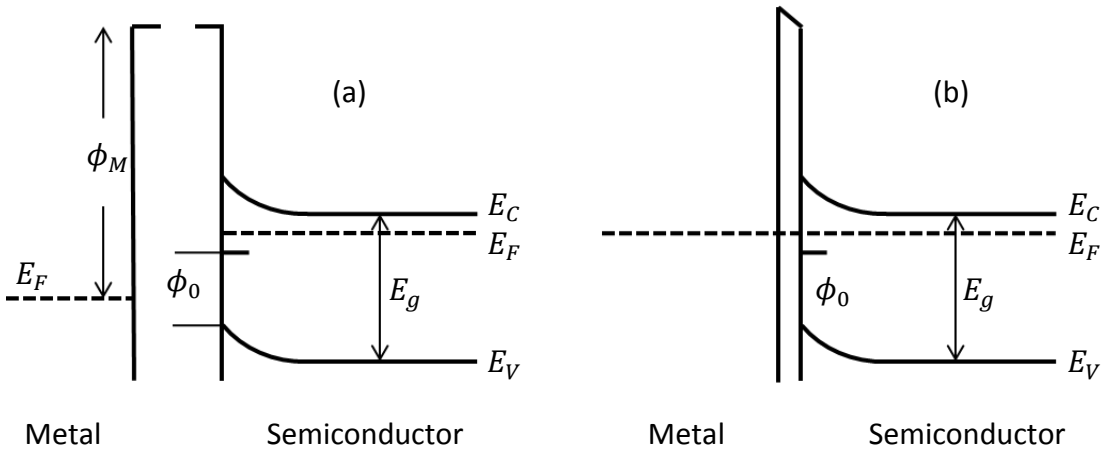

Figure 2.5 Schematic diagram of Schottky barrier formation in the presence of surface states In both diagrams the top of the valence band, E_V, the bottom of the conduction band, E_C, the Fermi level, E_F, the band gap, E_g, and the charge neutrality level, ϕ_0 are indicated. (a) shows the bands when the metal and the semiconductor are separated. The work function of the metal, ϕ_M is shown. The bands in the semiconductor are bent at the surface due to the negative charge in the surface states that results from the Fermi level being above the charge neutrality level. In (b) we show the bands after the metal and semiconductor are in close contact, analogous to Figure 2.4 (c). We have shown the extreme case with the density of surface states near to infinity. Due to this the band bending at the edge of the semiconductor which gives rise to the Schottky barrier is unaffected by the addition of the metal.

can be deduced from this image that in the case of perfect Fermi level pinning the height of the barrier is given by [27]:

$$\phi_b = E_g - \phi_0 \qquad \text{Eq. 2.44}$$

where E_g is the band gap. This limit may be practically reached if as few as one in every 100 surface atoms contributes a surface state [27].

Fermi level pinning is also the phenomenon that reduced the gate effect in MOSFETs in the presence of surface states as discussed in Section 1.1. A MOSFET works on the principle that a charge on the gate electrode is compensated by an equal but opposite charge in the semiconductor, which alters the resistivity of the semiconductor (see Eq. 2.4 and Section 2.1.2). In the presence of surface states the charge will be at least partially compensated by immobile charges on the surface, which do not contribute to the current [10]. Equivalently we may say that the Fermi level is pinned

by the surface states and cannot be changed by the gate. We will see in Chapter 4 that we observe such an effect in some of our wires.

It has been claimed that in the case of nanostructures Fermi level pinning should be alleviated [28]. An experimental demonstration of this has recently been reported [6]. This arises from the fact that in one dimension the density of states goes to infinity for certain energies, as discussed in Section 2.2.5. As a result the density of states of free carriers in the semiconductor is greater than the density of trapped surface states and the above argument no longer holds. We note however that it is theoretically predicted that the pinning will only be significantly alleviated if there are fewer than one surface state per ten surface atoms for a wire with a 6 nm diameter [28]. As our wires have diameters from 10 to 25 nm we expect that fewer surface states will be necessary for pinning to occur. We will argue in Chapter 4 that the density of trap states at the core/shell interface is close to the density of surface atoms in our devices, meaning Fermi level pinning may occur here. This will be further discussed in Chapter 6.

2.4.3 Modelling Current Flow Through Schottky Barriers

The current flow through a Schottky barrier is ideally given by the equation [25]:

$$j = j_0 \exp\left(\frac{qV}{k_B T}\right) \qquad \text{Eq. 2.45}$$

where k_B is Boltzmann's constant, T is the temperature and j_0 is a constant. An example of the current voltage (IV) curve given by Eq. 2.45 is shown in Figure 2.6. The form of j_0 depends on the way that the current flow is modelled. There are two main models used, arising from the fact that there are two possible current limiting

mechanisms [25]. The first is the diffusion of the electrons across the depletion region at the surface of the semiconductor. This gives rise to the diffusion model, which gives [25]:

$$j_0 = qN_C\mu E_{Max}\exp\left(-\frac{q\phi_b}{k_BT}\right), \qquad \text{Eq. 2.46}$$

where N_C is the effective density of states in the conduction band of the semiconductor, μ is the mobility of the semiconductor perpendicular to the surface and E_{Max} is the maximum electric field in the barrier. It should be noted that E_{Max} depends on the magnitude of the applied voltage [25]. As a result j_0 is not constant, and so the Schottky barrier is not ideal.

An alternative model for a Schottky barrier is the thermionic emission model. Here it is assumed that the current limiting process is the transfer of the electrons across the metal-semiconductor interface [25]. In this case we may write [25]:

$$j_0 = A^*T^2\exp\left(-\frac{q\phi_b}{k_BT}\right), \qquad \text{Eq. 2.47}$$

where A^* is Richardson's constant. This too deviates from ideality due to the fact that the barrier height is voltage dependant [25]. As we are assuming that the current limiting process is not the electron reaching the interface, but rather the movement across the interface itself there will be an accumulation of electrons inside the semiconductor at the interface. This will induce an equal and opposite charge inside the metal resulting in additional electric field across the interface which will act to reduce the barrier height under forward bias [25]. It is usual to define a quantity, η, known as the ideality factor as [25]:

$$\frac{1}{\eta} = 1 - \left(\frac{d\phi_b}{dV}\right). \qquad \text{Eq. 2.48}$$

Eq. 2.48, Eq. 2.47 and Eq. 2.48 can be combined to give:

$$j = A^* T^2 \exp\left(-\frac{q\phi_b^{(0)}}{k_B T}\right) \exp\left(\frac{qV}{k_B T}\right), \qquad \text{Eq. 2.49}$$

where $\phi_b^{(0)}$ is the barrier height with no applied voltage. An ideal Schottky barrier can be recovered by setting $\eta = 1$ which is equivalent to setting the barrier height to be independent of the applied voltage as can be seen from Eq. 2.48.

The length of the diffusion region is typically of the order of 1 μm [25]. As this is much longer than the width of the nanowire, it is likely that the depleted region is curtailed in the nanowires. As a result the main barrier to current flow will be emission across the barrier. It is therefore expected that thermionic emission theory is most applicable in the case of nanowires [25, 29].

Even in the case of an ideal Schottky barrier the contact resistance will not be a constant, but will depend on the magnitude of the applied voltage. This can easily be seen from Figure 2.6 (a). The contact resistance will be given by the inverse of the slope of this graph, which is clearly not a constant. This relationship will be further complicated by the deviations from ideallity discussed in relation to Eq. 2.46 and Eq. 2.47. This complicated relationship between the applied voltage and the contact resistance will be important for us in the discussion of the memristance of our devices in Chapter 4.

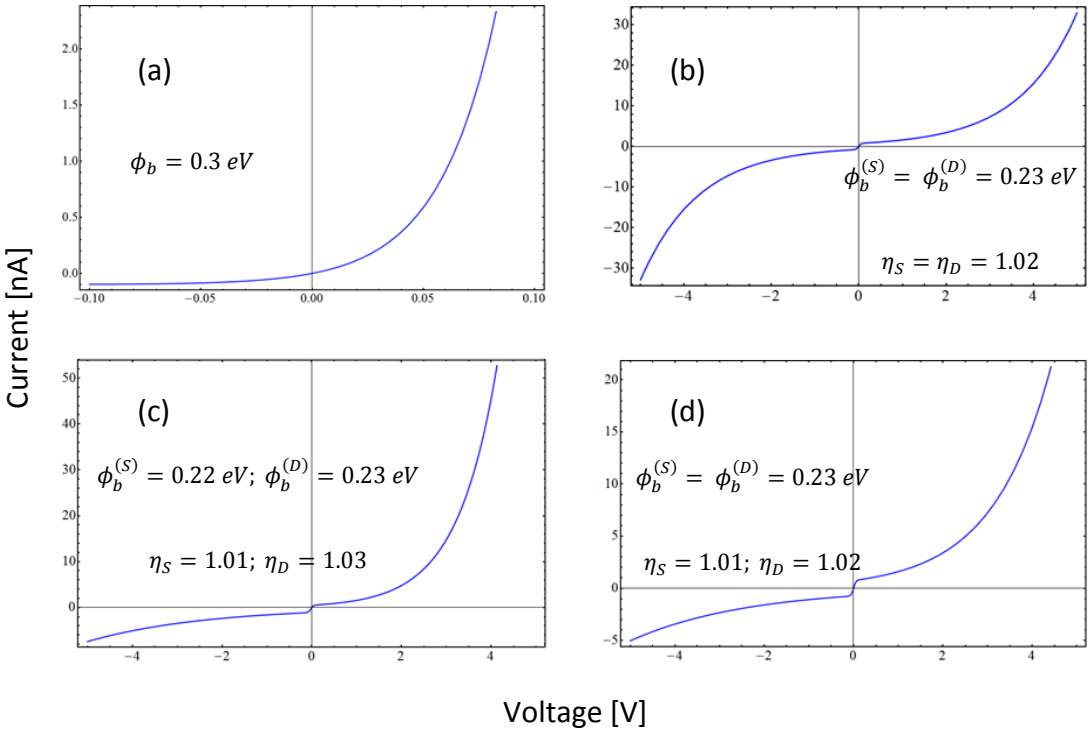

Figure 2.6 Examples of theoretical IV curves for Schottky barriers (a) shows a single ideal Schottky barrier, while (b), (c) and (d) show examples of non-ideal back to back barriers. The barrier heights and ideality factors used are indicated on each graph. In (b) the same barrier height and ideality factor is used for both contacts and a symmetric curve results. In (c) and (d) asymmetric curves are seen due to the fact that he barriers are not identical. Note that the asymmetry can arise from differences in the barrier heights or differences in the ideality factors, or both. At low biases there appears to be a region with low resistance. This is an artifact from the equations, which does not appear in real devices. It is removed by adding a shunt resistance to the Schottky barrier equations [25]

In our devices we will have not one, but two Schottky barriers – one at the source and one at the drain. For the case of ideal back to back Schottky barriers the current is given by [29]:

$$j = \frac{J_S J_D \sinh\left(\frac{qV}{2k_B T}\right)}{J_S \exp\left(\frac{qV}{2k_B T}\right) + J_D exp\left(-\frac{qV}{2k_B T}\right)}, \qquad \text{Eq. 2.50}$$

where $J_{S,D} = A^* T^2 \exp\left(-\frac{q\phi_b^{(S),(D)}}{k_B T}\right)$ and $\phi_b^{(S)}$ and $\phi_b^{(D)}$ are the barrier heights at the source and drain respectively when the thermionic emission model is used. The non-ideality of the barriers is introduced by replacing $\phi_b^{(S),(D)}$ as [29]:

$$\phi_b^{(S),(D)} \rightarrow \phi_0^{(S),(D)} - V\left(\frac{d\phi_b^{(S),(D)}}{dV}\right) = \phi_0^{(S),(D)} + V\left(\frac{1}{\eta} - 1\right) \qquad \text{Eq. 2.51}$$

where the last expression uses Eq. 2.48. Some examples of an IV curves given by Eq. 2.50 is shown in Figure 2.6. For our analysis of our two point measurements in section 2.6 and Chapter 4 it is important to note that the IV curve will be symmetric only if the two barrier heights and ideality factors are equal.

2.5 Kubo-Greenwood Formula

The field effect mobility of nanowires may be extracted from measurements of the transconductance, as shown in Section 2.1.2. We will see in Chapter 4 that we did not see a gate effect in many of our wires, making the extraction of the mobility impossible. In Chapter 5 we shall discuss the effect that changing the nanowire diameter has on the resistivity of the germanium. To understand these results in the absence of experientially obtained mobilities we calculated the mobility of the wires using the Kubo-Greenwood formula.

The Kubo formula is used to determine the response of a system to an externally applied field. It assumes that the response is linear [30]. To ensure that this condition is met for our wires we apply this analysis to the linear region of the IV characteristics near to $V_{sd} = 0\,V$. The key insight in deriving the conductivity of the system is that the induced current does not depend solely on the externally applied field, but also of the electric field inside the material, which may itself be altered by the induced current [30]. The formula is [30, 31]:

$$\sigma_{\alpha\beta}(\boldsymbol{q},\omega) = \frac{1}{\omega V}\int_0^\infty dt\, e^{i\omega t}\langle\psi\left|\left[j_\alpha^\dagger(\boldsymbol{q},t), j_\beta\,(\boldsymbol{q},0)\right]\right|\psi\rangle + i\frac{n_0 e^2}{m\omega}\delta_{\alpha\beta} \qquad \text{Eq. 2.52}$$

where α and β are direction in real space, $\boldsymbol{q}$ and ω are the wavevector and the angular frequency respectively of the applied electric field, V is the volume of the solid, $|\psi\rangle$ is the wavefunction of the ground state of the system without any external field applied, $j_\alpha(\boldsymbol{r},t)$ is the current operator at a time t and a position $\boldsymbol{r}$, $j_\alpha^\dagger(\boldsymbol{r},t)$ is its Hermitian conjugate, and $[a,b]$ is the commutator of a and b. The D.C. conductivity is found from Eq. 2.52 by first setting $\boldsymbol{q}\to 0$ and then setting $\omega \to 0$ [30] [6].

It is interesting to note that the wavefunction that appears in Eq. 2.52 is the wavefunction of the ground state without any contribution from the applied external field [30]. The Hamiltonian contains all of the interactions in the solid, including electron-electron interactions. The conductivity tensor is an intrinsic property of the system. In the derivation of the Kubo formula the applied field is treated as a perturbation [30].

It is often convenient and sufficient to model materials as non-interacting Fermi systems. The single particle Eigenstate, $|n\rangle$ and Eigenvalue, E_n are given by:

$$H_0|n\rangle = E_n|n\rangle \qquad \text{Eq. 2.53}$$

[6] The reason for doing the operation is this order can be understood on physical grounds. If ω is let go to 0 before the wavevector then the applied field would be constant in time, but vary spacially. This would lead to an unphysical rearrangement of the charge that would result in the wrong solution being obtained when $\boldsymbol{q}$ is subsequently set to 0.

The Hamiltonian is then taken to be the sum of each of the single particle Hamiltonians. Under this assumption Eq. 2.52 can be re-written in the static limit as [32, 33]:

$$\sigma_{\alpha\beta} = \frac{\pi\hbar}{\mathrm{V}} \int \langle \sum_{nm} j_{\alpha}^{nm} j_{\beta}^{nm} \delta(E - E_n)\delta(E - E_m) \rangle \, dE, \qquad \text{Eq. 2.54}$$

where $j_{\alpha}^{nm} = \langle n|j_{\alpha}|m\rangle$ and the brackets $\langle \dots \rangle$ in Eq. 2.54 indicate a sum over all possible scattering configurations. This is the Kubo-Greenwood formula.

The mobility of a one-dimensional nanowire may be calculated from Eq. 2.54. It has been shown that the mobility of a subband i is given by [16, 34]:

$$\mu_i = \frac{2ge}{n_i \pi\hbar} \int_{E_i^{(Min,NP)}}^{\infty} \frac{dE\tau_i(E)v_i(E)}{4k_B T cosh^2\left(\frac{E - E_F}{2k_B T}\right)} \qquad \text{Eq. 2.55}$$

where g is the valley degeneracy, n_i is the density of charge carriers in the sub-band, $\tau_i(E)$ and $v_i(E)$ are the total momentum relaxation time and velocity of a charge carrier in the sub-band at energy E, $E_i^{(Min,NP)}$ is the minimum energy of the non-parabolic sub-band (see Section 2.2.4), k_B is Boltzmann's constant, E_f is the Fermi level and T is the temperature. The valley degeneracy is set to 1 in the case of the valance band. The total mobility is calculated by taken a summation over all sub-bands, weighted by the carrier concentration of each sub-band [16, 34]:

$$\mu_{total} = \frac{1}{n_{total}} \sum_i \mu_i n_i. \qquad \text{Eq. 2.56}$$

Here n_{total} is the total number of carriers.

It is Eq. 2.55 and Eq. 2.56 that we shall use in Chapter 5 to calculate the mobility in our devices. The main part of the calculation is working out the total momentum

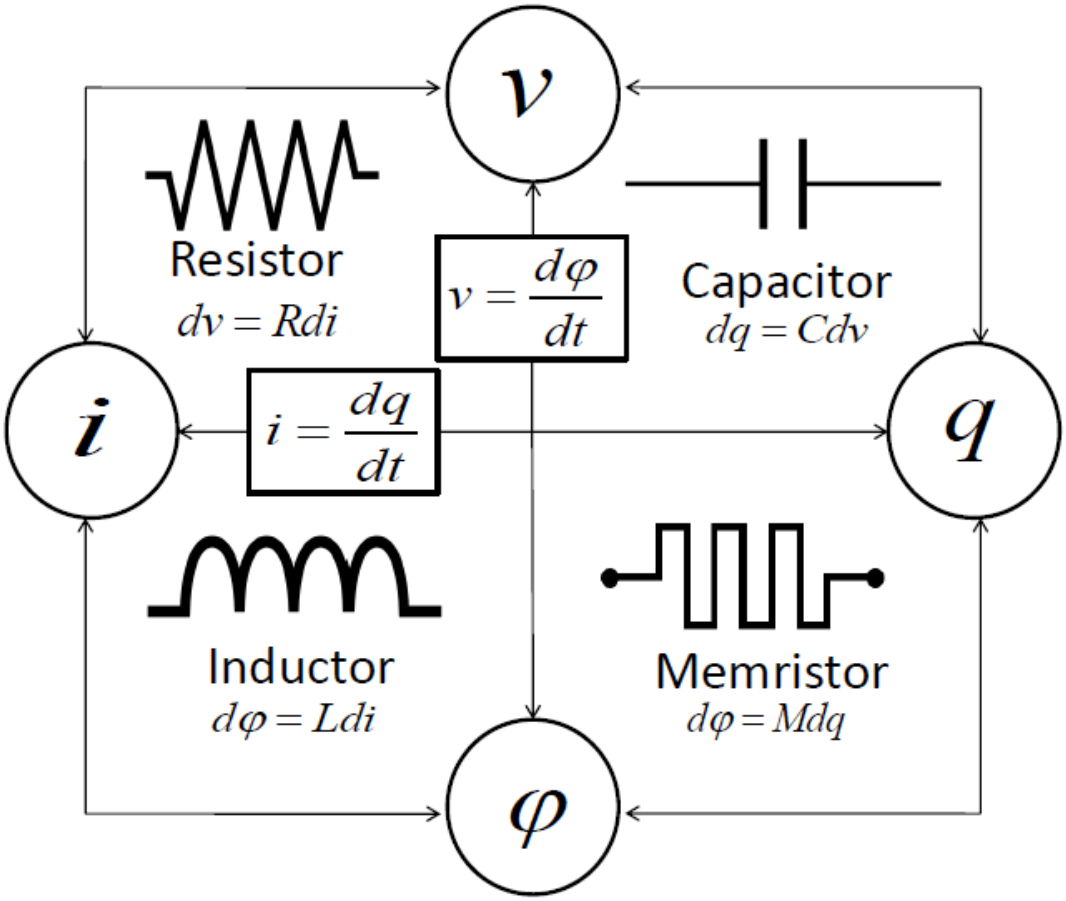

Figure 2.7 Schematic diagram showing the relationships between current, voltage, flux and charge**.**The four basic state variables are shown in circles on each side of the square. In each corner the circuit element that links the two adjacent variables is shown along with its governing equation. State variables on opposite sides of the square are linked by the equations that are also given.

relaxation time. This is achieved by calculating the relaxation time due to each individual scattering mechanism and then using Matthiessen's rule to sum them. This is discussed in detail in Chapter 5.

2.6 Memristance

In 1971 Leon Chua postulated that there should exist a fourth passive circuit element to complement the resistor, capacitor and inductor [35]. This argument was based on the fact that there are four important state variables for electronic devices: the voltage, v,

the current i, the magnetic flux, $\varphi = \int v\, dt$, and the charge, $q = \int i\, dt$ [7]. All possible pairs of these variables except one were related through one of the previously mentioned devices, or through the definitions of charge and magnetic flux. For example the current and voltage are related through the resistor, as shown in Eq. 2.8, and on the top left of Figure 2.7. Chua realised that there was no device that related the charge to the flux however, and so it was through this symmetry argument that he proposed the existence of a new device which he named the memristor [35]. A schematic diagram of this idea is shown in Figure 2.7, with the memristor on the bottom right. The name is a portmanteau of "memory-resistor" [35], for reasons that will become clear in the following paragraphs.

A memristor is characterised by its memristance, M. It can easily be deduced from Figure 2.7 that this is given by:

$$d\varphi = M dq. \qquad \text{Eq. 2.57}$$

Memristance has units of Ohms and if it is constant it is indistinguishable from resistance [35]. This can be seen from the fact that if we differentiate Eq. 2.57 with respect to time holding M constant we recover Eq. 2.8.

In Chua's original paper he proposed that the memristor should be a single valued function of the charge or the flux exclusively [35]. We will refer to such a device as ideal memristors. For clarity in the following discussion we will talk only about memristors which depend on the charge, $M \to M(q)$. Such memristors are called current controlled memristors. The details of a memristor in which the memristance

[7] We use lower case letters for the voltage and the current here to indicate that they may be either AC or DC in general. In previous sections we have implicitly assumed the DC case.

depends on the flux is exactly analogous, simply replace every instance of the word current with voltage and charge with flux.

In order to understand the origin of the memory in a memristor it is important to note that the charge referred to is not the charge within the device, such as in the case of a capacitor, but rather the total amount of charge that has moved through the device from time $t = 0$ to a time t [35]. This follows from the fact that the charge is defined as the time integral of the current. As a result the charge, and hence the value of the memristance, changes only when a current is flowing in the device. From this definition of the charge and Eq. 2.57 it follows that this change must be reversible – when the current direction is reversed the memristance returns to its original value [35]. In the absence of current flow the charge and hence the memristance is a constant which depends only on the history of the current flow through the device. It is this property that gives the memristor the first part of its name, and that has led to the commercial interest in it, due to its possible use in non-volatile memory [36].

In 1976 Chua and his student Sung Mo Kang generalised the principle of the memristor to include devices that did not depend solely on charge or flux [37]. They defined a new set of equations governing what they referred to as memristive systems:

$$y = g(x, u, t)u$$
$$\dot{x} = f(x, u, t) \qquad \text{Eq. 2.58}$$

where x represents one or more state variables. It is not a requirement that g or f are explicit functions of u or t. In that paper they define the memristor [37] as a special case of Eq. 2.58 where we may write:

$$v = R(x, i, t)i$$
$$\dot{x} = f(x, i, t). \qquad \text{Eq. 2.59}$$

This is a broader definition of a memristor than given by Eq. 2.57. We shall use the convention of referring to devices described by Eq. 2.59 as memristive devices. Memristors described by Eq. 2.57 shall be called ideal memristors and the term memristive system will be used for the broad range of devices described by Eq. 2.58. A memristor is a specific memristive device where x must be either the charge or the flux and $\dot{x}$ is the current or voltage by definition.

It can easily be seen from Eq. 2.59 that if a voltage v is applied across a memristive system at a time t the current may take a range of different values, depending on the state of the system at that time. The one exception to the rule is that when $v = 0$ no current can flow. This fact differentiates memristive systems from an arbitrary dynamical system [38]. This zero crossing property and the fact that that the memristor is defined as a passive circuit element mean that memristive devices store no energy [38]. As a result the IV response of a memristor with a sinusoidal driving potential with a mean value of 0 is a double valued Lissajous figure, more commonly known as a pinched hysteresis loop [38]. An example of this type of curve is shown in Figure 2.8. As the frequency of the driving potential increases the IV curve of a memristor will tend towards being a straight line, as shown in Figure 2.8. This can be intuitively understood by realising that in order for the resistance of the device to change some physical property of the device must be reversibly altered. As the driving frequency tends towards infinity the time for the physical change to occur approaches

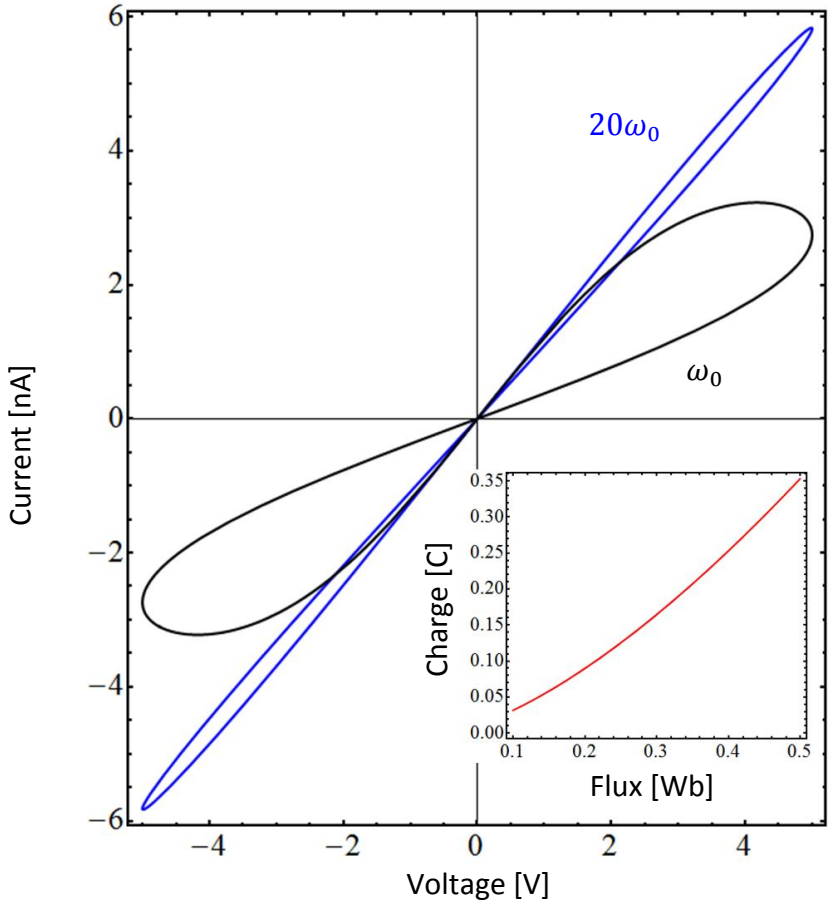

Figure 2.8 A example of a pinched hysteresis loop The solid black curve in the main diagram is the pinched hysteresis loop. The blue curve shows the response of the same device when the frequency is increased 20 times. It is clear that it approaches a linear resistor in this regime. In the insert the relationship between the charge and flux that gives rise to these curves is shown.

zero. This leads to a constant memristance, which is equivalent to a resistor [35], as we have already seen.

In Chapter 4 we will show pinched hysteresis loops in the IV characteristics of some of our wires. We will develop a model to show that this is the result of charge traps at the interface between the core and the shell that shows that these nanowirewire field effect transistors are memristive devices.

2.7 Temperature Dependence of the Resistivity of Solids

We finish this chapter by looking at the theory behind the change in resistivity with temperature. It is clear from Eq. 2.4 and Eq. 2.5 that the resistivity depends on the mobility and the carrier concentration. We therefore first examine the change in the mobility with temperature in Section 2.7.1 before turning our attention to the carrier concentration in Section 2.7.2. In Chapter 6 we will see that the equations described in Sections 2.7.1 to 2.7.2 do not well describe all of our experimental data. We shall therefore introduce Mott variable range hopping theory in Section 2.7.3, which is valid near to the metal insulator transition.

2.7.1 Temperature Dependence of Mobility

For Bloch waves in a perfectly periodic material the conductivity is infinite [4]. The finite conductivity observed in normal metals is the direct result of deviations from perfect periodicity [4, 39]. Thermally excited vibrations of the lattice, called phonons, are the most important contributor to deviations from periodicity at room temperature [4, 39]. Phonon scattering is reduced as the temperature is lowered due to the reduction in the phonon population [4]. This leads to an increase in the mobility, which in turn leads to a smaller resistivity, with decreasing temperature [4]. This effect is dominant in metals, as the carrier concentration is almost independent of temperature [4]. Below the Debye temperature, Θ_D, the resistivity of a metal at a given temperature is given by the Bloch-Gruneisen formula [39]:

$$\rho_\mu(T) = \rho(0) + A\left(\frac{T}{\Theta_D}\right)^5 \int_0^{\Theta_D/T} \frac{t^5}{(e^t - 1)(1 - e^{-t})}\, dt \qquad \text{Eq. 2.60}$$

where A is a material parameter and t is a dummy variable. The Bloch-Gruneisen formula is linear at large temperatures and varies as $\rho_\mu \propto T^5$ at low temperatures.[8]

2.7.2 Temperature Dependence of the Carrier Concentration

In a semiconductor the concentration of free charge carriers is determined by the number of electrons that are excited from the valence band to the conduction band, giving rise to free electrons and free holes, the number of electrons excited from donor levels to the conduction band, giving rise to free electrons and bound positive charges, or from the valence band to acceptor levels giving rise to free holes and trapped negative charges [4]. In each case the number of electrons excited across the relevant energy gap, E_A[9], depends exponentially on the temperature and follows an Arrhenius law [4]. If we assume that this is the only contribution to the resistivity change we can write [4]:

$$\rho_n(T) = \rho_0 e^{\frac{E_A}{k_B T}}, \qquad \text{Eq. 2.61}$$

where ρ_0 is a constant. For the case of intrinsic semiconductors $E_A = E_g/2$, where E_g is the band gap. For a doped semiconductor E_A is the energy between the chemical potential and either the valence or the conduction band for, for *p*-type and *n*-type doping respectively.

Let us now consider the case of a semiconductor doped with shallow dopants. At high temperatures the dopants will be entirely ionised and there will also be a substantial number of carriers excited across the band gap. As the temperature is

[8] Eq. 2.60 can be modified to give $\rho_\mu \propto T^3$ or $\rho_\mu \propto T^2$ at low temperatures for *s-d* electron scattering or electron-electron scattering respectively. We do not consider these process here.
[9] The subscript A refers to the fact that the electrons are activated across this energy gap.

lowered from room temperature the dopants remain completely ionised, but an increase in resistivity is seen which results from the reduction in carriers excited from the valence to the conduction band [13]. This is termed the intrinsic regime [13]. At intermediate temperatures the carrier concentration is constant as there are no carriers excited across the gap, but the dopants are still ionised completely [13]. This is termed the saturation regime [13]. Finally at low temperatures the dopants begin to recombine and another region with increasing resistivity is observed, known as the extrinsic regime [13]. It should be noted that due to the form of Eq. 2.61 a plot of $\ln(R)$ Vs. $1/T$ should yield a linear plot in the intrinsic and extrinsic regimes. The slope of this plot will be related to the band gap in the former and the ionisation energy of a dopant in the latter.

2.7.3 Variable Range Hopping

In a strongly disordered material there may exist localised and extended states [18, 40]. These two types of states will not exist at the same energies, but will be separated by a well-defined critical energy, E_C [18, 40]. In a semiconductor the localised states will exist in the band gap, and will in fact be made up of states removed from either the conduction or valence band [18]. If the Fermi level crosses E_C from the extended states to the localised states the mobility will be greatly reduced and a metal-to-insulator transition will occur [40]. This is known as an Anderson transition and the energy E_C is known as the mobility edge [40, 41]. After an Anderson transition there are two ways in which conduction can happen [40]. The first is that electrons are excited to extended states across the mobility edge [40]. This will give a temperature dependence of the form of Eq. 2.61 [40]. Alternatively if the temperature is too low to allow this to happen

conduction proceeds by electrons or holes hopping from one localised state to another [18, 40].

This type of hopping conduction was first proposed in 1960 [42] it was assumed that the carrier would always hop to its nearest neighbour [42]. Near to an Anderson transition however the localisation length is quite large and in general there will be many states that the carrier can jump to [40]. In this case the conduction is known as variable range hopping [18], to distinguish it from the case of nearest neighbour hopping.

It can be shown that in this case the resistivity varies with temperature as [43, 44]:

$$\rho(T) = \rho_0 exp\left(\left(\frac{T_0}{T}\right)^{\nu}\right) \qquad \text{Eq. 2.62}$$

where ρ_0 and T_0 are a constants and the value of ν depends on the model used. According to the model first proposed by Mott $\nu = (d+1)^{-1}$, where d is the dimensionality of the system [40]. In his derivation Mott ignores the role of electron-electron interactions [40]. When these are included a gap opens up in the single particle density of states near to the Fermi level [45] and the law is modified such that the exponent is to $1/2$ for all dimensions [43]. This is known as the Efros- Shklovskii law. The two equations are indistinguishable in one dimension. In Chapter 6 we shall see that variable range hopping fits our experimental data well for samples with a high resistivity which show a gate effect.

References

[1] P. Drude, Zur Elektronentheorie der Metalle, Annalen der Physik, 306 (1900) 566-613.
[2] P. Drude, Zur Elektronentheorie der Metalle; II. Teil. Galvanomagnetische und thermomagnetische Effecte, Annalen der Physik, 308 (1900) 369-402.
[3] J.J. Thomson, XL. Cathode Rays, The London, Edinburgh, and Dublin Philosophical Magazine and Journal of Science, 44 (1897) 293-316.
[4] N.W. Ashcroft, N.D. Mermin, Solid State Physics (Holt, Rinehart and Winston, New York, 1976), There is no corresponding record for this reference, (2005).
[5] S.M. Sze, Physics of Semiconductor Devices, Wiley, New York, 1981.
[6] M.M. Koleśnik-Gray, T. Lutz, G. Collins, S. Biswas, J.D. Holmes, V. Krstić, Contact resistivity and suppression of Fermi level pinning in side-contacted germanium nanowires, Applied Physics Letters, 103 (2013) 153101.
[7] S. Ramo, J.R. Whinnery, T. Van Duzer, Fields and waves in communication electronics, John Wiley & Sons, 2007.
[8] D.R. Khanal, J. Wu, Gate Coupling and Charge Distribution in Nanowire Field Effect Transistors, Nano Letters, 7 (2007) 2778-2783.
[9] S.A. Dayeh, C. Soci, K. Paul, T.Y. Edward, D. Wang, Influence of surface states on the extraction of transport parameters from InAs nanowire field effect transistors, Applied physics letters, 90 (2007) 162112.
[10] S. Hsu, Influence of surface states on the measurement of field-effect mobility, Electron Devices, IEEE Transactions on, 25 (1978) 1331-1332.
[11] S.A. Dayeh, D.P. Aplin, X. Zhou, P.K. Yu, E.T. Yu, D. Wang, High Electron Mobility InAs Nanowire Field-Effect Transistors, small, 3 (2007) 326-332.
[12] J. Mitard, K. Martens, B. DeJaeger, J. Franco, C. Shea, C. Plourde, F. Leys, R. Loo, G. Hellings, G. Eneman, Impact of Epi-Si growth temperature on Ge-pFET performance, in: Solid State Device Research Conference, 2009. ESSDERC'09. Proceedings of the European, IEEE, 2009, pp. 411-414.
[13] S.R. Elliott, The physics and chemistry of solids, Wiley, 1998.
[14] F. Bloch, Über die quantenmechanik der elektronen in kristallgittern, Zeitschrift für physik, 52 (1929) 555-600.
[15] C. Jacoboni, L. Reggiani, Bulk hot-electron properties of cubic semiconductors, Advances in physics, 28 (1979) 493-553.
[16] S. Jin, M.V. Fischetti, T. Tang, Modeling of electron mobility in gated silicon nanowires at room temperature: Surface roughness scattering, dielectric screening, and band nonparabolicity, Journal of Applied Physics, 102 (2007) 083715-083715-083714.
[17] S. Rodríguez-Bolívar, F. Gómez-Campos, F. Gámiz, J. Carceller, Implications of nonparabolicity, warping, and inelastic phonon scattering on hole transport in pure Si and Ge within the effective mass framework, Journal of applied physics, 97 (2005) 013702-013702-013710.
[18] D.K. Ferry, S.M. Goodnick, Transport in nanostructures, Cambridge university press, 1997.
[19] A. Godoy, Z. Yang, U. Ravaioli, F. Gámiz, Effects of nonparabolic bands in quantum wires, Journal of applied physics, 98 (2005) 013702-013702-013705.

[20] W. Shockley, On the Surface States Associated with a Periodic Potential, Physical Review, 56 (1939) 317-323.
[21] J. Tersoff, Schottky barrier heights and the continuum of gap states, Physical Review Letters, 52 (1984) 465-468.
[22] V. Heine, Theory of Surface States, Physical Review, 138 (1965) A1689-A1696.
[23] A. Dimoulas, P. Tsipas, A. Sotiropoulos, E.K. Evangelou, Fermi-level pinning and charge neutrality level in germanium, Applied Physics Letters, 89 (2006).
[24] D. Kuzum, K. Martens, T. Krishnamohan, K.C. Saraswat, Characteristics of surface states and charge neutrality level in Ge, Applied Physics Letters, 95 (2009) 252101.
[25] E.H. Rhoderick, R. Williams, Metal-semiconductor contacts, (1988).
[26] C. Kittel, Introduction to Solid State Physics, in, John Wiley & Sons, New York, 2005.
[27] J. Bardeen, Surface states and rectification at a metal semi-conductor contact, Physical Review, 71 (1947) 717.
[28] F. Léonard, A.A. Talin, Size-Dependent Effects on Electrical Contacts to Nanotubes and Nanowires, Physical Review Letters, 97 (2006) 026804.
[29] T. Nagano, M. Tsutsui, R. Nouchi, N. Kawasaki, Y. Ohta, Y. Kubozono, N. Takahashi, A. Fujiwara, Output Properties of C60 Field-effect transistors with Au electrodes modified by 1-alkanethiols, The Journal of Physical Chemistry C, 111 (2007) 7211-7217.
[30] G.D. Mahan, Many-particle physics, Springer, 2000.
[31] R. Kubo, Statistical-mechanical theory of irreversible processes. I. General theory and simple applications to magnetic and conduction problems, Journal of the Physical Society of Japan, 12 (1957) 570-586.
[32] D. Greenwood, The Boltzmann equation in the theory of electrical conduction in metals, Proceedings of the Physical Society, 71 (1958) 585.
[33] W.H. Butler, Theory of electronic transport in random alloys: Korringa-Kohn-Rostoker coherent-potential approximation, Physical Review B, 31 (1985) 3260-3277.
[34] R. Kotlyar, B. Obradovic, P. Matagne, M. Stettler, M. Giles, Assessment of room-temperature phonon-limited mobility in gated silicon nanowires, Applied physics letters, 84 (2004) 5270-5272.
[35] L. Chua, Memristor-The missing circuit element, Circuit Theory, IEEE Transactions on, 18 (1971) 507-519.
[36] D.B. Strukov, G.S. Snider, D.R. Stewart, R.S. Williams, The missing memristor found, Nature, 453 (2008) 80-83.
[37] L.O. Chua, S.M. Kang, Memristive devices and systems, Proc. IEEE, 64 (1976) 209-223.
[38] L. Chua, S. Kang, MEMRISTIVE DEVICES AND SYSTEMS, Proc IEEE, 64 (1976) 209-223.
[39] J. Bass, W.P. Pratt, P.A. Schroeder, The temperature-dependent electrical resistivities of the alkali metals, Reviews of Modern Physics, 62 (1990) 645-744.
[40] N. Mott, Metal-Insulator Transitions, Taylor and Francis, New York, 1990.
[41] N. Mott, The electrical properties of liquid mercury, Philosophical Magazine, 13 (1966) 989-1014.
[42] A. Miller, E. Abrahams, Impurity Conduction at Low Concentrations, Physical Review, 120 (1960) 745-755.
[43] B.I. Shklovskii, A.L. Efros, Electronic properties of doped semiconductors, Moscow Izdatel Nauka, 1 (1979).

[44] N. Mott, Conduction in non-crystalline materials: III. Localized states in a pseudogap and near extremities of conduction and valence bands, Philosophical Magazine, 19 (1969) 835-852.
[45] M. Pollak, Effect of carrier-carrier interactions on some transport properties in disordered semiconductors, Discussions of the Faraday Society, 50 (1970) 13-19.

3. Experimental approach

The wires examined in this work were grown in University College Cork by Richard Hobbs and Olan Lotty, working in the group of Professor Justin Holmes. In Section 3.1 we detail the method used to grow the wires, emphasising the details of the growth process that have an impact on our electrical measurements. Section 3.2 details our procedure for contacting single germanium nanowires. We then look at the methods used for imaging the nanowires in Section 3.3. Images of the nanowire are necessary both to ensure single wires have been contacted and to measure the diameter and channel length of measured wires, for extracting the resistivity as discussed in Section 2.1.1. Finally Section 3.4 gives the specific details of the electrical set up used to take all of the data presented in the subsequent chapters.

3.1 Nanowire Material

The germanium nanowires were produced with a supercritical fluid method using the metal/organic precursor hexakis(trimethysilyl)digermane ($Ge_2(TMS)_6$) [1]. It is important to note that no seed is required for this growth. This removes complications arising from doping of the wire due to the incorporation of seed, which was discussed in Section 1.2. The wires produced in this way are coated in an amorphous dielectric shell made of carbon, silicon, germanium, hydrogen and oxygen [1]. A TEM image of an individual wire is shown in Figure 3.1.

The growth of the nanowires is a two-step process. In the early stages of nanowire growth germanium nanocrystals are observed. The final batch of nanowire powder contains many of these nanocrystals along with the nanowires themselves. The nanowires are formed when these nanocrystals join together [2]. When the crystals

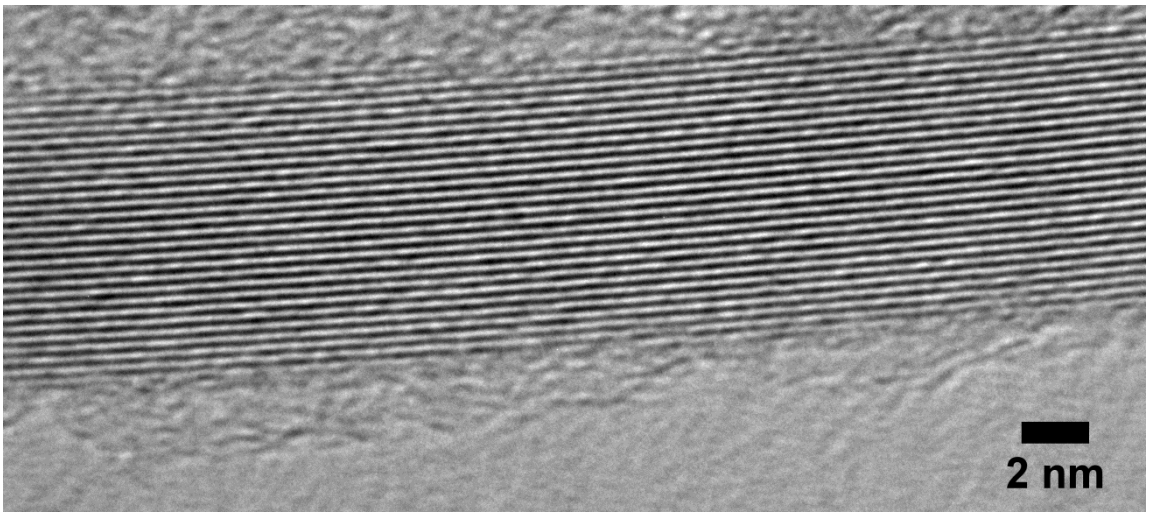

Figure 3.1 TEM image of typical germanium nanowire. The crystal structure of the germanium with a diameter of 8 nm can be clearly seen. Outside of the crystalline core the amorphous shell material approximately 1-2nm thick in this image can be made out. Image taken by Richard Hobbs.

initially join together to form nanowires the germanium remains in a liquid state, supported by an amorphous matrix that will eventually become the shell. Only when the mixture is cooled does the nanowire solidify, resulting in single-crystal nanowires. The growth direction is either <211> or <110> in equal proportion with a small number of <111> wires also present. No change in the crystallographic direction was observed when the growth conditions were varied.

We measured wires grown under two different growth conditions. The first batch of wires was grown at a temperature of 698 K for 15 hours. The chamber was cooled at a rate of 15 K/min. The second batch of wires was grown in two stages. First the precursor was heated to 723 K for 15 minutes, creating the germanium nanocrystals. The chamber was then cooled at a rate of 10 K/min to 523 K where it was held for 24 hours. It was during this stage that the nanowires formed. The process was changed to allow longer wires to be grown, and to increase the yield of wires. Wires from the first batch almost all had lengths of 1 μm or less, while in the second batch

lengths of 5 μm and greater were found regularly. A third batch of wires was grown with the same growth condition of the second batch. We will make no distinction between the wires grown at different times but with the same growth conditions as it was found that the electrical characteristics of different wires grown with the same parameters were identical. The dependence of the electrical characteristics on growth conditions shall be discussed in detail in Chapter 4.

3.2 Electrical contacting of single nanowires

In order to carry out electrical characterisation of the nanowires it is first necessary to contact them with metallic electrodes and to have a nearby gate. The nanowires are electrically contacted on an Si/SiO_2 substrate in order to allow gating. The SiO_2, which acts as the gate dielectric, is 300 nm thick and thermally grown on top of the silicon. The silicon itself is highly doped with arsenic, which is an *n*-type donor. A high level of doping ensures metallic behaviour even at low temperatures. The following sections describe in detail the process used to facilitate the contacting of the nanowires.

3.2.1 Photo-lithography patterning

The first step is to cleave the 6" wafer into 1 cm^2 pieces and pattern it using ultra violet (UV) lithography. The *OAI mask aligner* was used for this purpose. The mask used leaves an array of 36 possible sites at which a nanowire may be contacted. Each of these sites consists of four 250 μm x 250 μm pads and alignment markers. Metal is deposited by electron beam evaporation in the *Temescal FC2000.* and is typically Ti/Au (10 nm/40 nm). An optical image of a patterned substrate is shown in Figure 3.2 (a).

3.2.2 Placing the nanowires on the substrate

First the wires are mixed with isopropanol (IPA) with a typical concentration of the order of 1 g/L. The nanocrystals that form as part of the growth process for these wires are also present. Then this mixture is placed into a *Fisherbrand FB11002* ultrasonic bath at 20% power for 30 s to disperse the nanowires and nanocrystals in the IPA. This dispersion is drop cast onto the patterned substrate and the IPA is allowed to evaporate. This leaves the nanowires randomly distributed on the substrate along with the nanocrystals.

The density of the nanocrystals places an upper constraint on the concentration of the dispersion. If the dispersion is too dense then the quantity of this undesired material on the substrate will prevent contacting the nanowire to the pads and if it is too dilute then there will not be a sufficient number of contactable nanowires on the substrate. Each dispersion was made with an initial concentration of 1 g/L, which was found to always allow the contacting of some wires. The exact concentration varied as the ratio of nanoparticles to nanowires was found to be different in each dispersion. IPA was added or removed as necessary before each subsequent drop casting. In this way each dispersion was optimised. After the optimisation is complete there are typically about 20 to 30 nanowires out of a possible 36 on the substrate that may be contacted.

3.2.3 Electron beam lithography

The substrates are now coated with a positive electron beam resist. In early work a bi-layer comprising of a 300 nm layer of MMA (8.5) MAA 10% in ethyl lactate, followed by a 100 nm layer of 950K PMMA 3% in anisole was used. We later utilised a single 200 nm layer of 950K PMMA, 3% in anisole. In general bi-layers allow for easier lift off due to

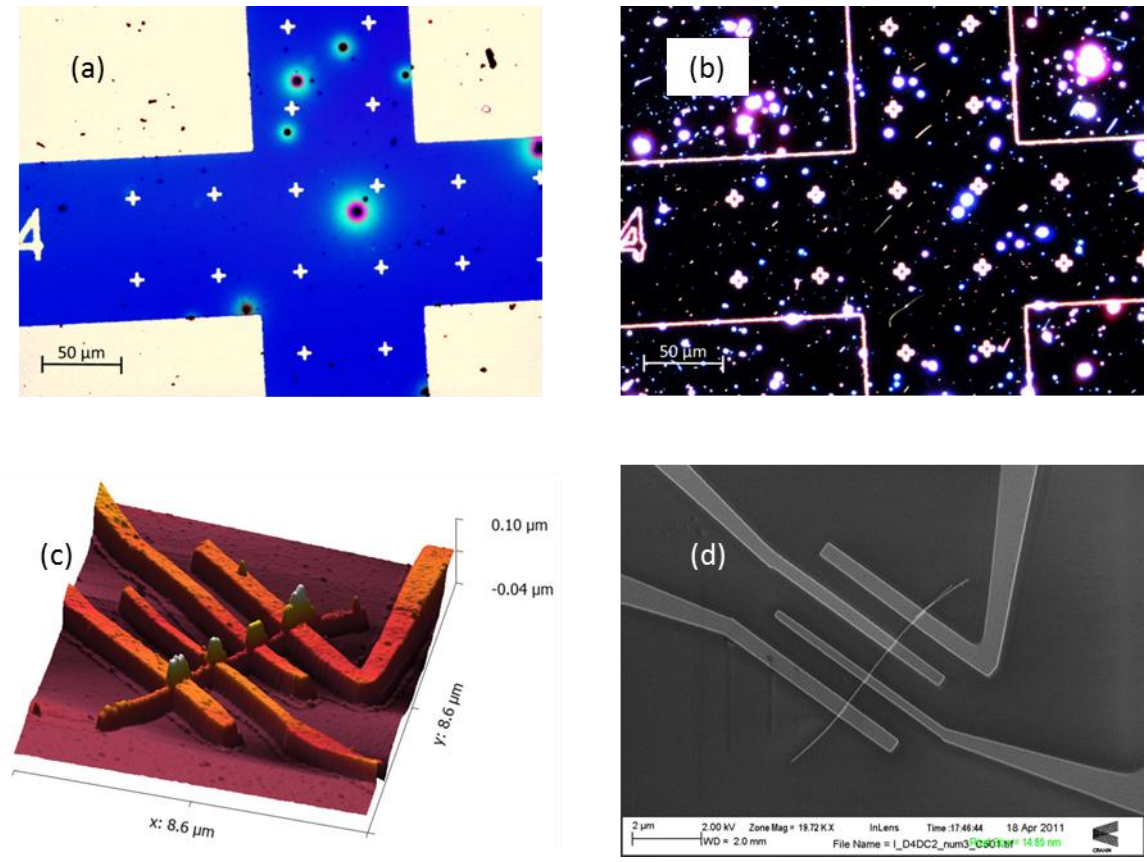

Figure 3.2 Images of a nanowire field effect transistor being created. (a) shows an optical image of a patterned SiO_2/Si substrate. The yellow squares in each corner are the bond pads, and the array of crosses that act as alignment marks for the electron beam lithography step are clearly visible. This sample has already had wires deposited, and some of the larger germanium crystals can be seen. (b) shows a dark field of the same sample that is shown in (a). Now only the edges of the bond pads and alignment marks can be distinguishd. In addition several straight green and yellow lines can be seen, as well as extra nanoparticles. These are the germanium nanowires. (c) and (d) show an AFM and an SEM image respectively of a contacted nanowire. Such images are used to ensure that devices consist of a single germanium nanowire.

the edge profile [3], while the single layer allows smaller features to be realised [3]. We switched from bi-layer to single layer to enable for contacting of smaller wires. Individual nanowires are identified in an optical microscope using the dark field setting. In dark field microscopy only scattered light is allowed into the objective lens. Flat areas therefore show up as black, while edges are clearly defined. As a result, the nanowires, which weakly scatter the light, are visible against the flat SiO_2 substrate. An example of such an image is shown in Figure 3.2 (b).

Using these images we create an electronic mask for the electron beam lithography process, which defines the electrodes joining the wire to the UV patterned pads. Electron beam lithography was performed primarily in the *Zeiss SUPRA*. Development is in an MIBK/IPA (1:3) solution for 50 s, after which the sample is rinsed in IPA and dried by blowing with nitrogen gas.

3.2.4 Removal of shell and metallisation for electrical contacting

It is necessary to remove the amorphous shell material that exists on these wires in order to electrically contact the germanium core. This is achieved with an argon ion etch prior to metal deposition. The etch and the deposition of the contacts take place in the *Temescal FC2000* without breaking vacuum. This is advantageous as it prevents a germanium oxide layer forming between the germanium and the electrode. The etch process involves argon atoms being ionised and accelerated through a voltage of 500 V towards the sample, which is placed approximately 1 m above the gun. The argon ions are deionised en route by a filament which the ions pass after exiting the gun. As the shell is made of an amorphous material it is removed at a much greater rate than the crystalline core material. Although the PMMA is itself amorphous an etch rate test showed that only 12 nm of PMMA was removed in a 60 s etch. This is not a sufficient amount to cause problems with regards to the masking of the sample. The etch is performed at this stage so that the shell is only removed under the contact area. The electron beam resist acts as a mask to ensure that only this part of the wire is exposed to the Ar atoms. The required etch times varied between wires grown under different conditions. This will be discussed in more detail in Section 4.1. After the etch electrode material is deposited by electron beam evaporation. Cobalt nickel and silver contacts were used, though no significant change to the electrical properties was seen upon

changing electrode material. This shall be important in the discussion of our results in Chapters 4 and 6.

3.3 Imaging of nanowires

3.3.1 Atomic force and optical microscopy

After device fabrication is complete atomic force microscopy (AFM) and/or dark field microscopy images of the devices are taken. This is done in order to ensure that the contacts are on the nanowire and that there is no material electrically shorting the contacts. It may also be possible to tell at this point if the nanowire which has been contacted is a bundle or a single wire. The AFM allows more high resolution imaging, but is significantly slower than the optical microscope. Images were taken using the *Asylum MFP-3D AFM*. Whenever an image is taken with the scanning electron microscope (SEM) hydrocarbons that are present in the sample chamber become deposited on the surface of the sample. For this reason the initial images of the devices are acquired in the AFM and optical microscopes before measurements are carried out and the SEM images are only taken when the measurements are complete. An AFM image of a finished device is shown in Figure 3.2 (c).

3.3.2 Scanning electron microscopy

It is important to know the core diameter as it allows us to calculate the resistivity of a given wire from the measured resistance value, as well as providing information with regard to any changes in observed effects with increased confinement. These images also provide the final confirmation, in addition to AFM images taken earlier, that a single wire as opposed to a bundle has been contacted.

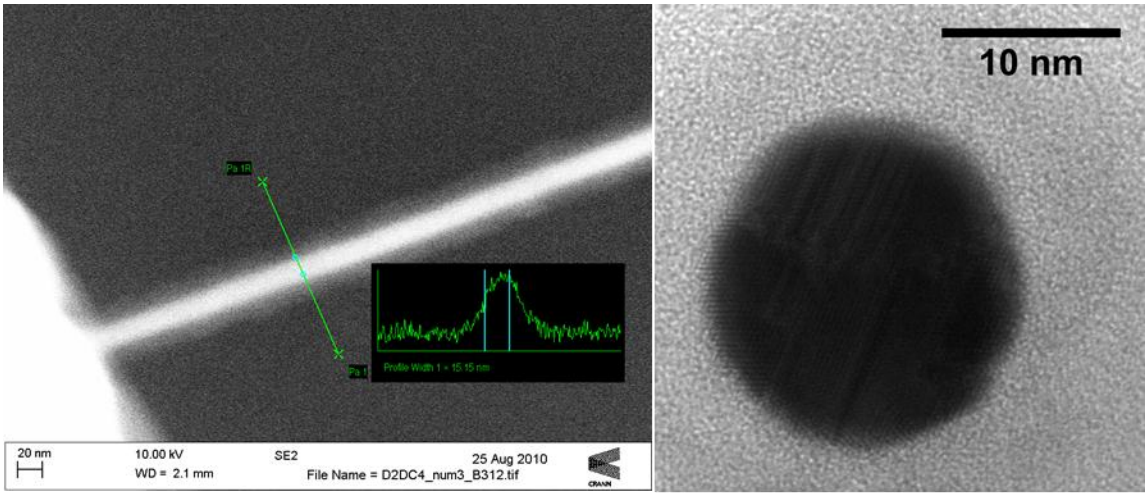

Figure 3.3 Comparisson of SEM and TEM images of a germanium core. (a) shows a nanowire imaged with a beam voltage of 10kV and a working distance of 2.1mm. The secondary electron detector was used. The bright area on the left is a nickel contact, while the white line across the image is the nanowire core. The lighter grey area around the core is the nanowire shell. From this image the nanowire core was determined to be 15 nm. (b) is a TEM image of the same wire taken by Richard Hobbs. The crystal structure of the core can be seen showing stacking faults. The diameter of the core was found to be 16 nm from this image, showing good agreement between the two methods for extracting the core diameter.

To reveal the core SEM images are taken at 8 to 10 kV accelerator voltage and a working distance of 2 mm in the *Zeiss ULTRA*. An example of an image taken in this way is shown in Figure 3.3 (a). This image was taken with the secondary-electron detector. This detects electrons ejected from the *K*-shell of the sample as a result of scattering from the incoming beam of electrons. A core diameter of 15 nm was extracted from the image shown in Figure 3.3 (a). Images may also be taken with the in-lens detector, which detects the electron from the beam that are scattered elastically from the sample. We take images with both detectors and take the average of the measured core diameters.

3.3.3 Transmission electron microscopy

The final method used for imaging the devices is transmission electron microscopy (TEM). The devices are sent to Richard Hobbs in University College Cork for this

purpose. The TEM images provide complementary information to the SEM images. The core and shell under the contact may also be imaged, to gain information about the Ar etch. The images also provide a second measurement of the core diameter in addition to the image from the two detectors on the SEM. A TEM image is shown in Figure 3.3 (b). This is the same wire as shown in the SEM image in Figure 3.3 (a). A core diameter of 16 nm was extracted from the TEM image, which compares well with the 15 nm found from the SEM images.

Taking the TEM images is a two step process. Firstly the devices must be milled using a focused ion beam (FIB). The second step is to image the thin lamellae created in this way. This process is therefore time and resource consuming. There is also the danger that the nanowire may be destroyed in either the FIB or the TEM before images can be obtained. Therefore, the SEM imaging is an elegant approach (Section 3.3.2) in order to circumvent these difficulties with TEM imaging.

We note that in the TEM image shown in Figure 3.3 (b) stacking faults are evident in the nanowire. In total TEM images were obtained for 5 separate nanowires, and only 1 showed signs of such defects. It has been reported that defects such as these are rare in nanowires grown using this seedless method [1, 2] (Section 3.1). The presence of such defects in the wires would lead to additional scattering, which we would measure as a reduced mobility and increased resistivity. It is not expected however that any of the experimental results that we see can be attributed to the presence of stacking faults.

3.4 Electrical measurement set up

Room temperature measurements were carried out with a probe station while temperature dependent measurements were made in a cryogen free cryostat from Cryogenic, capable of reaching temperatures of 1.6 K and magnetic fields of 9 T. The same electrical set up was used in both cases, a detailed circuit diagram of which is shown in Figure 3.4. All the green wires represent wires that are attached to the clean ground, which is shown as a thick green line at the bottom of the diagram. The green dashed rectangle in the middle is a custom made switch box which allows us to ground the sample between measurements. This ensures that the nanowires are not subject to any electrical shocks while the device is being wired. It is possible to ground each channel individually using the switches on the left, or to ground all lines simultaneously using the compound switch on the right, indicated by the dash-dot box. Further protection is provided to the device by the low pass RC filters indicated in dashed green boxes on the right. One is located between the source and the device, one between the device and the current to voltage pre-amplifier, and a final one on the circuit for the measurement of the 4 point voltage. Each filter consisted of a 5.1 MΩ resistor and a 10 nF capacitor, giving a time constant of 50 ms. These filters were designed to remove any 50 Hz noise from the line and to provide protection to the nanowires and preamplifier from any spikes in voltage that may appear in the circuit. A sufficient delay was allowed between applying a source voltage and measuring the resulting current and voltage drop to allow the capacitors in the filters to charge. Before every measurement the nanowire was replaced by a resistor of comparable resistance and

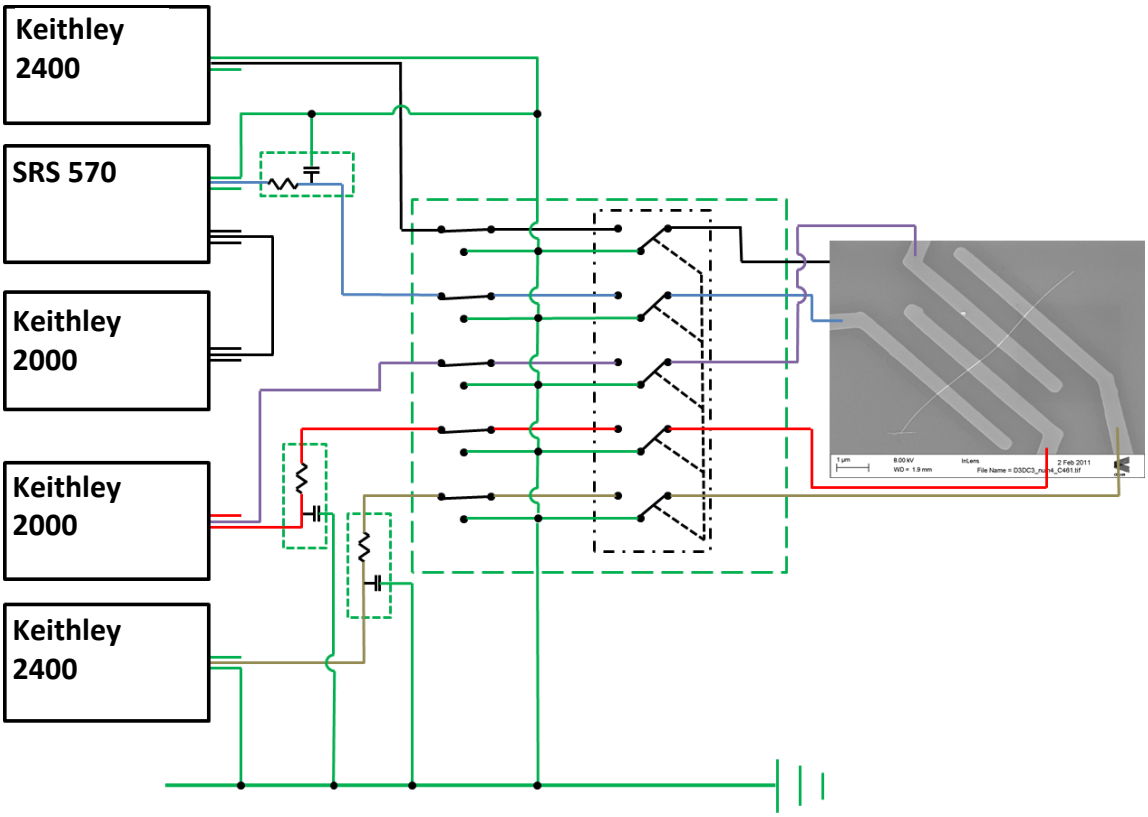

Figure 3.4 Circuit diagram of our electrical set up. We apply a voltage using the bottommost Keithley 2400 sourcemeter. The brown line indicates the high voltage line. An RC filter is placed on this line to protect the nanowire from any voltage spikes from thevoltage source. The blue line indicates the drain, where the current returns. The Stanford Research Systems SR570 current preamplifier measures the current flow from the blue line to ground, indicated by the green line. At the output it sets a voltage proportional to the measured current. We measure this voltage with a Keithley 2000 voltmeter. The voltage drop across the nanowire is measured between the purple and red wires with another Keithley 2000. Finally the black line indicates the back gate. A gate voltage may be applied and any leakage current measured using a Keithley, 2400.The large green dashed box in the middle is a custom made switch box that allows us to ground each channel either simultaneously using the compound switch indicated by the black dot-dash line, or individually using the switches on the left

.

the circuit was tested for fidelity.

Every wire outside of the main box and the RC filters were coaxial cables. Both the main box and the RC filters were located inside metal boxes, and the main switch box was tied to the clean earth. The outer shielding of every coaxial cable was thus grounded by its connection to the switch box, supplying shielding to the measurement current. This star-like arrangement ensured that there were no ground loops present in the set up. This also ensures that both sourcemeters were referencing the same

ground. The coaxial connections are indicated on the instruments on the left. The metallic shielding of the coaxial cables are extended over a wide range only were necessary for the sake of clarity in the diagram.

We used two *Keithley 2400* sourcemeters in our set up, one for the source and one for the back gate. As the name suggests these devices can source a voltage, while simultaneously measuring a current. We utilised this functionality to monitor the back gate for any significant leakage current. The sample current was measured using a SRS SR570 low noise pre-amplifier. This was required due to the fact that the 2 point resistance of our devices was of the order of 10-100 MΩ in most cases. We were therefore usually measuring currents of less than 100 nA. The voltage output of the preamplifier and the voltage across the inner two contacts of the wires were measured with a Keithley 2000 digital multimeter. The current measured by the sourcemeter should also agree with the current indicated by the *SRS SR570 pre-amplifier*/*Keithey 2000.* The agreement of these two numbers was checked to ensure that the currents measured were flowing through the nanowire, and not caused by a shorted RC filter, for example.

Each of the Keithleys was controlled by a range of custom made LabView programs. The programs allowed full automation for every type of measurement that we carried out.

References

[1] R.G. Hobbs, S. Barth, N. Petkov, M. Zirngast, C. Marschner, M.A. Morris, J.D. Holmes, Seedless growth of sub-10 nm germanium nanowires, Journal of the American Chemical Society, 132 (2010) 13742-13749.

[2] O. Lotty, R. Hobbs, C. O'Regan, J. Hlina, C. Marschner, C. O'Dwyer, N. Petkov, J.D. Holmes, Self-seeded growth of germanium nanowires: Coalescence and Ostwald Ripening, Chemistry of Materials, 25 (2013) 215-222.
[3] M.A. Mohammad, M. Muhammad, S.K. Dew, M. Stepanova, Fundamentals of electron beam exposure and development, in: Nanofabrication, Springer, 2012, pp. 11-41.

4. Variation in Electrical Response with Altered Growth Parameters

As discussed in Chapter 3 we measured wires grown under two different growth conditions. In this chapter we will compare and contrast the electrical characteristics of the two batches of wires [1]. We will first look at the removal of the shell material from the wires in Section 4.1. We shall see that the change in the growth conditions led to a difference in the ease of removal of the shell. The electrical results from the two batches will then be shown in Section 4.2. The final section will then give the details of a model that we developed to explain the memristive response that we observe in batch 1 wires.

4.1 Shell Removal

The only parameter that we vary from etch to etch is the time for which the sample is exposed to the argon atoms. Wires from batch 1 gave working devices when the etch time was 30 s, 45 s or 60 s. In batch 2 an etch of 30 s or more destroyed the wires completely. Etch times of 10 s to 20 s allowed the wires from batch 2 to be successfully contacted. It should be noted that 16 devices were created from the second batch which underwent an etch of 30 s or more. None of these gave current injection despite the fact that all appeared to be viable devices from AFM and SEM images. In total 32 wires were contacted without any etch. None showed any current injection, demonstrating the non-conducting nature of the shell.

[1] As a reminder: a third batch of wires were synthesised with growth characteristics identical to batch 2. No difference was seen in the electrical characteristics, so we do not differentiate between them (see Section 3.1).

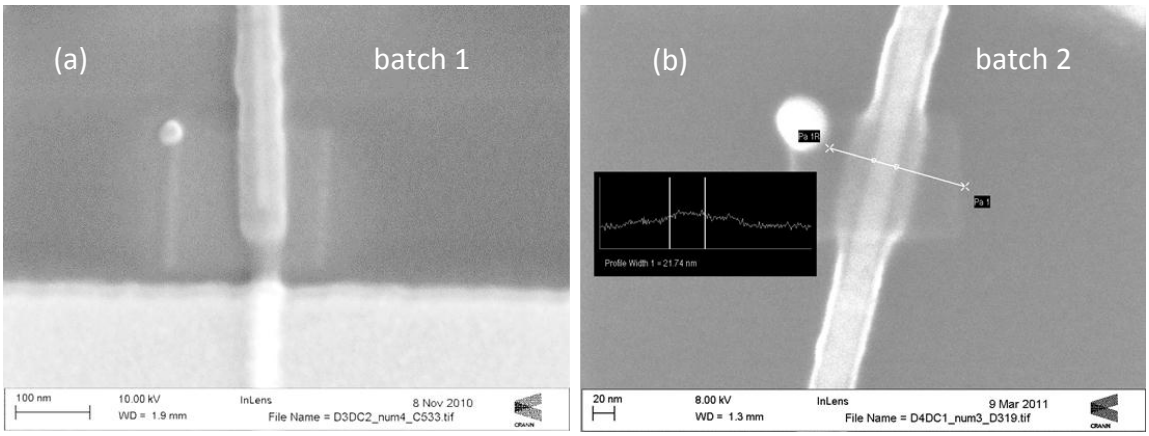

Figure 4.1 SEM image of wires from each batch showing the difference in the damage to the shell. The core and the shell can be distinguished in both images. The core is a straight bright area surrounded by a translucent material with rough edges, which is the shell. There is also a white circular spot evident in both cases. This is an area of contamination from the electron beam which marks the top left hand corner of an area that was previously imaged at higher magnification. It can clearly be seen in (b) that the shell of the wire from batch 2 has been damaged in the region where a higher magnification has been used, while no damage is evident in (a) for the wire from batch 1. In (a) the wire was over-etched by the argon gun, and a break in the core and shell can be seen at the bottom of the image.

Also it was observed that the shell of the batch 2 nanowires was damaged even under bombardment by the electrons in the SEM. An example of this is shown in Figure 4.1 (b). A square of contamination is evident in both images which marks an area that was previously imaged at a higher magnification. It is easy to identify the location of this square by the bright white spot on its top left corner. It can clearly be seen that the shell in this area has been damaged from the flux of electrons on the batch 2 wire in Figure 4.1 (b). The germanium core, visible as a bright area, shows no sign apparent of damage. In contrast, no damage to core or shell could be seen when wires from the batch 1 were imaged, as shown in Figure 4.1 (a).

It has been found that the thickness of the shell material depended on the growth parameters [1]. Wires grown at lower temperatures had thinner shells [1]. This is consistent with our observation that the shell on batch 2 was thinner and therefore easier to remove. Furthermore it has been reported that there exists germanium

Table 4.1 A summery of the main results from the two batches.

	Growth Conditions	Field effect	Memristive response	Conductance
Batch 1	425 ^{o}C for 15 hours	Yes. *p*-type	Yes	75 % of measured wires less than 14 nS
Batch 2	450 ^{o}C for 15 minutes, then 250 ^{o}C for 24 hours	No	No	72% of measured wires greater than 14 nS

crystals in the shell [1, 2]. These crystals are formed before the nanowires and eventually coalesce resulting in the nanowires that we measure, as discussed in Section 3.1. The crystals in the shell are of the order of 5 nm in diameter and can be seen in TEM images of the wires [1]. When the growth temperature of the nanowires is increased fewer crystals are seen in the final nanowires, as a greater quantity of the germanium from the precursor ends up in the nanowires [1, 2]. It is expected that the initial high temperature growth is sufficient to ensure that the majority of the germanium migrates to the nanowire cores and that there is therefore a smaller quantity of crystals in the shell of the batch 2 nanowires. This is also consistent with observation that the shell on the second batch is easier to remove.

4.2 Electrical measurements

In Figure 4.2 we show four graphs that summarise all of the main experimental results of this chapter. Figure 4.2 (a) and (b) are taken from a wire from batch 1 and Figure 4.2 (c) and (d) are taken from a wire from batch 2. The device functionalities that we will point out from these graphs are characteristics of the wires in that particular batch. It should be noted however that there is not a strict distinction between the behaviour of

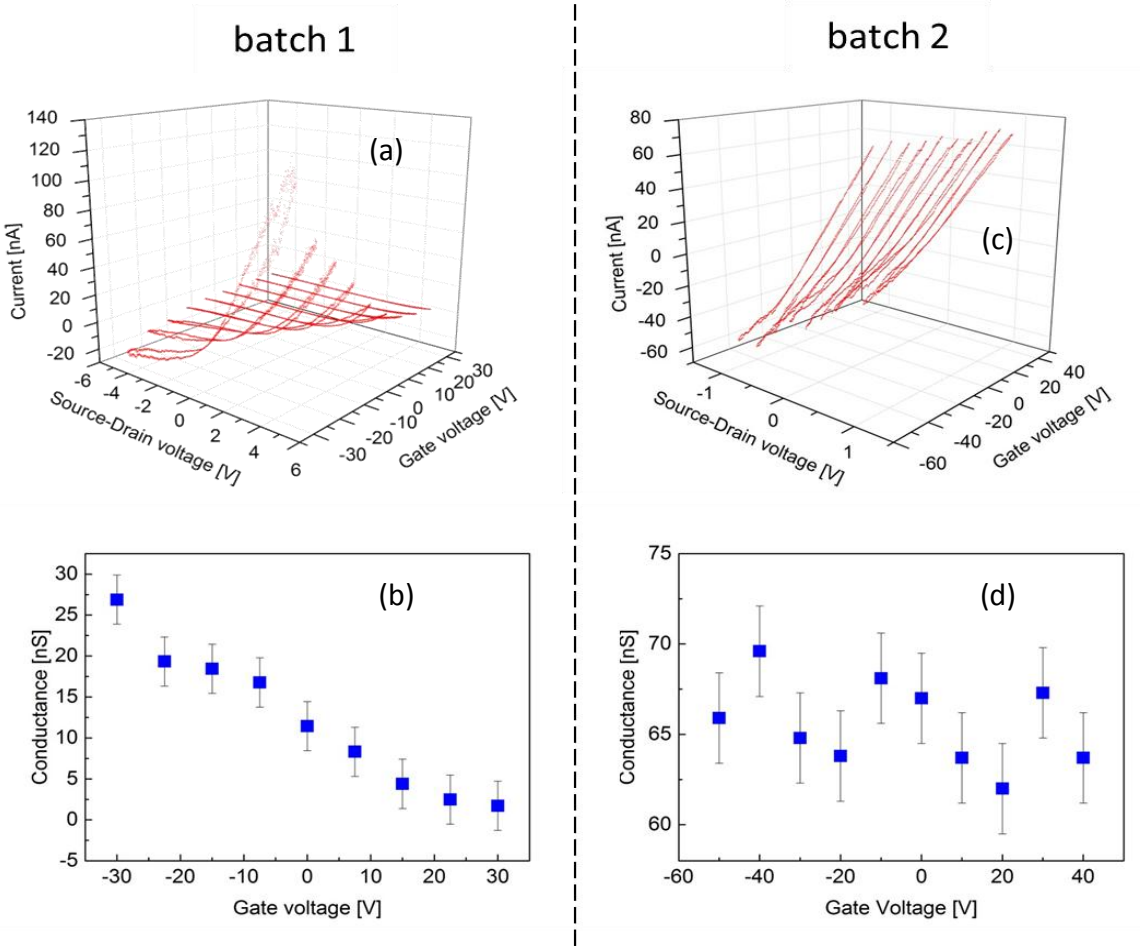

Figure 4.2 Difference in electrical characteristics of wires grown under two different growth conditions. (a) and (b) show results from batch 1. The graph in (a) is of source drain sweeps performed at different gate voltages, ranging from +30 V to -30 V. (b) shows the 2-point conductances extracted from the slope of the graphs with a positive source-drain voltage applied. A clear increase can be seen when a negative gate voltage in applied, suggesting *p*-type conduction. A memristive response is also seen in the plots, particularly at negative gate voltages. The plots (c) and (d) are of the same type, but the wire is taken from batch 2. It is clear from (c) that these graphs are much more linear, and there is no memristive response present. It can also be seen that there is little or no gate effect, which is confirmed by the extracted conductances, shown in (d). It should be noted that a wider range of gate voltages was applied to this sample. If the bulk conductivity is assumed conductances of 0.49 nS and 0.85 nS would be expected from the sample in (a) and (c), respectively. As can be seen from graphs (b) and (d) the value of conductance is higher in both cases in spite of the fact that these samples are measured in a 2-point configuration.

the two batches. That is to say that some batch 1 wires showed batch 2 like characteristics and *vice versa*. The characteristics that we associate with each batch is observed in the majority of wires in that batch, or is present much more prominently in that batch, but is not necessarily exclusive to the batch. Table 4.1 gives a summary of the main results from each batch.

Figure 4.2 (a) and (c) show 2-point source-drain sweeps carried out at different gate voltages. In Figure 4.2 (a) the device shows clear *p*-type behaviour, with increasing current at negative gate voltages. This is in contrast to the device shown in Figure 4.2 (c), which showed little or no change in conductance with changing gate voltage. To underline this fact we have extracted the conductance of each of the curves and plotted this against the gate voltage in each case, as shown in Figure 4.2 (b) and (d), corresponding to the graphs in Figure 4.2 (a) and Figure 4.2 (c) respectively. For Figure 4.2 (b) we extracted the conductance from the linear region with positive source drain voltage applied, near 2 V source-drain voltage. It should be noted that the gate voltage was swept to $\pm$ 30 V for the device shown in Figure 4.2 (a), while the device in Figure 4.2 (c) was tested to -40 V and $+50$ V. The former nonetheless shows a conductance change of approximately 25 nS, while in the latter only a change of at most 10 nS is evident, in spite of the greater range of gate voltages used.

It can also be seen that the current-voltage characteristics of the sample from batch 2 is linear, in contrast to the sample from batch 1 which shows a clear non-linearity and hysteresis. This type of curve is known as a pinched hysteresis loop due to the fact that it passes through the origin and is indicative of memristance [3, 4], as discussed in Section 2.6.

The third point to note is that the value of the conductance in wires from batch 2 is higher than the value of wires from batch 1 for the majority of samples. This is evident from the extracted conductances shown in Figure 4.2 (b) and (c). In total we measured eight wires from batch 1 and thirty-six wires from batch 2 in a four point configuration. Measuring a sample in four point configuration allows us to extract the

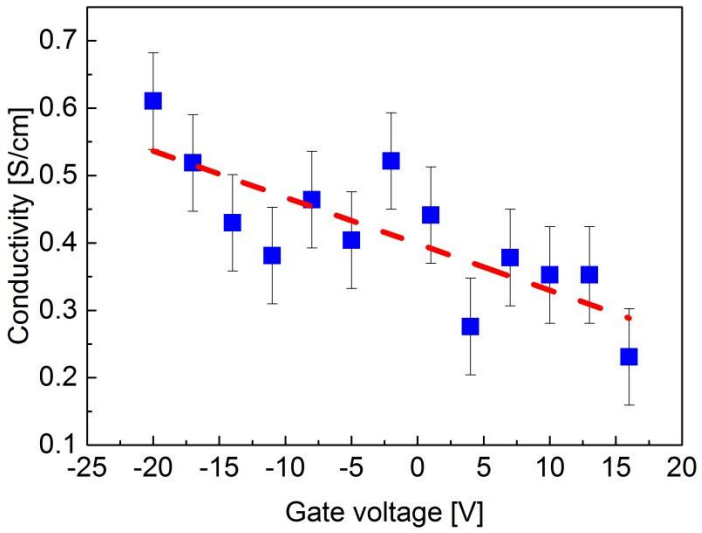

Figure 4.3 Extracted conductivity plotted against gate voltage for a wire grown in batch 1 which was measured in a four point configuration to eliminate contact resistances. The red line is a linear fit. From the slope of this line we can extract the mobility and the carrier concentration of this sample using Eq 2.12, finding a value of 9.6×10^{-2} $cm^2V^{-1}s^{-1}$ for the former and 4.9×1019 cm^{-3} for the latter when no gate voltage is applied.

wire conductance without any contact effects. Six wires from batch 1 (75%) had a conductance below 14 nS, while in batch 2 twenty six wires (72%) out of the thirty- six measured had a conductance in excess of 14 nS. This demonstrates the fact the conductance of wires in batch 2 was usually higher than that seen in batch 1.

In Figure 4.3 we plot the conductivity of a wire from batch 1 as a function of gate voltage. Conductivity is calculated from Eq. 2.6, using the resistance value measured in a 4-point configuration (Section 2.1.1) and geometric factors determined from SEM images (Section 3.3.2). In all cases, from both batches, the extracted conductivity was an order of magnitude or more greater than the bulk conductivity of 0.02 S/cm [5], as it is in Figure 4.3. Furthermore in all cases where we made a two point measurement the measured conductance is higher than would be expected if the wire retained the bulk value for conductivity. For example in Figure 2 (b) and (d) 2-point

conductance values of 0.49 and 0.85 nS respectively would be expected at zero gate voltage. Instead we measure values of 11.4 in Figure 2 (b) and 67 nS in Figure 2 (d) despite the contact resistance contribution.

Increased conductivity can be the result of increased mobility or increased carrier concentration or both. The mobility μ from a batch 1 nanowire can be calculated from the slope of a graph using Eq. 2.12 in Section 2.1.2. We found mobilities of the order of 10^{-3} to 10^{-1} $cm^2V^{-1}s^{-1}$. The mobility of holes in bulk germanium is 1.9×10^2 $cm^2V^{-1}s^{-1}$ [6], far in excess of the mobility that we observe. Therefore the carrier concentration in our wires must be greatly increased with respect to the bulk value, in order to account for the high value of the conductivity observed.

From the graph in Figure 4.3 and the known nanowire geometry we calculate the mobility of this sample to be 9.6×10^{-2} $cm^2V^{-1}s^{-1}$. From the value of the conductivity we find the carrier concentration to be 4.9×10^{19} cm^{-3} at zero applied gate voltage. The wires are grown to be nominally intrinsic, so there are no intentional dopants present in the core. As stated in Chapter 3 the shell consists mainly of silicon, with some germanium, carbon, oxygen and hydrogen also present [2]. Silicon and carbon are both group IV elements and therefore do not dope germanium. Oxygen and oxygen-hydrogen complexes both act as *n*-type dopants in germanium and so cannot be the source of the *p*-type doping that we observe [7, 8]. Therefore the source of the high charge carrier concentration in the core of the nanowire are charge traps at the surface of the germanium. It has long been known that the density of charge traps at the germanium surface that lead to doping can be as high as the density of surface atoms [9]. The density can be greatly reduced by functionalization of the surface [10]. It was

reported that the density of surface states due to an oxide layer was 10^{13} cm^{-2} or higher [9], and that the surface states lead to a heavily doped *p*-type region at the surface of the germanium [9]. For a nanowire with a diameter of 20 nm, this would lead to a carrier concentration of the order of 10^{19} cm^{-3}, in agreement with our experimentally observed value.

It should be noted that although the mobility that we measure in our wires is very low compared to the value expected in bulk germanium, it is commensurate with the value of mobility reported for unpassivated germanium nanowires in other studies [11, 12]. This is believed to be due to the scattering from the trapped charges at the interface [11-14]. Furthermore, as discussed in Section 2.1.2, the mobility that we measure here is a lower bound on the value due to the inadequacies of the cylinder on plane capacitor model and the screening effect of the surface states. This in turn means that the calculated carrier concentration is an upper bound on the true value.

Germanium begins to become degenerately doped at a doping density of 10^{19} cm^{-3} [15-17]. It is increasingly likely to undergo a metal-insulator transition at doping levels above 10^{19} cm^{-3}, at which point it may be considered quasi-metallic [18, 19]. This suggests that the difference in the functionalities of these wires arises from a difference in their doping levels. The wires from batch 2 behave as quasi-metallic, showing the lack of a field-effect, and an increased conductivity compared to the batch 1 wires. Since the core of the nanowires from each batch is identical, this disparity can only stem from the difference of the shell material. This difference results in a modification in the number of available core/shell interface states, and hence alters the doping of the wires, which leads to the observed electrical behaviours.

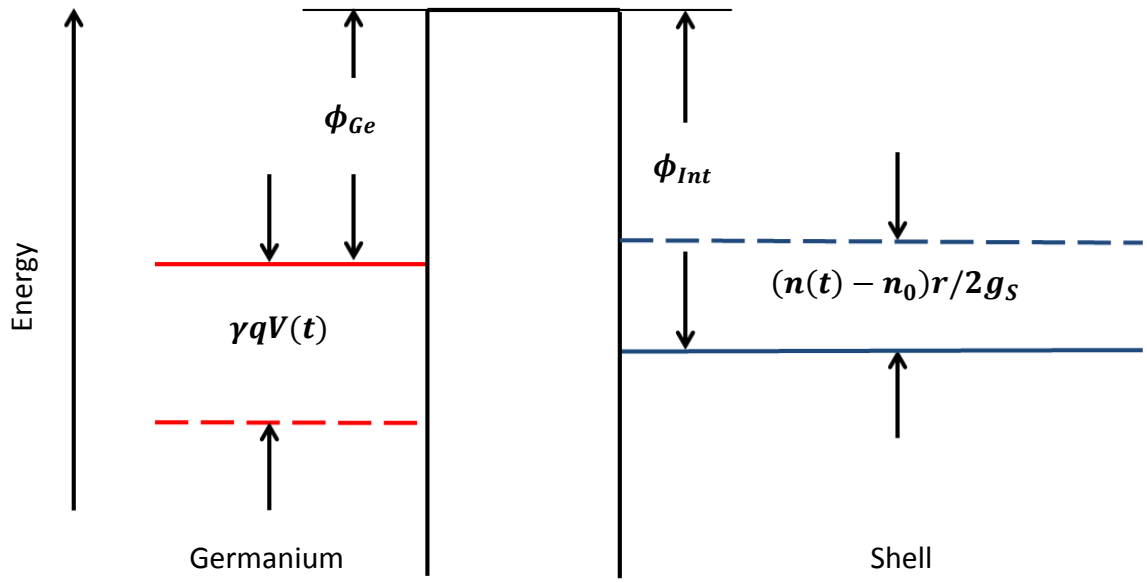

Figure 4.4 Schematic diagram of the underlying mechanism of the memristor model ds described in the main text for batch 1 nanowires. The solid lines represent the situation at equilibrium with no voltage applied. In the germanium this is the Fermi level, while in the shell this is the highest occupied state. The dashed lines show how these levels are changed when a voltage is applied such that electrons have been removed from the germanium core and added to the shell.

4.3 Memristance model

We attribute the memristance to the transfer of electrons into and out of the interface states. Here we develop a simplified model to show this specific memristive behaviour, which qualitatively reproduces the data. In principle for any electron to enter one of the charge traps at the interface it must overcome a potential barrier. With the system at equilibrium and no source voltage applied the height of this barrier shall be denoted as ϕ_{Ge}. When, at a time, t, a source drain voltage, $V(t)$, is applied the barrier height will be changed by an amount $\gamma qV(t)$, where q is the charge of the electron, and γ is a factor between 0 and 1 that accounts for the voltage drop across the contacts. The electrons will now need to overcome a barrier height of $\phi_{Ge} + \gamma qV(t)$. This situation is depicted on the left hand side of Figure 4.4, where the solid red line shows the Fermi level with no voltage is applied, and the dashed line is the case after applying voltage.

The average time that it takes for an electron to overcome the barrier can be estimated by:

$$\tau_{Ge}(t) = \tau_0^{(Ge)} e^{\frac{\phi_{Ge}+\gamma q V(t)}{k_B T}}, \quad \text{Eq. 4.1}$$

where $\tau_0^{(Ge)}$ is a time constant, k_B is Boltzmann's constant and T is the temperauture.

It should be noted that the barrier height may not in fact be constant along the length of the nanowire. It may, for example, differ due to local non-uniformity of the shell. In addition the effects of thermal broadening should be taken into account as all of our measurements were carried out at room temperature. For the sake of simplicity we use a single value here, which may be considered to be a weighted average of the value at all points in the wire.

The voltage drop across the Schottky barriers at the contacts will principally determine the value of γ. As discussed in Section 2.4.3 the voltage drop across a Schottky barrier has a complicated relationship to the voltage applied across the contact. It was also discussed that in the case of side contacted nanowires Fermi level pinning is significantly alleviated [20, 21] and the barrier height at the contact depends predominantly on the metal work function. In general the work function of a metal can take a range of values depending, for example, on which crystal surface is measured [22]. We contacted each wire either with nickel or cobalt. Nickel has a work function in the range of 5.04 to 5.35 eV [22]. The work function of cobalt is approximately 5 eV, however more specific details are not reported in the literature [22]. Due to the polycrystalline nature of our contacts we do not know which crystal surface is in contact with the wire. As a result the Schottky barrier height and the ideality factors for

the source and the drain contact may be different leading to an asymmetric current-voltage curve in a 2 point configuration, as we discussed in detail in Section 2.4.3.

This process of electrons overcoming the barrier leaving behind free holes in the germanium will be counteracted by electrons jumping out of the surface states back into the wire and recombining with the holes. The literature shows that for slow states this time can be in the range of thousands of seconds at room temperature [9, 12, 23]. The barrier height for the electrons to overcome in moving from the shell to the core is given by $\phi_{Int} - (n(t) - n_0)r/2g_S$, where ϕ_{Int} is the barrier height that an electron at the interface needs to overcome in order to get back into the germanium core when the wire is at equilibrium and no voltage is applied, n_0 is the initial hole concentration in the core, $n(t)$ is the hole concentration at a time t, r is the radius of the nanowire and g_S is the density of states in the shell. The second term accounts for the fact that as more electrons are added to or removed from the shell the effective height of the barrier changes, as depicted on the right hand side of Figure 4.4. Here the solid line depicts the height of the highest occupied level when no voltage is applied and the system is in equilibrium. The dashed line shows the highest occupied level after a voltage has been applied and electrons have been added to the shell. We assume that the number of electrons in the interface states is equal to the number of mobile holes in the core and for simplicity we also take the density of states in the shell to be constant. The factor of $r/2$ is required to convert the hole density in the core (in cm^{-3}) to surface states density (in cm^{-2}). The average time for recombination will be given by:

$$\tau_{Int}(t) = \tau_0^{(Int)} e^{\frac{\phi_{Int} - (n(t) - n_0)r/2g_S}{k_B T}}, \qquad \text{Eq. 4.2}$$

where $\tau_0^{(Int)}$ is a time constant. Again the barrier height in Eq. 4.2 should be considered to be a weighted average as in Eq. 4.1.

In equilibrium these two processes will be balanced, leaving a constant number of holes in the wire. The change in the hole concentration in the core during a short time, δt, is simply given by the difference between the number of electrons entering the core/shell interface states and the number of electrons leaving these states:

$$\begin{aligned} \Delta n(t) &= n(t) - n(t-\delta t) \\ &= \frac{n_{Ge}(t-\delta t)\delta t}{\tau_{Ge}(t-\delta t)} - \frac{n(t-\delta t)\delta t}{\tau_{Int}(t-\delta t)} \end{aligned} \qquad \text{Eq. 4.3}$$

where $n_{Ge}(t)$ is the concentration of the electrons in the germanium at a time t, given by:

$$n_{Ge}(t) = n_{Ge}(t-\delta t) - \Delta n(t). \qquad \text{Eq. 4.4}$$

If we know the initial carrier concentration we can now calculate the carrier concentration at any later time. If we set the voltage and Δn equal to 0, the initial electron concentration in the germanium is given by:

$$n_{Ge}^{(0)} = \frac{n_0 \tau_{Ge}(0)}{\tau_{Inter}(0)}. \qquad \text{Eq. 4.5}$$

Using Eq. 4.1 to Eq. 4.5 the number of free carriers at any given time can be calculated. Assuming that the mobility remains constant, the resistance of the wire is then known.

Let us briefly examine the theory in the limit of a continually varying signal. The resistance at any given time will depend on $n(t)$, which will in turn depend on the value of the applied voltage and on time. We may therefore write:

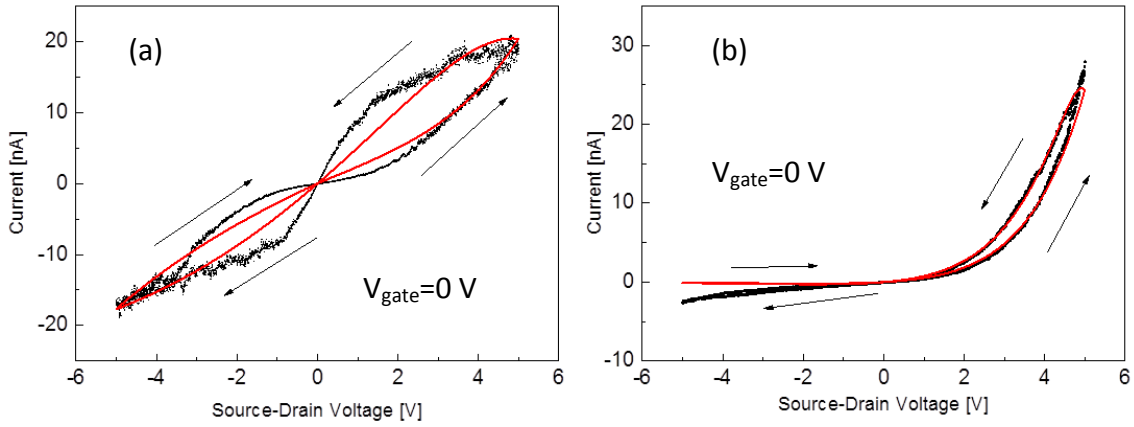

Figure 4.5 Comparisson between memristive device theory and experimentel curves. Source-drain voltages measured on two different samples, both taken from batch 1, and both measured with no gate voltage applied. In both cases the measurement lasted approximately 30 minutes. The black points are experimental data and the solid red line is a fit to the theory. It can be seen that the pinched hysteresis loop shown in (a) is much more symmetrical than the one shown in (b). It can be clearly seen that the theory reproduces the experimental data qualitatively, including the asymmetry seen in samples (b). Such an asymmetry was present in the majority of our devices, as can be observed in Figure 2 (a), for example. Our model suggests that at least part of the experimentally observed asymmetry results from the difference in the heights of the barrier for transferring into and out of the shell implying that the real barrier is asymmetric. In the model for (a) the two heights were set to be the same, as shown in Table 2.

$$v = R(n, v, t)i. \qquad \text{Eq. 4.6}$$

where we are using lower case letters to signify the fact that we are examining an AC signal. Rearranging Eq. 4.3 we find:

$$\lim_{\delta t \to 0} \frac{\Delta n}{\delta t} = \frac{dn}{dt} = \frac{n_{Ge}(t)}{\tau_{Ge}(t)} - \frac{n(t)}{\tau_{Int}(t)}. \qquad \text{Eq. 4.7}$$

In Section 2.6 we gave the two defining equations for a memristive system Eqs. 2.52. Eq. 4.6 is identical to the first of these with the state variable x equal to the concentration of trapped electrons, n. Eq. 4.7 is identical to the second defining equation with $f(n, v, t)$ equal to the right hand side of Eq. 4.7. The explicit voltage dependence comes from $\tau_{Ge}(t)$ given by Eq. 4.7. This shows that our model describes a voltage controlled memristive device.

Table 4.2 Parameters used for model curves shown in Figure 4.5**.**

	Figure 4.5 (a)	Figure 4.5 (b)	Units
ϕ_{Ge}	0.34	0.41	eV
$\tau_0^{(Ge)}$	0.2	0.0005	s
ϕ_{Int}	0.34	0.175	eV
$\tau_0^{(Int)}$	0.0046	0.02	s
g_S	1.6×10^{12}	4×10^{17}	$eV^{-1}\,cm^{-2}$
γ	0.01	0.015	Unitless
n_0	10^{19}	10^{19}	cm^{-3}
δt	0.25	0.25	s

A comparison between the experiment and theory is shown in Figure 4.5, for two different samples from batch 1 measured at zero-gate voltage. The fitting parameters used in both of these curves are given in Table 4.2. In both cases the height of the barrier is of the order of a few hundred meV. This is large enough to ensure that not all states are filled at room temperature (thermal energy 25 meV), but is smaller than the band gap of germanium, (0.67 eV [24]), which must be true for states in the gap. In addition the barrier height and the time constant give a trapping time for the surface states from Eq. 4.2. For the curve in Eq. 4.5 (a) a trapping time between 2400 and 2350 s was found over the course of the measurement while times between 14 and 15 s were calculated for the curve in Eq. 4.5 (b). The trapping time for a slow state can vary greatly depending on the details of the surface and have been found to exist in both of these ranges [9, 12]. It can be seen that the two barrier heights are equal for

the fitting of Eq. 4.5 (a), but differ by a factor of ~2.5 for the fitting of Eq. 4.5 (b). It is this difference that leads to the near symmetric current-voltage characteristics seen in the former sample as opposed to the asymmetric response seen in the latter. Our theory predicts a density of surface states which is of the order of 10^{12} eV^{-1} cm^{-2} for Figure 4 (a) and 10^{17} eV^{-1} cm^{-2} for Figure 4 (b). It has been found that the density of traps at the interface between epitaxially grown silicon and germanium is of the order of $10^{12} – 10^{14}$ eV^{-1} cm^{-2} at room temperature [25]. It should not be surprising that our density may be somewhat higher than was found at the interface with a well-controlled crystalline layer. For the initial carrier concentration we took a value of 10^{19} cm^{-3} in both cases in agreement with the previously discussed experimental results. Finally, we note that in four point measurements we regularly observe a voltage drop across the wire of the order of 10 mV when a source drain voltage of the order of 1 V is applied, justifying our choice of 0.01 or 0.015 for α.

Remarkably we can see that both the memristance and the asymmetry of the curve are both qualitatively well reproduced, despite the many simplifications in the model. As already discussed we took a single effective height for the barriers between the core and shell and assumed a constant density of core/shell interface states as well as neglecting the details of the Schottky barriers at the contact interfaces. In particular it should be noted that the asymmetry of the current-voltage curves is well reproduced in spite of the fact that we took γ to be a constant. In our model the asymmetry stems from a difference in the barrier heights. This implies that the experimentally observed asymmetry has a large contribution from the asymmetry in the real barrier heights. The fact that good agreement is obtained in spite of these simplifications and omissions

suggests that the basic mechanism causing the observed memristive response is transfer of electrons between the core and the core/shell interface states.

References

[1] O. Lotty, R. Hobbs, C. O'Regan, J. Hlina, C. Marschner, C. O'Dwyer, N. Petkov, J.D. Holmes, Self-seeded growth of germanium nanowires: Coalescence and Ostwald Ripening, Chemistry of Materials, 25 (2013) 215-222.
[2] S.B. Richard G. Hobbs, Nikolay Petkov, Michaela Zirngast, Christoph Marschner, Michael A. Morris, and Justin D. Holmes, Seedless Growth of Sub-10 nm Germanium Nanowires, Journal of the American Chemical Society, 132 (2010) 13742–13749.
[3] L.O. Chua, S.M. Kang, Memristive devices and systems, Proc. IEEE, 64 (1976) 209-223.
[4] L.O. Chua, Memristor - the missing circuit element, IEEE Trans. Circuit Theory, 18 (1971) 507-519.
[5] A. Levitas, Electrical Properties of Germanium-Silicon Alloys, Physical Review, 99 (1955) 1810.
[6] S.M. Sze, Physics of Semiconductor Devices, Wiley, New York, 1981.
[7] C.S. Fuller, W. Kaiser, C.D. Thurmond, Donor equilibria in the Germanium-oxygen system, Journal of Physics and Chemistry of Solids, 17 (1961) 301-307.
[8] P. Deák, B. Schröder, A. Annen, A. Scholz, Oxygen-hydrogen donor complexes in germanium, Physical Review B, 48 (1993) 1924-1927.
[9] R.H. Kingston, Review of Germanium Surface Phenemena, Journal of Applied Physics, 27 (1956) 101.
[10] T. Hanrath, B.A. Korgel, Chemical Surface Passivation of Ge Nanowires, Journal of the American Chemical Society, 126 (2004) 15466-15472.
[11] A.D. Schricker, S.V. Joshi, T. Hanrath, S.K. Banerjee, B.A. Korgel, Temperature dependence of the field effect mobility of solution-grown germanium nanowires, The Journal of Physical Chemistry B, 110 (2006) 6816-6823.
[12] T. Hanrath, B.A. Korgel, Influence of Surface States on Electron Transport through Intrinsic Ge Nanowires, The Journal of Physical Chemistry B, 109 (2005) 5518-5524.
[13] J. Lee, H.N. Spector, Impurity-limited mobility of semiconducting thin wire, Journal of applied physics, 54 (1983) 3921-3925.
[14] S. Jin, M.V. Fischetti, T. Tang, Modeling of electron mobility in gated silicon nanowires at room temperature: Surface roughness scattering, dielectric screening, and band nonparabolicity, Journal of Applied Physics, 102 (2007) 083715-083715-083714.
[15] D. Meyerhofer, G.A. Brown, H.S. Sommers, Degenerate Germanium. I. Tunnel, Excess, and Thermal Current in Tunnel Diodes, Physical Review, 126 (1962) 1329-1341.
[16] J. Sharp, W.J. Lee, K. Ploog, G.A. Umana-Membreno, L. Faraone, J.M. Dell, A novel technique for degenerate p-type doping of germanium, Solid-State Electronics, 89 (2013) 146-152.
[17] J.I. Pankove, P. Aigrain, Optical Absorption of Arsenic-Doped Degenerate Germanium, Physical Review, 126 (1962) 956-962.

[18] N.F. Mott, A.S. Alexandrov, Sir Nevill Mott: 65 years in physics, World Scientific, 1995.
[19] M.N. Alexander, D.F. Holcomb, Semiconductor-to-Metal Transition in *n*-Type Group IV Semiconductors, Reviews of Modern Physics, 40 (1968) 815-829.
[20] M.M. Koleśnik-Gray, T. Lutz, G. Collins, S. Biswas, J.D. Holmes, V. Krstić, Contact resistivity and suppression of Fermi level pinning in side-contacted germanium nanowires, Applied Physics Letters, 103 (2013) 153101.
[21] F. Léonard, A.A. Talin, Size-Dependent Effects on Electrical Contacts to Nanotubes and Nanowires, Physical Review Letters, 97 (2006) 026804.
[22] D.R. Lide, CRC handbook of chemistry and physics, CRC press, 2004.
[23] R.H. Kingston, A.L. McWhorter, Relaxation Time of Surface States on Germanium, Physical Review, 103 (1956) 534-540.
[24] S.M. Sze, Semiconductor Devices: Physics and technology, John Wiley & Sons, New York, 2002.
[25] J. Mitard, K. Martens, B. DeJaeger, J. Franco, C. Shea, C. Plourde, F. Leys, R. Loo, G. Hellings, G. Eneman, Impact of Epi-Si growth temperature on Ge-pFET performance, in: Solid State Device Research Conference, 2009. ESSDERC'09. Proceedings of the European, IEEE, 2009, pp. 411-414.

5. Diameter Dependence of the Resistivity of Quasi-Metallic Germanium Nanowires

We examine in this chapter the change in the resistivity of the germanium nanowires from batch 2 which showed little or no gate effect as a function of the core diameter. In Section 5.1 we shall briefly discuss the experimental results. Sections 5.2 and 5.3 will then give details of the calculations that we carried out to model the findings. We shall show that there are two different regimes that need to be considered: Above approximately 20 nm the mobile holes are predominately confined to an annular region close to the surface of the nanowire core, while below this diameter the holes are found throughout the entire core of the nanowire. In both cases the total carrier concentration will vary with diameter as a result of the difference in scaling between the volume in which the charge carriers can move and the number of surface states. This will be discussed in detail in Section 5.2. For wires with diameters less than 20 nm we will model the mobility using the one-dimensional Kubo-Greenwood formula, Eq. 2.48. Details of this calculation will be given in Section 5.3. Finally theory and experiment will be compared in Section 5.4.

5.1 Experimental findings

Figure 5.1 shows the resistivity of 32 germanium nanowires from batch 2 as a function of nanowire diameter. The two graphs contain the same data – Figure 5.1 (b) is simply a zoomed in image of the wires with diameters less than 25 nm. All measurements are performed at room temperature and the resistivity is extracted from measurements with no gate voltage applied. All data are taken from 4-point measurements as described in Section 2.1.1 and Section 3.4 and the resistance is extracted from the

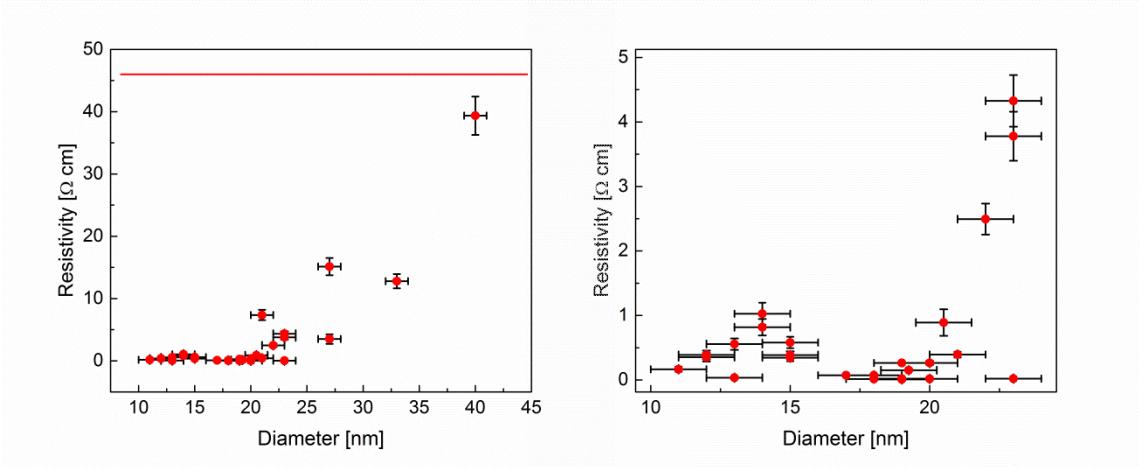

Figure 5.1 Diameter dependence of the resistivity of batch 2 wires showing little or no gate effect. (a) Shows the full data set, while (b) shows the data for the wires below 26 nm. All the data are taken from wires from batch 2 at room temperature with no gate voltage applied. The red line in (a) shows the value of resistivity in bulk germanium, and it can be seen that the value of the resistivity measured is lower in all cases. A clear trend is observed, with the resistivity decreasing as the diameter becomes smaller, with the value saturating at less than 1 Ωcm for wires with diameters below approximately 20 nm. The error on the resistivity comes from the error in measuring the diameter of the wires accurately and also from the least-squared fit to the IV curves. A difference in the resistivity of two wires with the same diameter may result from a difference in the density of surface states. This is not included in the calculation of the error bars.

linear part of the graph where low source-drain voltage is applied. The wires are all from batch 2, and data with nickel, cobalt and silver contacts are shown. No systematic difference is seen when the contacts are changed. The red line in Figure 5.1 (a) indicates the value of resistivity of intrinsic bulk germanium at room temperature, 46 Ωcm [1]. It can be seen that the value of the resistivity of every nanowire measured was significantly lower than this, as we discussed in Section 4.2.

The value of the resistivity decreases rapidly as the diameter of the nanowire is lowered from 40 nm to approximately 20 nm. For the largest diameter nanowire with a diameter of 40 $\pm$ 1 nm, a resistivity of 39 $\pm$ 3 Ωcm was measured, which is close to the value of bulk resistivity. The wire with the lowest resistivity had a diameter of 19 $\pm$ 1 nm and a resistivity of 0.009 $\pm$ 0.002 Ωcm, that is, five orders of magnitude lower.

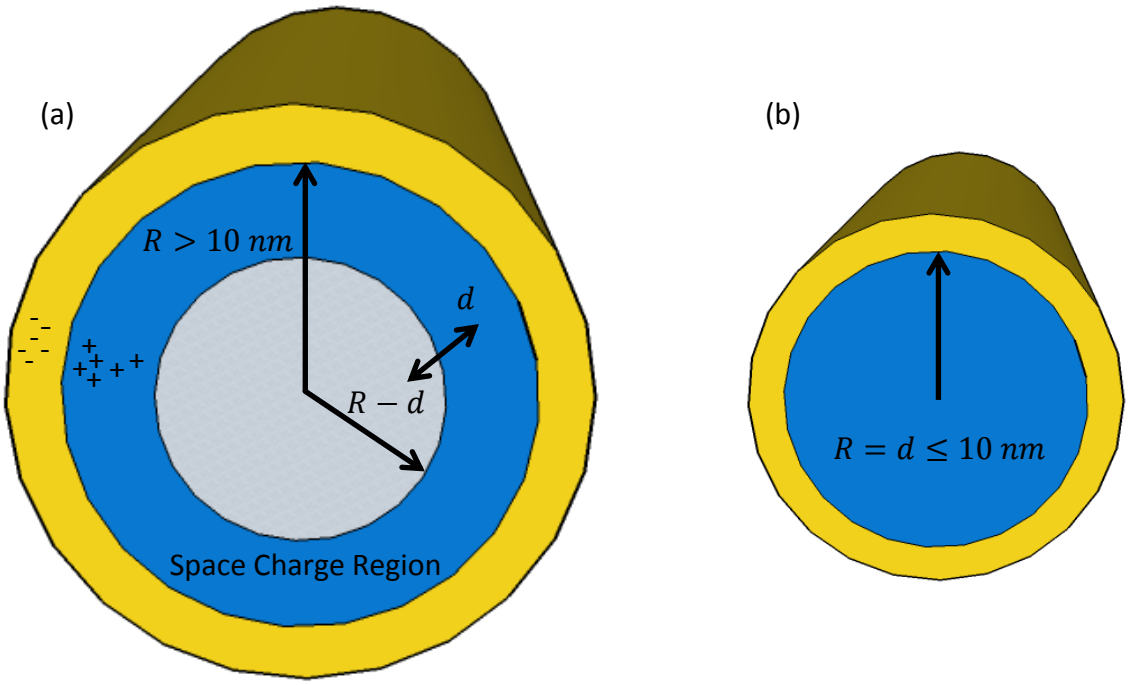

Figure 5.2 Schematic diagram of the volume in which holes are predominantly located for (a) a wire with a diameter above 20 nm (regime 1)and (b) a wire with a diameter less than 20 nm (Regime 2). In both graphs the thin yellow region at the outside represents the shell of the nanowire, and the blue area is the region in which the free holes are located. In (a) $\boldsymbol{d < R}$ and this results in a region in the centre of the wire in which there are no free carriers. This is shown in grey. The free holes in this case are confined to a space charge region near to the core/shell interface. On the left of (a) we schematically depict the trapped electrons (-) and free holes (+). In (b) the free hols are found across the whole cross section of the nanowire.

Below about 20 nm this trend no longer holds. The resistivity shows a peak-like feature at a diameter of approximately 14 nm, with the highest point being at a resistivity of 1.0 ± 0.2 Ωcm, for a wire with a 14 ± 1 nm diameter.

5.2 Carrier Concentration and Associated General Resistivity Expressions

The number of free holes in the core of the nanowire will depend on the number of charge traps at the core/shell interface as discussed at length in Chapter 4. We assume for simplicity that the total number of carriers from the surface states, N_{ss}, is equal to the total number of occupied surface states, given by:

$$N_{ss} = 2\pi l R n_{ss}, \qquad \text{Eq. 5.1}$$

where R is the radius of the nanowire, n_{ss} is the density of occupied surface states and l is the length of the wire. Eq. 5.1 shows that the number of carriers is linearly proportional to the radius if the density of surface states is constant. We assume that the surface state density is constant for all wires grown with the same growth conditions. The resistivity depends not on the carrier number, as given by Eq. 5.1, but on the carrier concentration as can be seen from Eq 2.5[1]. To find the carrier concentration we shall need to calculate the volume of the region to which the carriers are confined. We find that there are two separate regimes that need to be considered, which are depicted in Figure 5.2. For large diameter wires the free holes are confined to an annular region close to the core/shell interface by the electrostatic attraction of the electrons trapped in the shell. This regime will be discussed in Section 5.2.1. For smaller diameter wires there is no longer any region within the wire that is devoid of free carriers. This second regime will be discussed in Section 5.2.2.

5.2.1 Regime 1: $R \gg d$

The free holes in the germanium core will be attracted to the electrons trapped in the shell and consequently exist predominantly in a region near the interface for large diameter wires [2, 3], as depicted in Figure 5.2 (a). This region is called the space charge region [2, 3] and the depth to which it extends into the sample is found by solving Poisson's equation [3]. The calculation of this depth simplified by assuming that the space charge region has a constant charge density n_{sc} and extends some distance d from the surface [3]. Under these assumption it can be shown that for a cylindrical geometry [4]:

[1] $\rho = 1/ne\mu$, where we drop the tensor notation of Section 2.1.1 for simplicity.

$$-\frac{2\pi\epsilon_r\epsilon_0\phi_0}{en_{sc}} = R^2\left(1-\frac{d}{R}\right)^2 \times \left(1-2\ln\left(1-\frac{d}{R}\right)\right) - R^2, \qquad \text{Eq. 5.2}$$

where ϕ_0 is the electrostatic potential at the surface, ϵ_0 is the dielectric constant of free space, ϵ_r is the relative permittivity of germanium, and e is the charge of the electron. Equivalently we may say that the space charge region results from the bending of the bands near to the surface [3]. The bending is caused by the charge trapped in the surface states, as we discussed in Section 2.4.2, when we described the formation of Schottky barriers in the presence of surface states. The electrostatic potential at the surface in Eq. 5.2 is equivalent to the band bending discussed there. The carrier concentration will fall off gradually away from the surface, and there will not be a sharp distinction between the occupied space charge region and the empty centre of the nanowire. For this reason Eq. 5.2 is only valid when $R \gg d$. In Section 5.2.1 we shall see that $R \approx d$ for a nanowire diameter of approximately 20 nm. This is the primary theoretical reason for dividing our wires into two regimes above and below this diameter as mentioned in the introduction. The value of d varies as the diameter of the nanowire is changed, but is close to 8 nm over the entire range.

We now turn to calculating the carrier concentration when $R \gg d$ under the aforementioned discussions. The volume of the space charge region is the volume of the whole wire minus the inner cylindrical region with no charge:

$$V_{sc} = \pi R^2 l - \pi(R-d)^2 l. \qquad \text{Eq. 5.3}$$

To find the carrier concentration we divide the number of free holes in the wire, Eq. 5.1 by the volume of the space charge region. After expanding the second term in Eq. 5.3 we find the carrier concentration in the space charge region to be:

$$n_{sc} = \frac{N_{ss}}{V_{sc}} = \frac{2n_{ss}R}{2Rd - d^2}, \quad \text{Eq. 5.4}$$

where we have again assumed that there is a constant carrier concentration over some distance d, leading to the same restrictions of usage as for Eq. 5.2. Finally, by multiplying by the charge of the electron and the mobility, μ, we can find the dependence of the resistivity, ρ, on the diameter, using Eq 2.5:

$$\rho = \frac{1}{n_{sc}e\mu} = \frac{2Rd - d^2}{2n_{ss}Re\mu}. \quad \text{Eq. 5.5}$$

5.2.2 Regime 2: $R < d$

When $R \leq d$ we must now replace the volume of the space charge region in Eq. 5.3 with the volume of the core of the wire, V, as there is now no region in the nanowire that is devoid of mobile holes, as indicated in Figure 5.2 (b). This gives:

$$n = \frac{N_{ss}}{V} = \frac{2\pi Rln_{SS}}{\pi R^2 l} = \frac{2n_{SS}}{R}, \quad \text{Eq. 5.6}$$

$$\rho = \frac{R}{2n_{ss}e\mu}. \quad \text{Eq. 5.7}$$

We note if we set $R = d$ in Eq. 5.4 and Eq. 5.5 we recover Eq. 5.6 and Eq. 5.7, showing that the equations are consistent.

As will be discussed in detail in Section 5.3.1 we modelled each nanowire in regime 2 as an infinite cylindrical well. The density of charge carriers is then given by the square of the wavefunction, which is not constant across the cross sectional area of the nanowire. By using an infinite potential well we also neglect the effect of the electrons trapped in the interface states.

The use of an infinite potential well is the most important simplification that we make. A more accurate calculation would solve the Schrödinger and Poisson equations

self consistently [5-7]. To better understand what difference this will make to the charge distribution and thus to the final result of our mobility calculation let us briefly examine the results of this self-consistent calculation which have been reported by other groups [7, 8]. We note firstly that all previous work has been done for silicon nanowires, not germanium, so that we do not expect previous calculations to be quantitatively accurate for our wires. It has been found that for comparably larger diameter wires (15 nm in [7] and 8 nm in [8]) the carriers are located predominantly close to the edges of the nanowire. As the nanowire diameter is decreased the carriers move away from the edges and the highest density of carriers is found near to the centre of the wire. This is shown at 3 nm in [7] and approximately 6 nm in [8]. This effect is termed volume inversion in [8].

The charge distribution that was reported in these studies for large diameter wires agrees well with the charge distribution that we introduced in Section 5.2. We should note that the calculations in [7] and [8] were carried out with an applied gate voltage, using a gate-all-around geometry. This gate voltage has the same effect as our surface states in attracting the mobile carriers to the surface of the wire, and it is therefore not surprising that the results are qualitatively similar. By neglecting this charge distribution in wires with diameters below 20 nm we expect that we shall underestimate the Coulomb scattering from charges trapped at the interface, and therefore overestimate the associated mobility. We will discuss this in more detail in Section 5.3.4. Our analytical method is computationally simpler, but we shall see a good qualitative agreement with experiment nevertheless. The quantitative differences between the experimental and theoretical results all stem from the effects described

here. We will discuss this in more detail when we show the results for Regime 2 in Section 5.4.2.

It is important to note that the volume inversion that we discuss here is different from the change from regime 1 to regime 2. The characteristic change that occurs during the volume inversion is that the density of carriers is higher at the edges of the wire before volume inversion and is higher at the centre of the wire after volume inversion. In contrast the difference between regime 1 and 2 is the existence of a region devoid of carriers in regime 1 which is not present in regime 2. The carrier distribution may be similar in both regimes, particularly near to the transition at approximately 20 nm. It is not clear if volume inversion should occur in our wires given that the minimum diameter that we measure is 11 $\pm$ 1 nm. We note it here for completeness as it will have an effect on the results of the calculation for the smallest wires if it does occur at these diameters in germanium wires. In order to make the calculation of the mobility in regime 2 easier we neglected the effect of the trapped electrons on the hole distribution.

5.3 Mobility Calculation in Regime 2 ($R < d$)

We now discuss the calculation of the mobility in Regime 2 using the one-dimensional Kubo-Greenwood formula, Eq 2.48 [9, 10]. We shall first describe the wavefunction that we used in the calculation in Section 5.3.1 and then the calculation to find the Fermi level in Section 5.3.2. Phonon scattering, Coulomb scattering and surface roughness scattering will be the focus of Sections 5.3.3, 5.3.4 and 5.3.5, respectively. We give justification for the use of the one-dimensional formula for wires with diameters below 20 nm in Section 5.3.6 by examining the average subband spacing as a function of

nanowire diameter. This section also contains Table 5.1 which gives values for the various constants that we used, describes how the integration was carried out and discusses the relative importance of heavy and light holes in our system. Finally Section 5.3.7 contains a discussion of the important diameter dependent terms that arise in the calculation. We shall see that the mobility will decrease due to the increased probability of scattering between states, in spite of the fact that the number of available states to scatter into is reduced.

5.3.1 Wavefuction of the Charge Carriers

To calculate the mobility with the Kubo-Greenwood formula we first need to calculate the momentum relaxation times for different scattering processes. For these calculations we will require the wavefunction of the carriers in the wire. As mentioned in Section 5.2.2 we modelled the nanowire as an infinite cylindrical well, assuming that the mobile holes would be present throughout the entire volume of the wire. From the discussion in the previous section this limits the validity of this calculation to the wires in Region 2. The advantage of this approach is that it allows us to solve for the wavefunction analytically. In cylindrical coordinates ($\boldsymbol{r} = (r, \theta, z)$) the wavefuction, $\Psi(\boldsymbol{r})$ can be decomposed into its radial, $R(r)$, angular, $\Theta(\theta)$, and longitudinal, $Z(z)$, parts [11]:

$$\Psi(\boldsymbol{r}) = R(r)\Theta(\theta)Z(z). \qquad \text{Eq. 5.8}$$

For our calculations we shall only require the radial part due to cylindrical symmetry of the system. This is discussed in more detail in Appendix C. The radial part of the wavefunction is given by [11]:

$$R_{mn}(r) = R_i(r) = \frac{\sqrt{2}}{RJ_{m+1}(j_{mn})} J_m\left(\frac{j_{mn}}{R} r\right), \quad \text{Eq. 5.9}$$

where $m = 0, \pm 1, \pm 2 \ldots$, $n = 1,2,3 \ldots$, $J_m$is the mth Bessel function of the first kind and j_{mn} is the nth positive zero of the mth Bessel function. Each possible pair of values for m and n corresponds to a different subband. We shall label each subband with a single index, i, instead of with m and n for clarity in later equations. The derivation of $R_i(r)$ is given in Appendix C.

The assumption of an infinite potential well leads to parabolic bands. In Section 2.2.4 we discussed the fact that in low dimensional structures the bands are no longer well described as parabolic and introduced the nonparabolic correction term, α, to account for that fact. We then gave equations for the wavevector, group velocity and density of states, Eqs 2.29, 2.30 and 2.31 respectively in Section 2.2.5, taking into account the nonparabolicity of the bands. In these equations we also introduced the term U_i which is the expectation value of the potential energy for a given subband [5, 12], $U_i = \int \Psi_i^*(\boldsymbol{r}) U \Psi_i(\boldsymbol{r})$. Due to the fact that we are setting the potential inside the wire to be 0 at all points the term U_i vanishes everywhere, simplifying the equations for use in the calculation. We took the value of α to be 0.7 eV^{-1} for heavy holes and 0.2 eV^{-1} for light holes, as has previously been calculated for germanium nanowires [13].

5.3.2 Fermi Level Position

The number of charge carriers in a nanowire can be calculated by integrating the density of states, $g(E)$, over energy up to the Fermi level, E_f:

$$n = \int_{-\infty}^{E_f} g(E) dE. \quad \text{Eq. 5.10}$$

This expression is only strictly valid at 0 K, but can be used if the Fermi level does not change by a significant amount as the sample is heated to room temperature, which should be the case for our quasi metallic nanowires [14]. Putting Eq. 5.6 for n and Eq. 2.31 for $g(E)$ into Eq. 5.10 allows us to find the Fermi level as a function of diameter and the density of surface states.

5.3.3 Hole-Phonon Scattering

Charge carriers can be scattered by either acoustic or optical phonons. Acoustic phonons have little or no momentum at the Brillouin zone centre, in contrast to optical phonons [14]. The momentum relaxation time for a hole in the subband i due to scattering from an acoustic phonon is given by [7]:

$$\frac{1}{\tau_i^{(AC)}} = \frac{\pi E_1^2 k_B T}{\hbar \rho_{Ge} u^2} \sum_{i'} g_{i'}(E) F_{ii'}, \qquad \text{Eq. 5.11}$$

where E_1 is the average deformation potential which we further describe further below, ρ_{Ge} is the density of germanium, u is the speed of sound in germanium, $g_{i'}(E)$ is the density of states in the sub-band i', and $F_{ii'}$ is the so called form factor [2] for a one dimensional wire, given by [7]:

$$F_{ii'} = \frac{1}{2\pi} \int_0^\infty dr r R_i^2(r) R_{i'}^2(r). \qquad \text{Eq. 5.12}$$

The momentum relaxation time associated with scattering from optical phonons is given by [7]:

[2] The form factor is sometimes called the overlap integral or the hole-phonon overlap integral. We do not use the term overlap integral to avoid confusion between this term and the more familiar overlap integral, $\int \Psi_A^* \Psi_B dV$. Furthermore the latter name implies that the integral contains the phonon wavefunction. In fact Eq. 5.12 contains only the charge-carrier's wavefunction and so we avoid the term hole-phonon overlap integral.

$$\frac{1}{\tau_i^{(op)}(E)} = \frac{\pi(DK)^2}{2\rho_{Ge}\omega_{op}} \sum_{i'} g_{i'}\left(E \pm \hbar\omega_{op}\right) \times \frac{F_{ii'}\left(1 - f\left(E \pm \hbar\omega_{op}\right)\right)}{1 - f(E)} \left(N_{op} + \frac{1}{2} \mp \frac{1}{2}\right), \quad \text{Eq. 5.13}$$

where DK is the average deformation potential, $\hbar\omega_{op}$ is the energy of an optical phonon, $f(E)$ is the Fermi-Dirac distribution, N_{op} is the phonon number, determined by $\left(exp\left(\frac{k_B T}{\hbar\omega_{op}}\right) - 1\right)^{-1}$ [15], and the $\pm$ signs account for forward and backward scattering, both of which are included in the calculation. The derivation of Eq. 5.11 to Eq. 5.13 is given in Appendix D. We use the angular frequency of bulk phonons in our model which has been found to be a good approximation for germanium nanowires with diameters above 10 nm [11].

Finally we come back to the effective deformation potentials, E_1 in Eq. 5.11 and DK in Eq. 5.13. E_1 describes the local energy shift of the valence band that is caused by the presence of a phonon distorting the crystal structure [16, 17]. The deformation potential is in fact a second rank tensor quantity [16, 17], related to the strain tensor. For the valence band there are three deformation potentials [18], related to the fact that the valence band is derived from a *p*-orbital as described in Section 2.2.3: One deformation potential relates to isotropic deformations, one to deformations along the [100] direction and one to deformations along the [111] direction. Despite this complexity it has been found that a single, scalar, effective deformation potential can be used which results in an error of less than 5% in the final result [19, 20]. Similarly the effective deformation potential DK should be a vector quantity that is related to the displacement of the atoms by the phonon [16, 17]. This too is approximated by an effective scalar which has been shown to introduce a negligible error [19, 20].

5.3.4 Coulomb Scattering

The momentum relaxation time for a carrier in a subband i to scatter due to a Coulomb scattering centre located at r' is given by the following set of equations [21]:

$$\frac{1}{\tau_i^{(C)}} = \frac{\pi L}{2 g_v \hbar} \sum_{i'} (g_{i'}(E) \pm g_i(E)) I_{q;ii'}^{(C)}$$

$$I_{q;ii'}^{(C)} = 2\pi L \int_0^\infty dr' r' n_C(r') \left| V_{q,ii'}^{(C)}(r') \right|^2 \qquad \text{Eq. 5.14}$$

$$V_{q;ii'}^{(C)}(r') = \frac{Ze^2}{2\pi L \epsilon} \int_0^\infty dr r R_{i'}(r) R_i(r) G_{mq}(r, r')$$

where $q = k_i \pm k_{i'}$ is the change of the hole wavevector upon scattering (*i.e.* the momentum transfer), L is the channel length of the device, $n_C(r)$ is the density of Coulomb centres at the position r, Ze is the charge located at that position, $\epsilon = \epsilon_r \epsilon_0$ is the dielectric constant of the material and the $\pm$ sign refers to forward and backward scattering. $G_{mq}(r, r')$ is a Green's function. These equations can be used for scattering from Coulomb centres located anywhere in the channel or in the dielectric material around the channel. The form of the Green's function changes depending on the relative position of the scattering centre and the charge carrier. In our calculation we assume that all the traps are located at the core/shell interface, by setting $n_C(r) = n_{ss}\delta(r - R)$, where $\delta(r - R)$ is the delta distribution, and we assumed that all of the holes were located in the germanium core. In this case the Green's function is given by the following set of equations [5]:

$$G_{mq} = a_G I_m(qr)$$

$$a_G = b_G + \frac{c_G K_R}{I_0}$$

$$b_G = -\frac{f_G K_0}{I_0} - \frac{\epsilon_{Ge}}{\epsilon_{shell}} K_{r'} \qquad \text{Eq. 5.15}$$

$$f_G = c_G - \frac{\epsilon_{Ge}}{\epsilon_{Shell}} I_{r'}$$

$$c_G = \frac{\epsilon_{Ge}(\epsilon_{Ge} - \epsilon_{Shell}) x_R I_R I'_R (I_R K_0 - K_{r'} I_0)}{\epsilon_{Shell}(\epsilon_{Ge} - \epsilon_{Shell}) x_R I'_R (I_R K_0 - K_{R'} I_0) - \epsilon^2_{Shell} I_0}$$

where $K_R = K_m(x_R)$, $K_{r'} = K_m(qr')$, $I_{r'} = I_m(qr')$, $I_R = I_m(x_R)$, $I_0 = I_m(q(R + t_{shell}))$, $K_0 = K_m(q(R + t_{shell}))$, $I'_R = dI_R/d(qr)$, $I_m(qr)$ and $K_m(qr)$ are modified Bessel functions of the first and second kind, respectively, $x_R = qR$, ϵ_{Ge} is the dielectric constant of germanium and t_{shell} is the thickness of the oxide. We note that if $t_{shell} \to 0$ then the Green's function is zero at all points[3]. We therefore must include the shell in the calculations.

Eq. 5.15 show that the Green's function is modified by the thickness and dielectric constant of the shell. However, in our case the dielectric constant is not known and the thickness varies along the length of the wire by approximately 10 nm, as can be seen in the SEM images of the wires, Figure 3.3. To demonstrate the fact that the value of the Green's function was not strongly affected by these choices we examined the effect of changing them to other reasonable values. As discussed in Section 3.1 there is a large amount of silicon in the shell, so we first took the value of the dielectric constant to be that of silicon, 11.9 [22]. We also took the value to be that of germanium oxide, 7.4. The value of the Green's function was approximately 10 % lower of the case of the silicon compared to germanium oxide. A change of less than 1

[3] If $t_{shell} = 0$, $I_{r'} = I_R = I_0$ and $K_{r'} = K_R = K_0$ as we take $r' = R$. This results in $c_G = b_G = a_G = 0$.

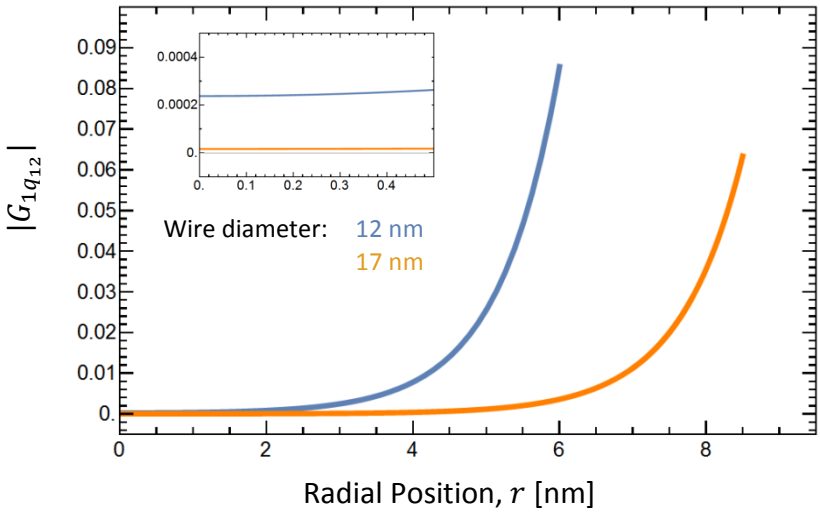

Figure 5.3 Green's function for Coulomb scattering as a function of radial position in the wire. The blue line corresponds to a wire with a diameter of 12 nm, while the orange line shows a 17 nm wire. The Greens function is larger for the smaller wire at all lengths. The insert shows a closer view of the Green's functions near to the centre of the wire. It is clear from these graphs that the scattering will depend very strongly on the distribution of the electrons within the wire. The value of the Green's function at the surface is 360 times larger than at the centre of the nanowire for the 12 wire and almost 4000 times larger for the 17 nm wire.

% was seen when we changed the thickness of the shell from 20 nm to 1 nm. We therefore conclude that our choice of parameters here does not have a large bearing on the final result. For these reasons we took the dielectric constant to be the same as for germanium oxide and assumed a constant thickness of 1 nm.

In Figure 5.3 we show the Green's function for scattering from the first ($i = 1$) to the second ($i' = 2$) subband for a nanowire with a 12 nm diameter and a wire with a 17 nm diameter wire as a function of r, the radial position of the charge carrier in the wire. The Green's function increases strongly approaching the surface of the wire, where the trapped charge is located, especially for the larger diameter wires. In this case the value of the Green's function at the surface ($r = R$) is 360 times larger than the value at the centre ($r = 0$) of the nanowire for the 12 nm wire, and 3958 times larger in the case of the 17 nm wire. For this reason the Coulomb scattering will be

strongly affected by the distribution of the carriers within the wire, especially for larger diameter wires. As discussed in Section 5.2.2 we expect that at large diameters in Regime 2 the charge carries will be located closer to the surface, and so scattering from electrons in the interface states will play a larger role. We do not take into account this carrier distribution and we are therefore likely to underestimate the Coulomb scattering especially for large diameter wires. As mentioned at the end of Section 5.2.2 this is the main source of quantitative error in the final result.

5.3.5 Surface Roughness Scattering

For wires with small diameters scattering from the structural inhomogeneity at the surface may play a significant role in limiting the mobility. However, it has been found in silicon nanowires that the surface roughness term does not become important until the wire diameter is below 10 nm [5, 6]. We should expect that this is reasonable also for germanium wires and so we do not take into account the effect of the surface roughness in our calculations.

5.3.6 Details of Calculation

In Table 5.1 we show all of the parameters that we used in the calculation. Some of these numbers have already been given, but we restate them here for ease of reference. The calculation of the mobility involves solving the Kubo-Greenwood formula [9, 10], which contains an integral over the energy from zero to infinity. In principle we should therefore include infinitely many subbands. In practise however we solve this integral numerically and include only a limited number of subbands. Only holes near to the Fermi level contribute to the mobility, as quantified by the $1/(4k_BTcosh^2((E-E_f)/2k_BT))$ term in Eq. 2.48 [5, 7]. Using the Fermi level that

Table 5.1 Constant used in calculating the mobility

Symbol	Description	Value	Unit
α	Non-parabolicy parameter	0.7 for heavy holes; 0.2 for light holes [13]	eV^{-1}
U_i	Total potential energy of the subband i	0	eV
m_{HH}^*	Effective mass of the heavy holes at $k = 0$	$0.28m_0$ [23]	kg
m_{LH}^*	Effective mass of the light holes at $k = 0$	$0.044m_0$ [23]	kg
E_1	Average acoustic deformation potential	6.49 [20]	eV
DK	Average optical deformation potential	12.17×10^8 [20]	eV/cm
$\hbar\omega_{op}$	Energy of optical phonon	37.04 [20]	eV
u	Speed of sound in germanium	5400 [20]	m/s
ρ_{Ge}	Density of germanium	5.32 [20]	g/cm^{-3}
ϵ_{Shell}	Dielectric constant of the shell	$7.4\epsilon_0$	F/m
n_{ss}	Density of surface states	10^{13}	cm^{-2}

we determine from Eq. 5.10 we find the first subband for which this term is below 10^{-3} for all energies and for every wire radius, which we refer to as the top subband. All subbands up to and including the top subband are included in the calculation. This is done for both light- and heavy-hole subbands. The number of subbands used in the calculation is diameter dependent both due to the diameter dependence of the Fermi level and the diameter dependence of the intersubband energy spacing. In Figure 5.4 (a) we plot the position of the bottom of the first 20 heavy-hole bands, in blue, and the

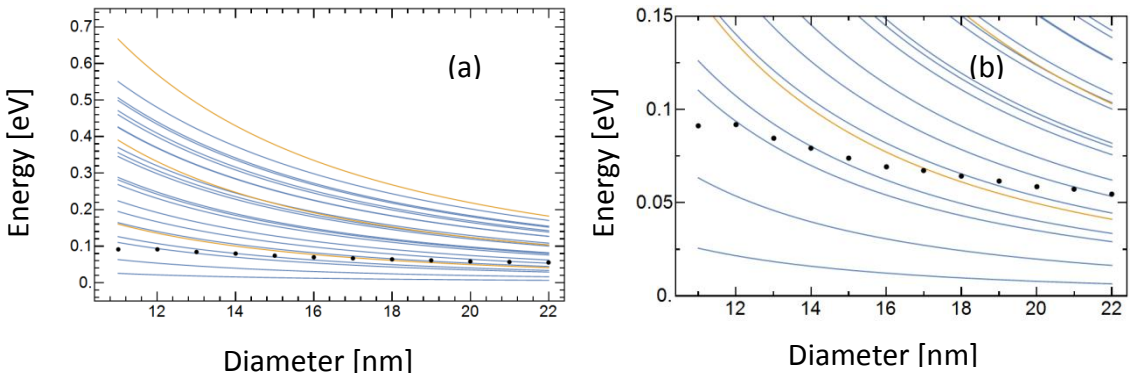

Figure 5.4 Position of subband minima and Fermi level as a function of nanowire diameter. The blue lines corresponds to heavy-hole bands, and the orange lines represent light-hole bands The black dots are the Fermi level positions for the diameters at which the calculation was carried out. (a) and (b) show the results of the same calculation, but with different energy scales. (a) shows a wider energy scale to emphasise the spreading of the subband bottoms as the nanowire diameter is decreased, and the disparity in the energy separation of the heavy-hole and light-hole subbands. It should be noted that not all of the subbands used in the calculation are shown. (b) clearly shows the position of the Fermi level relative to the subband minima.

first 3 light hole bands, in orange. It is clear to see from this image that the energy separation between the bottoms of the bands is increased as the diameter is decreased. Although we have plotted the bottom of the subband ($k = 0$) here, the same behaviour is seen for all values of k. Figure 5.4 (b) shows the same evolution of the band bottoms as Figure 5.4 (a), but with a smaller energy scale to better show the change of the Fermi level at different diameters. This will have an important bearing on the final result, which we will discuss in section 5.4.2. It should be noted that in Figure 5.4 (b) the scale on the *y*-axis is in steps of 25 meV, which is the thermal energy at room temperature, and therefore provides insight into the diameter at which single subband effects may be occurring.

The mobility of light and heavy holes, μ_{LH} and μ_{HH} respectively, will be different due to their dissimilar effective masses. We calculate the mobility of light and heavy holes separately and then combine the results as:

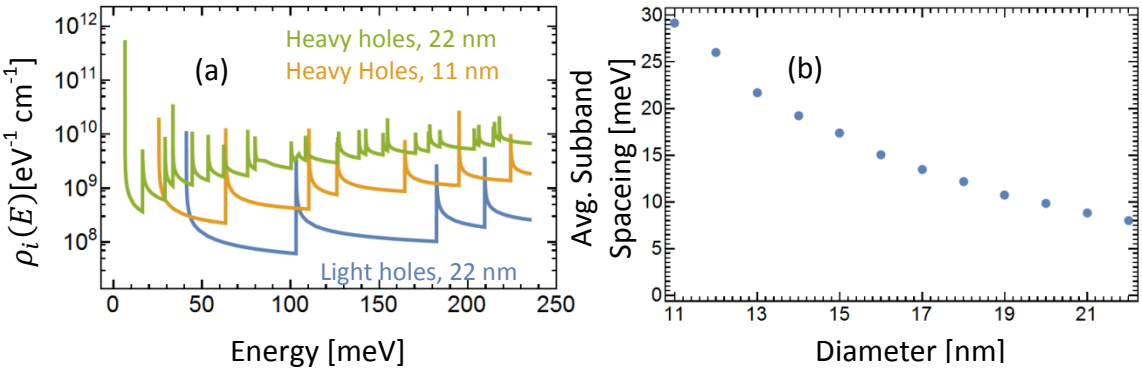

Figure 5.5 (a) modelled density of states and (b) the average subband bottom's spacing as a function of wire diameter.(a) shows the density of states for heavy holes and light holes in a 22 nm diameter wire, and the density of states for heavy holes in an 11 nm wire. The density of states for the heavy holes in the thinner wire is about an order of magnitude less than in the thick wire. This reduction in the density of states is one of the factors that leads to a diameter dependent resistivity. Similarly the density of states for light holes in a wire of the same diameter is 1.5 to 2 orders of magnitude lower than that of the heavy holes. It is for this reason that heavy holes dominate charge transport properties. Each of the spikes is caused by the singularity at the bottom of each one-dimensional subband. (b) shows the average subband bottom's spacing with all the subbands used in the calculation taken into account with equal weight. It can be seen that the average spacing is comparable to the thermal energy at room temperature, suggesting that the use of the one dimensional Kubo-Greenwood formula is justified.

$$\frac{1}{\mu_{tot}} = \frac{1}{\mu_{HH}} + \frac{1}{\mu_{LH}}. \qquad \text{Eq. 5.16}$$

Scattering into light-hole and heavy-hole bands is taken into account in both cases. In general the light holes will have a higher mobility due to their lighter effective mass, however the mobility of the material will be mainly determined by the heavy holes due to their greater density of states [13]. This can be seen in Figure 5.5 (a) where we plot the density of states for light and heavy holes in a nanowire with a 22 nm diameter. It can be seen that over the entire energy range shown here the density of states of the heavy holes is 1 to 2 orders of magnitude larger than the light hole. This is due both to the fact that the density of states in a single band is higher, as can be seen from Eqs.2.30 and 2.31, but also from the fact that at any given energy there will be more heavy-hole bands contributing to the density of states due to the smaller energy

separation between heavy-hole bands. This can be most easily seen from Figure 5.4 (a). The position of the Fermi level at each diameter is indicated by the position of the black dots, and it is clear that there are a greater number of heavy hole bands beneath the Fermi level at every diameter. It has been found that in Germanium at 220 K 96 % of the holes are heavy, with 4 % light [13] [4], and remains unaffected down to 40 K. From our plots in Figure 5.4 and Figure 5.5 (a) we expect that there should not be a substantial change at room temperature.

In Figure 5.5 (b) we plot the average subband spacing for different wire diameters. The average was found using the expression:

$$\frac{1}{\eta_{top\ subband}(R)} \sum_{i=1}^{top\ subband} E_{i+1}(R,0) - E_i(R,0), \qquad \text{Eq. 5.17}$$

where $E_i(R,0)$ is the energy of the bottom of the subband i for a wire of radius R and $\eta_{top\ subband}(R)$ is the number subbands used at that radius. It is evident that the average spacing is comparable to the thermal energy at room temperature, 25 meV. It can be seen in Figure 5.4 (b) that the subband spacing close to the Fermi level exceeds 25 meV for the smallest diameter wires that we consider. It is also clear from this plot that there are only a few subbands within a k_BT of the Fermi level at all diameters. We note that the one dimensional Kubo-Greenwood formula has previously been used when the average subband spacing was found to be 10 meV [7]. That is, the use of the one dimensional formula is reasonable, if the fact that the calculation is not valid for wires with diameters above approximately 20 nm is highlighted. This is the secondary

[4] The population of the split-off band, which is described in Section 2.2.3, was found to be negligible in the same study. In addition our Fermi level was found to be at most 92 meV, far below the split off distance of 296 meV ([20] M.V. Fischetti, S.E. Laux, Band structure, deformation potentials, and carrier mobility in strained Si, Ge, and SiGe alloys, Journal of Applied Physics, 80 (1996) 2234-2252.) For both of these reasons we do not include the split-off band in our calculations.

justification for carrying out the calculation only for wires with diameters below 20 nm in addition to the change in the distribution of the charge carriers within the wire at this diameter.

5.3.7 Origins of the Diameter Dependence of the Resistivity

The diameter dependence of the mobility is due to the density of states, the form factor and the Green's function. As the diameter of the wire decreases the density of states also decreases as we demonstrated in Figure 5.5 (a). Scattering is suppressed due to the reduction of available end-states, as can be seen from Eq. 5.11 and Eq. 5.13, leading to an increase in the mobility. This idea was first proposed by Sakaki in 1980 [24]. In Figure 5.5 (a) we have plotted the density of states for heavy holes for a wire with a diameter of 22 nm and a second wire with a diameter of 11 nm for illustration (*cf.* Section 5.3.6). The density of states for the smaller wires is found to be about one order of magnitude lower for most energies.

In the case of phonon scattering this decrease in available final states is counteracted by the form factor, (*c.f.* Section 5.3.3). The form factor increases strongly as the nanowire radius is decreased which in turn tends to decrease the mobility relaxation time. In Figure 5.6 we have plotted for illustration the form factor for a heavy hole scattering from the first to the second subband as a function of nanowire diameter from 11 nm to 22 nm. The form factor scales as R^{-2} due to the R^{-1} term in the normalisation factor of the radial part of the wavefunction, Eq. 5.9.

Similarly one finds for the case of Coulomb scattering that the Green's function increases for smaller diameter wires. This was shown in Figure 5.3. This

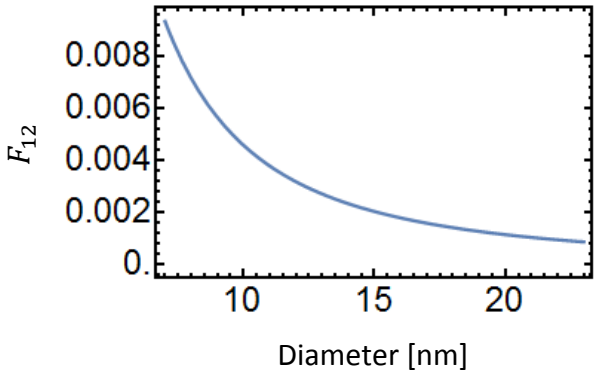

Figure 5.6 Modelled form factor for scattering from the first to the second subband. The fact that the form factor increases as the radius of the nanowire is decreased is clearly seen. This stems from the normalisation prefactor, $\sqrt{2}/RJ_{m+1}(j_{mn})$ in Eq. 5.9. This plays an important role in the diameter dependence of the resistivity, as it results in the decrease in the phonon-limited mobility as the wire radius is decreased.

counterbalances the reduction of the density of states and leads to a decrease in the mobility as the nanowire diameter is decreased.

Usually the form factor and Green's function increases are strong enough to cancel out the effect of the density of states decrease. In essence as the diameter of a wire is decreased there are fewer states to scatter into, but the probability of scattering between the states is increased, leading to an overall reduction in the mobility.

In addition to the change in the mobility the diameter dependence of the resistivity is also strongly influenced by the increase of the carrier concentration as the nanowire diameter is decreased. This can be seen from Eq. 5.6 and is the result of the difference in the scaling of the surface area and the volume of a cylinder. This has an important impact on the final results we will see in the next section and has not been included in any calculations reported previously.

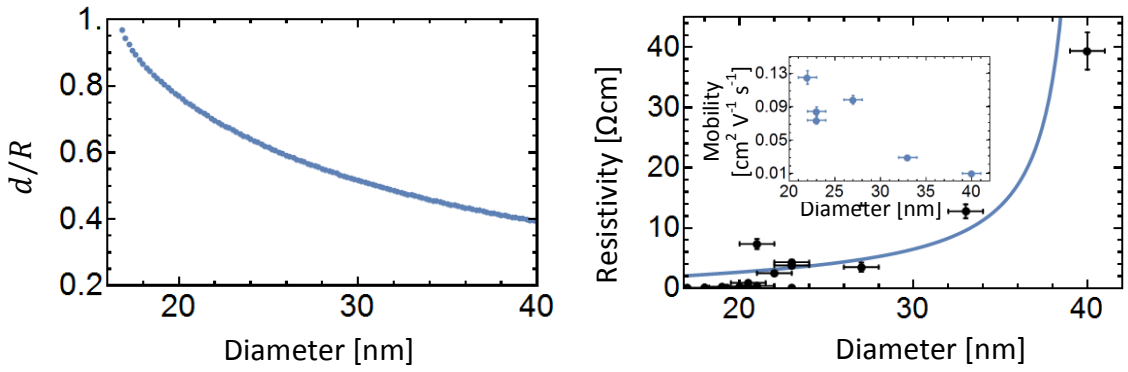

Figure 5.7 (a) ratio of space charge region width d to nanowire radius R as a function of diameter (b) comparison between theory and experiment above 20 nm. In (a) the density of surface states is assumed to be 10^{13} cm^{-2}. (a) shows that the mobile holes are distributed in an annular region near to the edge of the nanowire for nanowires with diameters above ≈ 18 nm. We therefore attempt to fit the experimentally observed resistivity values above 20 nm with Eq. 5.5. The blue line in (b) represents the fit, while the black dots are the experimental data, which are the same as that shown in Figure 5.1. The inset shows the calculated mobility values.

5.4 Comparison of Theory and Experiment

We shall now compare the results of the theory established in Sections 5.2 and 5.3 with the experimental results presented in Section 5.1. We shall look at the two regimes separately, beginning with Regime 1 ($R \gg d$) in Section 5.4.1. Here we shall use the equations from Section 5.2.1. We then turn our attention to Regime 2 ($R < d$) in Section 5.4.2, using the theoretical descriptions within Sections 5.2.2 and 5.3.

5.4.1 Resistivity in Regime 1 ($R \gg d$)

Putting Eq. 5.4 into Eq. 5.2 we can find the width of the space charge region d for a given nanowire diameter R, electrostatic surface-potential ϕ_0 and ϵ_r. We assume that the relative permittivity is the same as in bulk, 16 for the case of germanium [22]. ϕ_0 has been found to be 0.3 eV for *p*-type germanium nanowires with a native oxide [4]. Using these figures we can therefore find how the depth of the space charge region changes with diameter. In Figure 5.7 (a) we plot the ratio of d to R as a function of

nanowire diameter. We have assumed that $n_{ss} = 10^{13}$ cm^{-2}, consistent with our results from Chapter 4. We recall here that Eq. 5.2 and Eq. 5.3 to Eq. 5.5 are only valid when $R \gg d$, as discussed in Section 5.2. The experimental data suggests that this change should occur at approximately 20 nm, and that is backed up by the theory, as we see that the ratio of $d/R \approx 0.8$ at this diameter. This marks the boundary between the two regions that we have been discussing throughout this chapter. We note also that $R = d$ for a wire with a diameter of ≈ 18 nm. Below this diameter we are therefore in a region where the mobile holes are expected to be distributed throughout the entire wire.

In Regime 1 we can use Eq. 5.5 and the experimental data to calculate the mobility of the wires for different diameters. The mobility that we find is shown in the inset of Figure 5.7 (b). The mobility that we find here is in good quantitative agreement with that found in Chapter 4 from field effect measurements. As a first approximation we fit this data with a linear function and put this result back into Eq. 5.5 which allows us to plot the resistivity as a function of diameter. The result is shown as the blue line in Figure 5.7 (b) with the experimental data, the same as is shown in Figure 5.1. A good agreement with experiment is seen for wires with diameters greater than 22 nm.

5.4.2 Resistivity in Regime 2 ($R < d$)

In Figure 5.8 (a) we plot the results of the Kubo-Greenwood formula for the resistivity of wires with diameters below 22 nm. We see good qualitative agreement is seen with the experimental data shown in Figure 5.1 (b). Specifically a peak-like feature in resistivity at around 14 nm diameter is found. In Figure 5.8 (b) we plot the mobility that we calculate. We see that the mobility decreases monotonically over the entire range of diameters modelled. There is however a small plateau in the mobility between 12

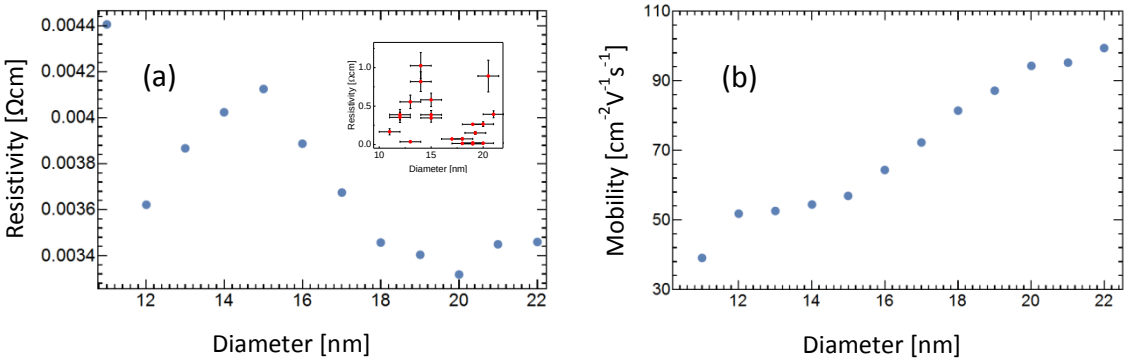

Figure 5.8 (a) Resistivity and (b) mobility calculated from the Kubo-Greenwood formula for wires with diameters from 11 nm to 22 nm. The resistivity varies by about 20 % in this range. Peaks and troughs are visible in the results, in striking similarity to the experimental results. These stem from the interplay of Fermi-level position and carrier concentration. The inset shows the experimental data for the same diameter range. The calculated resistivity values are lower than experimentally observed due to the underestimation of the scattering due to Coulomb scatterers at the nanowire surface.

nm and 15 nm. This is related to the fact that the Fermi level in this region rises rapidly as it is pinned by the large density of states at the bottom of the third and fourth subbands as can be seen in Figure 5.4 (b).

This plateau is responsible for the peak-like feature in the resistivity observed at close to 14 nm in Figure 5.8 (a). As we discussed in Section 5.3.7 the carrier concentration increases as the diameter of the wire is reduced, and is therefore acting to lower the resistivity, in opposition to the decreasing mobility. In the region where the mobility is almost constant, the increasing carrier concentration is the dominating effect and the resistivity decreases as the diameter is lowered. In all other regions the mobility decrease is strong enough to cancel out the change in carrier concentration and the resistivity increases with decreasing diameter. It is this switch between a region of mobility-dominated resistivity increase and carrier-concentration-dominated resistivity decrease leads to the peak in the resistivity that we observe at 14 nm. We note that there are two vital components here – the increasing carrier concentration

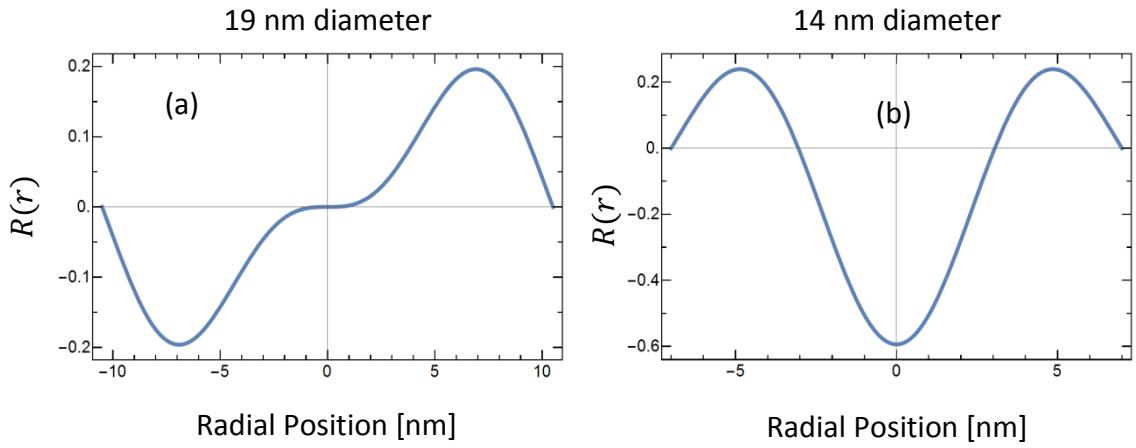

Figure 5.9 Radial part of the wavefunction for the 4th and 5th subbands. (a) shows the 5th subband, which is closest of the Fermi level for a 19 nm diameter wire as can be seen from Figure 5.4 (b), while (b) shows the 4th subband, which is close to the Fermi level for the 14 nm diameter wire. The wavefunction is large at the centre of the 14 nm wire, leading to a decrease in the calculated Coulomb scattering in this case in comparison to the 19 nm wire. Solving the Schrödinger and Poisson equations self-consistantly would likely cause a large modification of the wavefunction in the latter case, resulting in a much reduced mobility for this wire.

that is a direct result of the doping from the interface states and the quantization of the subbands that results from the carrier confinement. As such this effect is only expected in thin nanowires with significant surface state doping.

We would like to note that although the peak-like feature is well qualitatively reproduced, quantitatively the results are less satisfactory. The calculated resistivity is less than the measured resistivity across the entire range: For the lowest resistivity that we measured, 0.009 ± 0.002 Ω cm at a diameter of 19 ± 1 nm the calculated value of 0.0034 Ωcm is only a factor of 3 less than the measured value. However the situation is much worse at the top of the peak-like feature, where the calculated value of 0.0042 Ωcm is almost 240 times too low. The reason for this discrepancy is attributed to the infinite potential well approximation that we used, as we intimated in Section 5.2.2. It can be seen from Figure 5.4 (b) that at 19 nm the Fermi level is close to the bottom of the fifth heavy hole subband, while it is close to the fourth heavy hole subband at 14

nm. In Figure 5.9 we plot the wavefunction for these two subbands as a function of radial position. Clearly in the 14 nm diameter case, shown in Figure 5.9 (b), there is a greater probability of finding the charge carriers close to the wire centre, compared to the 19 nm diameter case shown in Figure 5.9 (a), where the Coulomb scattering is greatly reduced, as discussed in Section 5.3.4. This is most likely the underlying cause of the volume inversion that we discussed in Section 5.2.2 [8]. In Section 5.2.2 we pointed out that the use of the infinite potential well was likely to result in an overestimation of the charge carriers located at the centre of the wire. As a result we expect a greater modification of the wavefunction for the nanowire with a 14 nm diameter. Bearing in mind the fact that the Green's function is squared in Eq. 5.14, and that the Green's function can be hundreds of times greater at the surface of the wire than in the centre as shown in Figure 5.3, a large difference in the calculated and measured resistivity for the 14 nm wire can be expected, as compared to the relatively good agreement found for the wire with a 19 nm diameter.

As we have seen the details of the theoretical results are strongly dependent on the wavefunction used in the calculation. In spite of the fact that we modelled this in the simplest possible way we see good qualitative agreement with the experimental results. We must acknowledge that the position of the peak in the calculations is closely related to the positions of the subband minima and Fermi level and therefore it may be fortuitous that it appears at the same diameter in the experimental and theoretical results. Nevertheless the calculations suggest that such peaks are possible as a result of the Fermi level crossing subband minima while the carrier concentration increases as a consequence of the difference in the scaling of the surface area and volume of the nanowire, and indeed in this case the size of the peak is underestimated. More detailed

numerical calculation involving solving the Schrödinger and Poisson equations self-consistently need to be carried out to determine the exact details of the experimentally observed features.

References

[1] A. Levitas, Electrical Properties of Germanium-Silicon Alloys, Physical Review, 99 (1955) 1810.
[2] J. Bardeen, Surface states and rectification at a metal semi-conductor contact, Physical Review, 71 (1947) 717.
[3] M. Cardona, Y.Y. Peter, Fundamentals of semiconductors, Springer, 2005.
[4] D. Wang, Y.-L. Chang, Q. Wang, J. Cao, D.B. Farmer, R.G. Gordon, H. Dai, Surface Chemistry and Electrical Properties of Germanium Nanowires, Journal of the American Chemical Society, 126 (2004) 11602-11611.
[5] S. Jin, M.V. Fischetti, T. Tang, Modeling of electron mobility in gated silicon nanowires at room temperature: Surface roughness scattering, dielectric screening, and band nonparabolicity, Journal of Applied Physics, 102 (2007) 083715-083715-083714.
[6] J. Dura, F. Triozon, S. Barraud, D. Munteanu, S. Martinie, J. Autran, Kubo-Greenwood approach for the calculation of mobility in gate-all-around nanowire metal-oxide-semiconductor field-effect transistors including screened remote Coulomb scattering—Comparison with experiment, Journal of Applied Physics, 111 (2012) 103710-103710-103719.
[7] R. Kotlyar, B. Obradovic, P. Matagne, M. Stettler, M. Giles, Assessment of room-temperature phonon-limited mobility in gated silicon nanowires, Applied Physics Letters, 84 (2004) 5270-5272.
[8] E. Ramayya, D. Vasileska, S. Goodnick, I. Knezevic, Electron transport in silicon nanowires: The role of acoustic phonon confinement and surface roughness scattering, Journal of Applied Physics, 104 (2008) 063711-063711-063712.
[9] R. Kubo, Statistical-mechanical theory of irreversible processes. I. General theory and simple applications to magnetic and conduction problems, Journal of the Physical Society of Japan, 12 (1957) 570-586.
[10] D. Greenwood, The Boltzmann equation in the theory of electrical conduction in metals, Proceedings of the Physical Society, 71 (1958) 585.
[11] J. Hattori, S. Uno, K. Nakazato, N. Mori, Scaling consideration and compact model of electron scattering enhancement due to acoustic phonon modulation in an ultrafine free-standing cylindrical semiconductor nanowire, Journal of Applied Physics, 107 (2010) 033712-033712-033717.
[12] A. Godoy, Z. Yang, U. Ravaioli, F. Gámiz, Effects of nonparabolic bands in quantum wires, Journal of applied physics, 98 (2005) 013702-013702-013705.
[13] S. Rodríguez-Bolívar, F. Gómez-Campos, F. Gámiz, J. Carceller, Implications of nonparabolicity, warping, and inelastic phonon scattering on hole transport in pure Si and Ge within the effective mass framework, Journal of applied physics, 97 (2005) 013702-013702-013710.

[14] N.W. Ashcroft, N.D. Mermin, Solid State Physics (Holt, Rinehart and Winston, New York, 1976), There is no corresponding record for this reference, (2005).
[15] D.K. Ferry, S.M. Goodnick, Transport in nanostructures, Cambridge university press, 1997.
[16] D. Ferry, Semiconductor transport, CRC Press, 2000.
[17] B.K. Ridley, Electrons and phonons in semiconductor multilayers, Cambridge University Press, 2009.
[18] G. Bir, G. Pikus, Theory of the deformation potential for semiconductors with a complex band structure, SOVIET PHYSICS-SOLID STATE, 2 (1961) 2039-2051.
[19] P. Lawætz, Low-field mobility and galvanomagnetic properties of holes in germanium with phonon scattering, Physical Review, 174 (1968) 867.
[20] M.V. Fischetti, S.E. Laux, Band structure, deformation potentials, and carrier mobility in strained Si, Ge, and SiGe alloys, Journal of Applied Physics, 80 (1996) 2234-2252.
[21] J. Lee, H.N. Spector, Impurity-limited mobility of semiconducting thin wire, Journal of applied physics, 54 (1983) 3921-3925.
[22] S.M. Sze, Physics of Semiconductor Devices, Wiley, New York, 1981.
[23] C. Jacoboni, L. Reggiani, The Monte Carlo method for the solution of charge transport in semiconductors with applications to covalent materials, Reviews of Modern Physics, 55 (1983) 645.
[24] H. Sakaki, Scattering Suppression And High-Mobility Effect Of Size-Quantized Electrons In Ultrafine Semiconductor Wire Structures, Japanese Journal of Applied Physics, 19 (1980) L735-L738.

6. Temperature Dependence of Resistance

In this chapter we discuss the temperature dependence of the resistivity of the wires. We see a large difference in the temperature response of high resistance samples which showed a gate response and the low resistance samples in which little or no gate response to the gate was observed. We therefore discuss these two cases separately. Section 6.1 deals with the samples that showed a gate response. We shall argue that the data are best fit by the theory of variable range hopping in the presence of a Coulomb gap developed by Efros and Shklovskii [1], and described in Section 2.7.3. Section 6.2 shall then present the low resistance data. Here we will see that the data are not well fit by a single model, but that the transport mechanism varies with the temperature. The quasi-metallic nature of these wires will again be evident, in agreement with the results of Chapter 4 and Chapter 5. In many of the graphs throughout this chapter we shall encounter the problem that the temperature range measured is not large enough to definitively distinguish between different transport mechanisms. This is due either to the response changing over too small a temperature range or due to the sample becoming too resistive to measure. In each case we will attempt to extract parameters from the graphs to determine which mechanism is the most physically reasonable.

6.1 High Resistance Samples with a Gate Effect

In this section we will examine high resistance samples that showed a gate response. We will first present the data taken from 4-point measurements in Section 6.1.1, and then data taken in 2-point measurements in Section 6.1.2. Although it may be expected that the contacts would play a large role in the temperature response we will argue

that this is not the case both by directly comparing 4-point and 2-point data in Section 6.1.1, and by arguing that the response seen is not commensurate with contact effects in Section 6.1.2. In both sections we will present data with and without an applied gate voltage. We will see that all of the data are well fit by assuming that the transport is due to variable range hopping, but the measureable temperature range is too small to distinguish between Mott variable range hopping and Efros-Shklovskii variable range hopping. In Section 6.1.3 we will therefore use both theories to find the density of surface states. We shall find that the density of states extracted using the Efros-Shklovskii model agrees better both with the results presented in Chapter 4 of this thesis and with previously published results.

6.1.1 4-Point Data

Figure 6.1 (a) shows the 4-point resistance of a nanowire plotted against the temperature on a semi-log scale. This wire was taken from batch 2, and we shall hereafter refer to it as sample A. This sample had a resistivity at room temperature of 30 Ωcm, well in excess of other batch 2 samples of comparable diameter, as can be seen in Figure 5.1 in Chapter 5. Data are shown from room temperature to approximately 175 K, below which the sample was too resistive to measure reliably. Both 4-point and 2-point resistance is shown in black and red respectively. It is clear that the slope of the graph is the same in both cases, indicating that the observed change in the resistance was not due to contact effects, but was instead a feature of the nanowire

In Figure 6.1 (b), (c) and (d) we plot the natural log of the 4-point resistance against T^{-1}, $T^{-1/2}$ and $T^{-1/4}$ respectively. Data with no applied gate voltage is shown

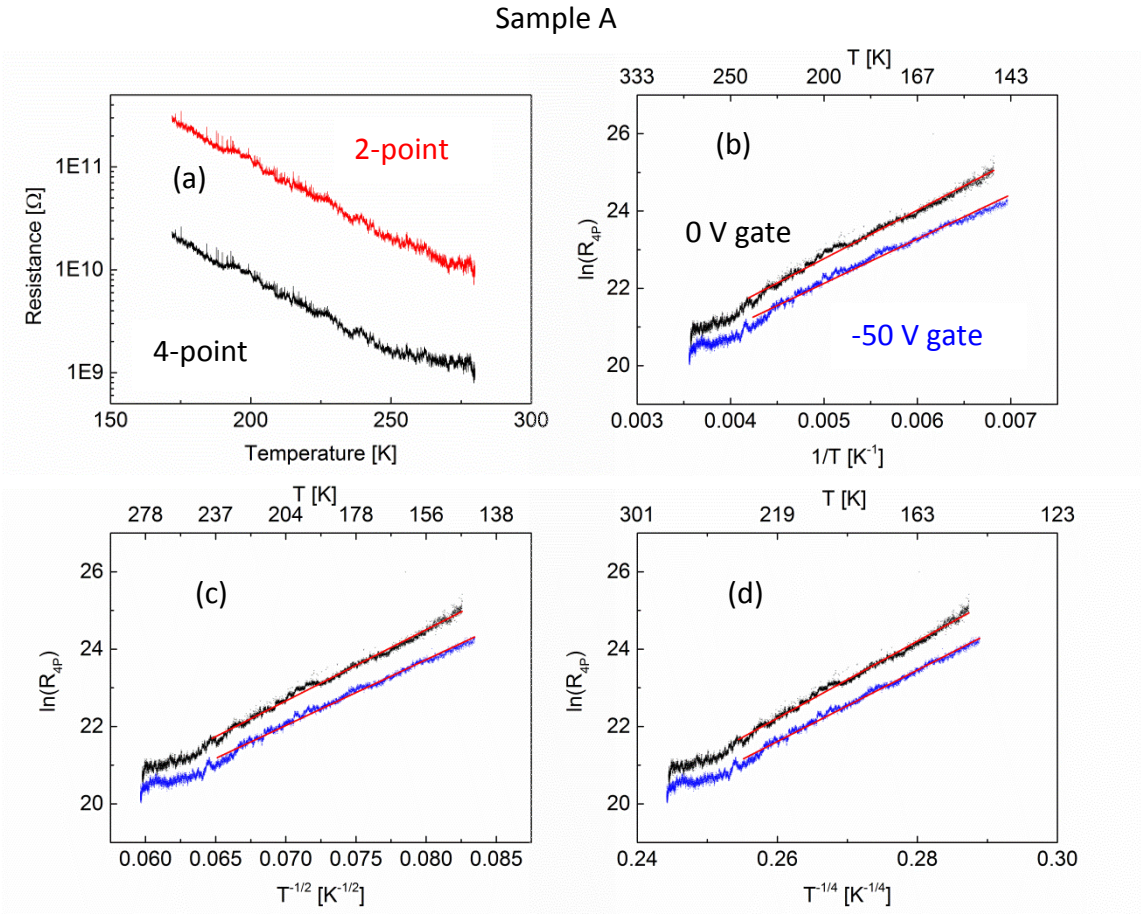

Figure 6.1 Variation of 4-point resistance with temperature for a high resistance sample with a gate effect In (a) the two point data are shown in red, while the 4-point data is in black. A lower resistance is seen for the 4-point measurement, as expected. The two sets of data have the same slope, showing that the contact resistance is a constant at all temperatures, and not the source of the resistance variation that we see. Graphs (b), (c) and (d) plot the natural log of the resistance against the inverse of the temperature in (b), against the inverse of the square root of the temperature in (c) and against the inverse of the fourth root of the temperature in (d). In each of these graphs the black points are taken with no gate voltage applied, and the blue data points were taken with -50 V applied to the back gate. A lower resistance is seen with the gate applied as expected for *p*-type samples, but the slope is not substantially altered in any case. The red line is a fit to the linear fit to the data below 250 K.

in black, while data taken with -50 V applied to the gate is shown in blue. The slopes of the graphs are not significantly altered by the applied gate voltage, though the value of the current is reduced. In Section 2.7.2 we discussed the fact that in doped or intrinsic semiconductors the resistance is expected to vary due to the freezing out of charge carriers. We would expect in this case that the resistivity follows an Arrhenius law [2]:

$$\rho(T) = \rho_0 \exp\left(\frac{E_A}{k_B T}\right), \qquad \text{Eq. 6.1}$$

where ρ_0 is a constant, E_A is the activation energy and k_B is Boltzmann's constant. In that section we also discussed the possibility of observing variable range hopping in the presence of localised states. We gave the equation for the change in resistivity with temperature, $\rho(T)$, in the variable range hopping regime to be:

$$\rho(T) = \rho_0 \exp\left(\left(\frac{T_0}{T}\right)^{-\nu}\right), \qquad \text{Eq. 6.2}$$

where ρ_0 and T_0 are constants and ν is 1/(d+1) in the case of Mott variable range hopping, where d is the dimensionality of the system and 1/2 for Efros-Shklovskii variable range hopping [1, 3]. The main difference between the two theories is that the Efros-Shklovskii theory assumed that a band gap opens in the single electron density of states [1, 3]. Eq. 6.2 is often described as a stretched exponential form. In the presence of localised states transport can also occur due to carriers being excited across the mobility edge, and the resistivity would vary according to Eq. 6.1 in this case. If activated transport holds we would expect the data shown in Figure 6.1 (b) to fall on a straight line in accordance with Eq. 6.1 while the graphs of Figure 6.1 (c) or (d) should be linear in the case of variable range hopping, following Eq. 6.2. It is clear that a reasonable fit is seen in all cases for the data from $\approx$ 250 K to 175 K, but a better fit is seen in Figure 6.1 (c) and (d) than in (b). The non-linearity of (b) is most evident in the gated data. The range of data over which this sample was measureable is too small to distinguish adequately between the Mott model of variable range hopping in 3 dimensions or 1 dimension and the Efros-Shklovskii model. In Section 6.1.3 we shall argue that the data are better fit by the latter theory based on the slopes of the graphs.

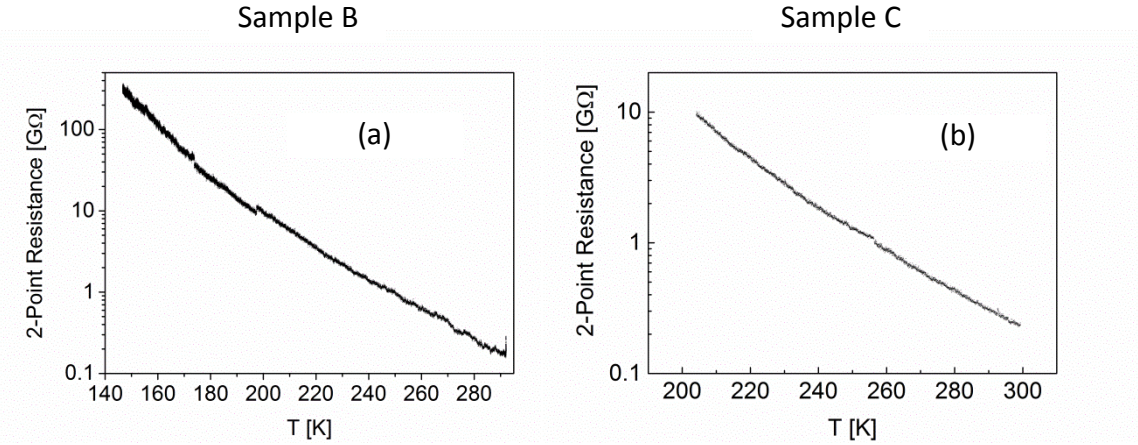

Figure 6.2 Variation of resistance with temperature for two samples from batch 1, plotted on a semi-log scale. In (a) we show data from room temperature to approximately 150 K, while in (b) data are shown from room temperature to 200 K. A three order of magnitude change is seen in (a), but only a two order of magnitude change is evident in (b). In both graphs the data are plotted as individual crosses, not as a line. No gate voltage is applied ot the sample in either case.

6.1.2 2-Point Data

In Figure 6.2 we show the variation of resistance with temperature for two different samples. Both of these samples were from batch 1, and showed a *p*-type gate effect. 2-point measurements are shown for both samples, and the data are plotted on a semi-log plot. The graph on the left, Figure 6.2 (a), is from one sample, which we shall call sample B, while the graph on the right, Figure 6.2 (b) is from a different sample, which we shall call sample C. No gate voltage is applied to the wire in either case. The data with a gate voltage applied shall be discussed at the end of this section, as a different temperature response was seen with an applied gate voltage in this case. The temperature range is from room temperature down to approximately 150 K in sample B, and from room temperature to 200 K in sample C. Below these temperatures the wires became too resistive to measure.

Figure 6.3 plots the same data as shown in Figure 6.2. Graphs (a), (b) and (c) show the sample B data, while graphs (d), (e) and (f) show the sample C data. Figure 6.3

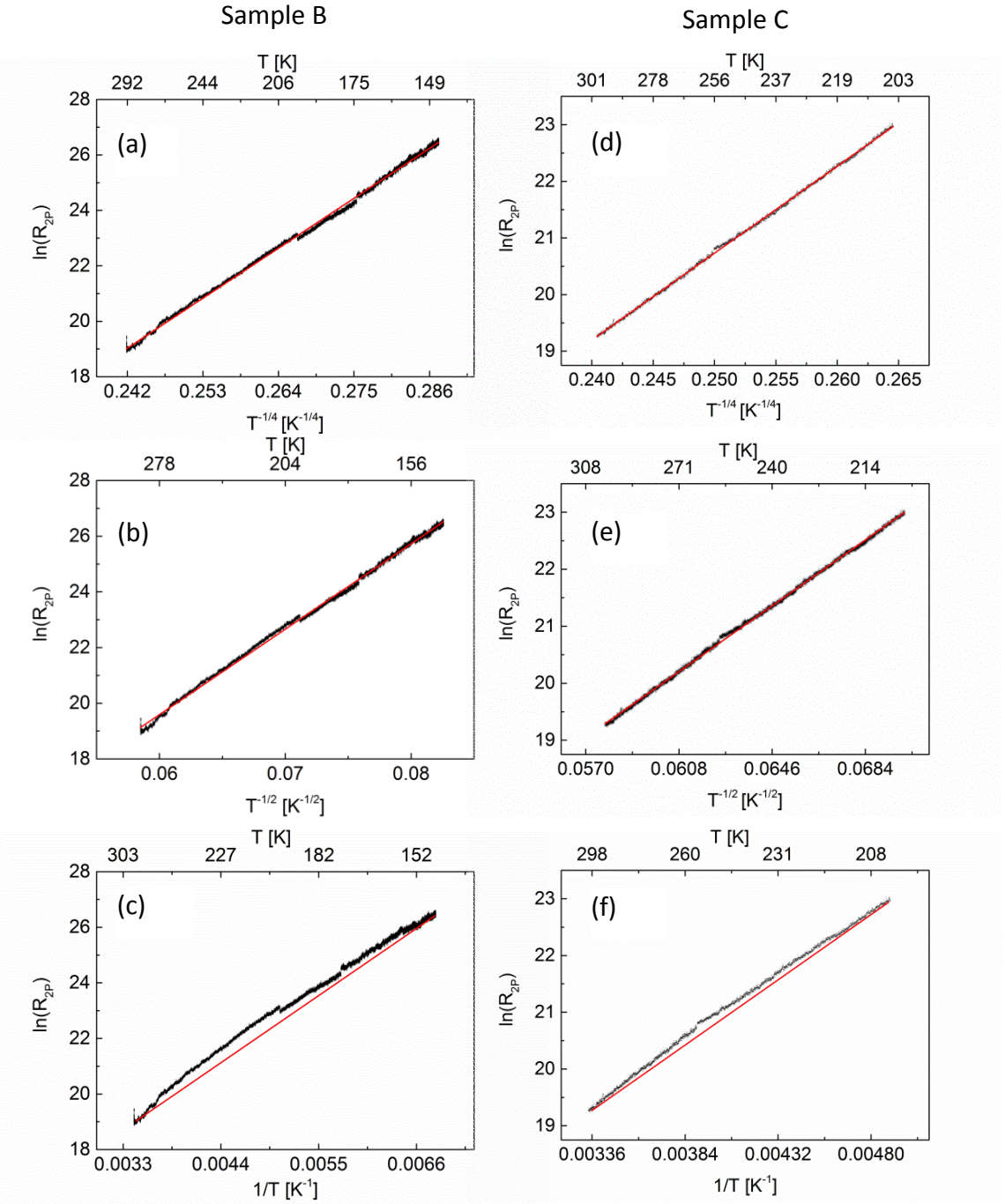

Figure 6.3 Change of resistance with temperature of samples B and C. The graphs on the left, (a), (b) and (c) are from one sample, sample B, and contain the same set of data. (d), (e) and (f) are taken from sample C. All plots show the data as individual crosses, not as a line. (a) and (d) show the natural log of the 2 point resistance is plotted against $\boldsymbol{T^{-1/4}}$, (b) and (e) show the natural log plotted against $\boldsymbol{T^{-1/2}}$. and (c) and (f) show the natural log plotted against $\boldsymbol{T^{-1}}$. The plots shown in (a) and (d) are linear in the case of Mott variable range hopping in 3 dimensions, the plots in (b) and (e) are linear in the case of Efros-Shklovskii variable range hopping or Mott variable range hopping in 1 dimension and (c) and (f) are expected to be linear in the case of activated transport or in the case that Schottky barriers play in important role in the temperature response. The red line in (a), (b), (d) and (e) are linear fits to the data, while the red lines in (c) and (f) are guides to the eye to emphasise the lack of linearity in these plots. The temperature range is not large enough to distinguish between Mott variable range hopping and Efros-Shklovskii variable range hopping.

(a) and (d) show the natural log of the 2-point resistance plotted against the inverse of the fourth root of the temperature. This is the plot suggested by the model of Mott variable range hopping in 3 dimensions[3] (Eq. 6.2 with ν=1/4). Graphs (b) an (e) plot the natural log of the 2-point resistance against the inverse of the square root of the temperature, to test for the fit to Efros-Shklovskii variable range hopping, or Mott variable range hopping in 1 dimension [1] (Eq. 6.2 with ν=1/2). For comparison Figure 6.3 (c) and (f) show the natural log of the resistance plotted against the inverse of the temperature. The data should fall on a straight line here in the case of a doped or intrinsic semiconductor [2], as discussed in Section 6.1.1.

It is clear that the data fit much better to Eq. 6.2 than to Eq. 6.1, even in this limited temperature range, though it is again not clear from the experimental data whether the Mott in 3 dimensions or 1 dimension or Efros-Shklovskii model is favoured. In Figure 6.3 (c) and (f) the red line a guide to the eye to emphasise the non-linearity of these plots, while the red line is a fit to the data in all other graphs.

As the data shown in Figure 6.2 and Figure 6.3 are taken from 2-point measurements it may be expected that the variation in the contact resistance would play a large role. In Section 2.4 we discussed the formation of Schottky barriers at metal-semiconductor interfaces, such as we have on our wires. In that Section we also gave the formulae relating the current density through the Schottky barrier to the temperature and applied voltage for the case of both a single Schottky barrier and for the case of back to back Schottky barriers. In either case an exponential dependence similar to Eq. 6.1 is expected [1]. The fact that we do not see a good fit to this indicates

[1] Eq. 2.40 also contains a term such that $j \propto T^2$, but the exponential term dominates here.

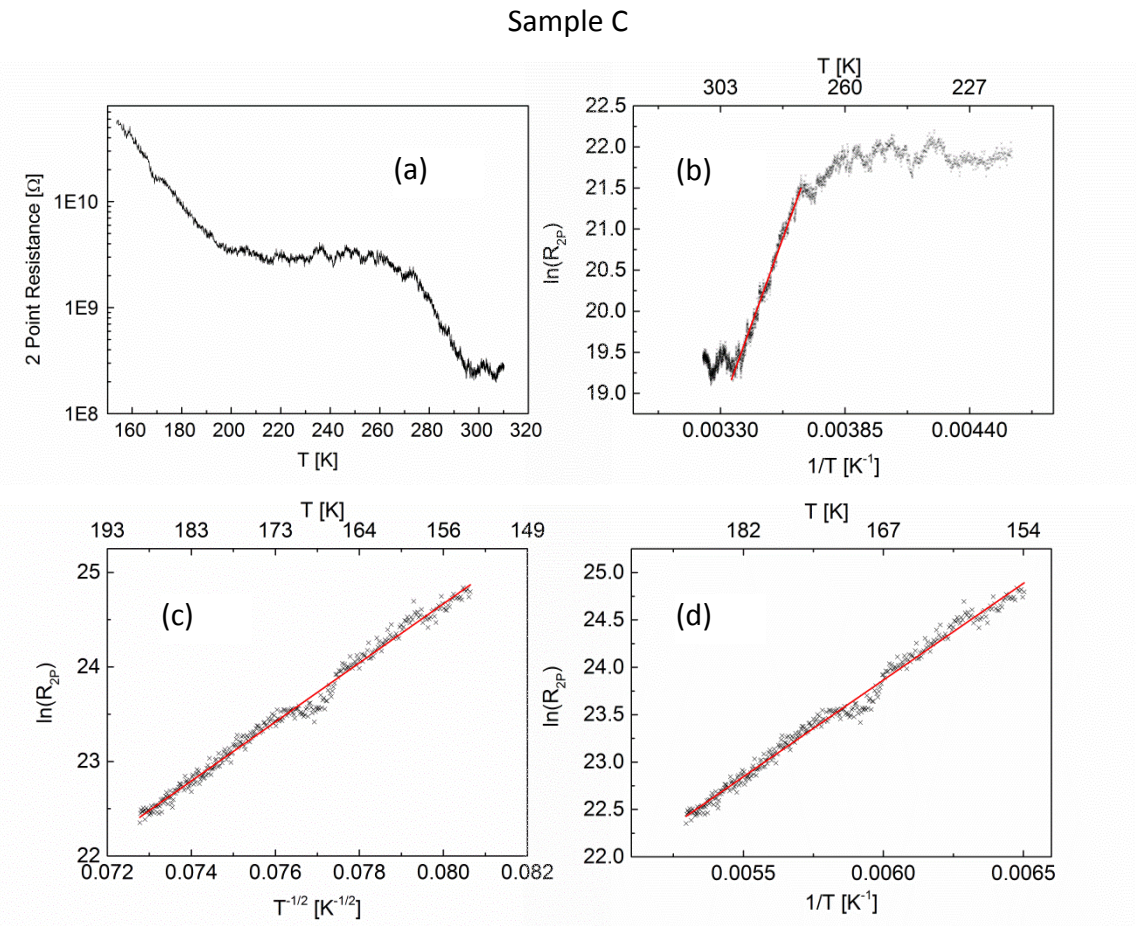

Figure 6.4 Temperature dependence of sample C with – 20 V applied to the gate. (a) shows the data on a semi-log plot. Three distinct regions are seen. (b) and (d) show the data plotted as the natural log of the resistance against the inverse of the temperature. (b) shows the range from room temperature to 220 K, while (d) shows the data from 200 K to 160 K. In both cases the red line is a fit to the Arrhenius equation, Eq. 6.1. (c) shows the same data as (d), but this time plotted against $\boldsymbol{T^{-1/2}}$. A good fit is also seen in this case. This suggests that the temperature range here is too small to distinguish well between the exponential and stretched exponential form of Eq. 6.1 and Eq. 6.2.

that Schottky barriers do not play an important role in the temperature response of these samples. Furthermore the fact that the contact resistance plays little role in the 4-point data shown in Figure 6.1 (a) supports the fact that the effects that we see here are effects of the nanowire. This also adds evidence to the memristance model that we developed in Chapter 4, where we claimed that the non-linearity of the current-voltage response was due primarily to the asymmetric hopping of electrons into and out of interface states, with Schottky barriers, if present, not playing a dominant role.

In Figure 6.4 we plot the temperature dependence of Sample C when -20 V is applied to the gate. A very different response is seen in this case, in contrast to sample A. Figure 6.4 (a) shows the resistance against temperature on a semilog scale. Three clear regimes can be made out. There is a region of increasing resistance from about 300 K to 270 K, flowed by a flat region from 270 K to approximately 200 K, and finally another region with increasing resistance from 200 K to 140 K, below which the wire was too resistive to measure. The slope in the first and final region is different. This behaviour is characteristic of a doped semiconductor [4], as described in detail in Section 2.7.2. Region one is the intrinsic region, where electrons are excited across the band gap [4]. The flat region is the saturation region [4]. In this temperature range there is not enough thermal energy to excite carriers across the gap, but still enough to ensure that all dopants are ionised [4]. As the temperature is lowered further the dopants begin to recombine leading to the third region of increasing carrier concentration [4].

As described in Section 2.7.3 in the presence of localised states transport can occur either due to a carrier hopping from state to state or by a carrier being excited to an extended state [3]. There is a critical energy, known as the mobility edge between the localised and the extended states [3]. If transport is due to the excitation of carriers across the mobility edge then the temperature dependence of the resistivity will be given by an Arrhenius equation, Eq. 6.1, where the activation energy is the energy between the mobility edge and the Fermi level [3].

In Figure 6.4 (b) we plot the high temperature regime to test its fit with the Arrhenius equation, Eq. 6.1. The red line is a fit to the data, from which we extract a

slope of 7585 K. This corresponds to an energy gap of 0.65 eV, which is in excellent agreement with the band gap of germanium [5]. This suggests that the Fermi level lies near to the valence band, as would be expected with a negative gate applied to the nanowire. In Figure 6.4 (d) we make the same fit for the low temperature region and extract an energy of 0.18 eV. Finally in Figure 6.4 (c) we plot the natural log of the resistance against $T^{-1/2}$ to test for Efros-Shklovskii variable range hopping or Mott variable range hopping in 1 dimension. We find that this also fits the data, with a slope of 312 $K^{1/2}$, which is in good agreement with the slope of 304 $K^{1/2}$ seen when no gate voltage is applied. The fact that this number agrees well with the previously obtained value for this sample strongly implies that variable range hopping is recovered at low temperatures. We note however that the temperature range in Figure 6.4 (d) is simply too small to distinguish between the two formulae and we cannot conclusively rule out the possibility that the Fermi level is located 0.18 eV above the valence band leading to the freezing out of charge carriers a low temperatures. This would imply that the band gap of the nanowire is 0.83 eV, which is in good agreement with the direct band gap of bulk germanium [6, 7].

Figure 6.5 shows the temperature data from sample B when – 20 V is applied to the gate. The same data are shown in both plots and the temperature range is from room temperature to 181 K. Figure 6.5 (a) assesses the fit to the formula for activated transport, while (b) is the plot for Efros-Shklovskii variable range hopping or the 1 dimensional Mott variable range hopping theory. It is clear that there is no saturation region in this case. In (a) there appears to be two separate slopes, both of which are fitted separately. The blue line in (a), for temperatures above 260 K yields an activation energy of 0.55 eV, in good agreement with germanium's bandgap [5]. The red lines in

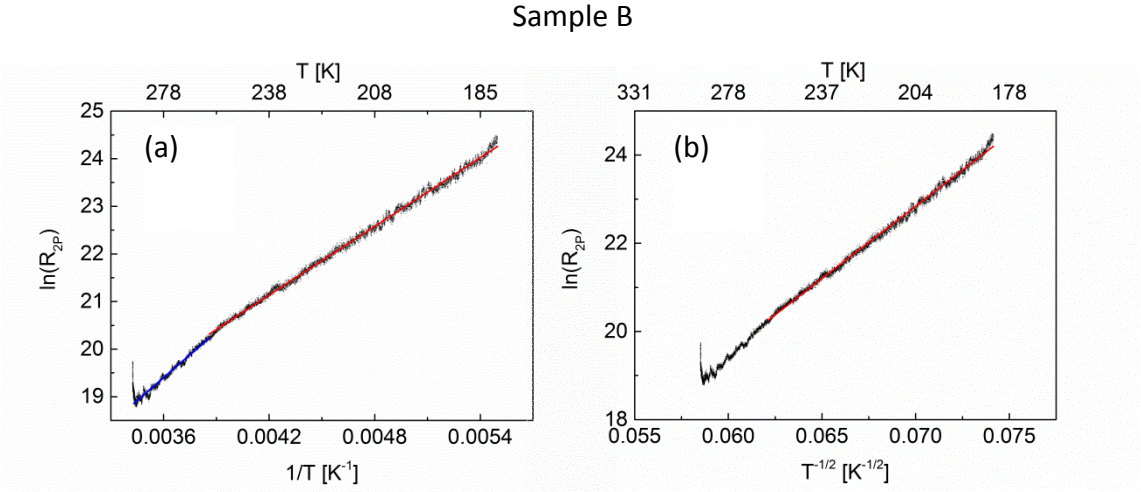

Figure 6.5 Temperature dependence of sample A with –20 V applied to the gate. (a) shows the natural log of the resistance plotted against the inverse of the temperature, while in (b) it is plotted against $\boldsymbol{T^{-1/2}}$. The blue line in (a) is a fit to the data above 260 K, while the red lines in (a) and (b) are fits to the data from 260 K to 180 K. A good fit is obtained in both graphs for the latter range.

Figure 6.5 (a) and (b) are both fits to the data from 260 K to 180 K. Both fit the data well. An activation energy of 0.41 eV is calculated from (a), while the slope of (b) is 328 $K^{1/2}$, in good agreement with the slope of 307 $K^{1/2}$ seen when no gate voltage is applied. Again the experimental data do not well distinguish between the two forms of transport, but the calculated values suggest that variable range hopping is again recovered at low temperatures, as otherwise the band gap in this sample would be 0.96 eV.

The data from Figure 6.4 and Figure 6.5 suggest that when a gate voltage is applied activated transport is recovered. The application of a negative gate brings the Fermi level close to the mobility edge and therefore activated transport is possible at a sufficiently high temperature. At low temperatures activated transport is no longer possible and hopping transport is once again recovered.

6.1.3 Mott vs. Efros-Shklovskii Variable Range Hopping

Let us first discuss the origin of the variable range hopping in these nanowires and then discuss what information can be gleaned from the graphs in order to determine which model is the most physically reasonable. In Chapter 4 we described the origin of the doping in our wires when discussing our memristance model. We said that the number of holes in the core is increased by electrons overcoming an energy barrier to enter the surface states. Simultaneously the number is decreased by electrons overcoming a different energy barrier to leave the energy state and recombine with a hole in the wire. In equilibrium these two processes will be balanced and there is a constant number of holes in the wire. The rate of both processes decreases with temperature, as described by Eq 4.1 and Eq. 4.2. Therefore if the temperature is lowered sufficiently electrons no longer enter or leave the surface states and as a result the carrier concentration in the wire remains constant. This is in stark contrast to the freezing out of charge carriers normally seen in a semiconductor which gives rise to an exponential decrease in the carrier concentration [2, 4]. Our model showed barrier heights of the order of 0.1 eV, leading to trapping times of the order of 10s of minutes at room temperature, consistent with previous observations [8, 9]. It is therefore expected that a decrease in the carrier concentration is not observed at any temperature.

The holes will not be entirely free to move throughout the wire, but will be influenced by the electrostatic attraction of the electrons trapped at the interface between the core and the shell [10]. This was discussed in Chapter 5, when we solved Poisson's equation to find that the holes existed predominantly within approximately 10 nm of the surface, see Figure 5.2. This calculation suggests that a mobile hole is able to move approximately 10 nm from the site of an electron trapped in the shell. In

Chapter 5 we assumed that the surface state density was sufficiently high that the holes were not laterally confined. That is to say that the spacing between the trapped electrons was small enough that the holes could move easily between them. This was justified (and will be further justified in Section 6.2) by the fact that the wires showed lower than bulk resistivity, suggesting that there must exist free carriers in the nanowire core. For a low density of surface states, however it would be expected that the holes will be confined not only radially, but also laterally. It is expected from the discussion in Chapter 4 that wires that show a gate effect and a high resistance should be associated with a low density of surface states, so that lateral confinement due to the trapped electrons may play a role in this case. The holes must then overcome an energy barrier to move from one electron to the next and so conduction proceeds through variable range hopping. In Section 2.7.3 we discussed the fact that variable range hopping is only possible if the electronic state of a material is on the insulating side of a metal-insulator transition [3]. This is exactly the scenario that we argued for in Chapter 4, and so the observation of variable range hopping in these samples adds further evidence to those findings.

It can be seen from Eq. 6.2 that the slope of the graphs shown in Figure 6.1 (c) and (d) and in Figure 6.3 (a), (b), (d) and (e) will be equal to T_0^{ν}. If we take the Mott model, with $\nu = 1/(d+1)$, it can be shown that this constant is related to the density of states g_d and the localisation length ξ by [3]:

$$T_0 = T_M = \frac{1.5}{k_B g_d \xi^d}, \qquad \text{Eq. 6.3}$$

where we have introduced the symbol T_M for later clarity. In contrast the characteristic temperature in the Efros-Shklovskii model is given by:

$$T_0 = T_{ES} = \frac{2.8e^2}{k_B \epsilon a}, \qquad \text{Eq. 6.4}$$

where T_{ES} has been introduced for later clarity, e is the charge of the electron, ϵ is the dielectric constant of the material and a is the distance between localised sites. From the slope of the graphs in Figure 6.1 (d) and Figure 6.3 (a) and (d), we can use Eq. 6.3 to calculate the density of states if we estimate the localisation length. From that we can obtain the density of surface states and compare it to the results obtained from transconductance measurements. The slopes of Figure 6.1 (d) and Figure 6.3 (b) and (e) can be used in conjunction with Eq. 6.4 to find the average distance between localised states directly.

Let us start with the Mott theory in 3D, *i.e*. Figure 6.1 (d), Figure 6.3 (a) and (b) and Eq. 6.3. The slopes of the graphs, 97 $K^{1/4}$, 164 $K^{1/4}$and 153 $K^{1/4}$ for samples A, B and C respectively, are equal to $T_M^{1/4}$ in this case. In order to obtain the density of states we first need to estimate the localisation length. We first remember the aforementioned solution of Poisson's equation from Chapter 5 and secondly the fact that the Bohr radius of an exciton in germanium is 24 nm [11]. While the latter should be modified by the dielectric constant of the shell it nevertheless suggests that a localisation length of the order of 10 nm is a reasonable assumption. Using this in Eq. 6.3 we calculate the density of states at the Fermi level to be 1.9×10^{14} eV^{-1} cm^{-3}, 2.4×10^{13} eV^{-1} cm^{-3} and 1.3×10^{13} eV^{-1} cm^{-3} for samples A, B and C respectively. Assuming that all of the states at the Fermi level are derived from surface states this gives a density of surface states of 3.3×10^{9} ev^{-1} cm^{-2} for sample A, 8.2×10^{8} ev^{-1} cm^{-2} for sample B and 1.0×10^{9} ev^{-1} cm^{-2} for sample C. In Chapter 4 we pointed out that the surface state density at the interface between epitaxially grown silicon and germanium was of the order of 10^{12} –

10^{14} cm^{-2} eV^{-1} [12]. We see that the results here are at least 4 orders of magnitude lower than that. If we assume that the states are spread evenly across the band gap, we find that the number of surface states per square centimetre is 2.0×10^9 cm^{-2} for sample A, 4.9×10^8 cm^{-2} for sample B and 6×10^8 cm^{-2} for sample C. In Chapter 4 we found that the number of surface states per square centimetre in our batch 1 wires was of the order of 10^{13} cm^{-2}. We therefore see that there is not a good fit to previous results if we assume that the Mott theory holds. Furthermore these results imply that the average distance between surface states is 223 nm, 450 nm and 408 nm for samples A, B, and C respectively. For variable range hopping to be possible the average distance between localised states must be less than the localisation length [3]. The results of the calculation are therefore not consistent.

Seondly let us consider Mott variable range hopping in 1D. The slope of the graphs shown in Figure 6.3 (b) and (e) are 187 $K^{1/2}$, 307 $K^{1/2}$ and 304 $K^{1/2}$ for samples A, B and C respectively, which correspond to $T_M^{1/2}$. We make the same assumptions as we did in 3 dimensions. That is to say that we assume that the hopping length is of the order of 10 nm and that the states are spread evenly across the entire bandgap of 0.6 eV. In this case we find that the density of surface states is 6.6×10^{10} cm^{-2}, 9.1×10^9 cm^{-2} and 9.4×10^9 cm^{-2} for samples A B and C respectively. Again, this is in poor agreement with the density of surface states that we previously found in these nanowires.

Let us turn now to the Efros-Shklovskii theory. The slopes of the graph are the same as those given at the start of the previous paragraph, but we now take them to be equal to $T_{ES}^{1/2}$. Taking the dielectric constant of germanium to be the same as that of

bulk, 16 [5] we find the average spacing between localised sites to be 95 nm for sample A, 2.6 nm for sample B and 2.5 nm for sample C. This corresponds to a density of surface states of 9.1×10^{13} cm $^{-2}$ for sample A, 6.6×10^{14} cm^{-2} for sample B and 6.3×10^{14} cm^{-2} for sample C. This is in much better agreement both with the results of Chapter 4 and with the density of surface states previously reported to be present on the germanium surface [8]. Furthermore for samples B and C the average spacing between localised states is less than the 10 nm localisation length that we argued for in the previous paragraph, as it must be [3]. Finally, the observation of a low density of surface states for sample A is consistent with the fact that this sample had the highest resistance, even when measured in 4-point, as can be seen in Figure 6.1 and Figure 6.2, whereas in the Mott theory this sample had the lowest density of surface states.

The above calculations suggest that the Efros-Shklovskii theory is a better fit to our data than the Mott theory. In addition, Efros-Shklovskii variable range hopping has previously been reported in bulk germanium close to the metal insulator transition [13].

6.2 Low Resistance Sample with Little or No Gate Effect

We turn now to the data from a low resistance nanowire, which we shall refer to as sample D, shown in Figure 6.6. This was the wire which showed the lowest resistivity of all the samples measured, 0.009 ± 0.002 Ωcm at room temperature. This sample was taken from batch 2, and all the data shown here is 4-point. In accordance with all the low resistivity samples no change was seen when a gate voltage was applied as discussed in Chapter 4, and so all data presented here is taken without a gate voltage. The temperature range shown in Figure 6.6 (a) is from 2 K to room-temperature. It is

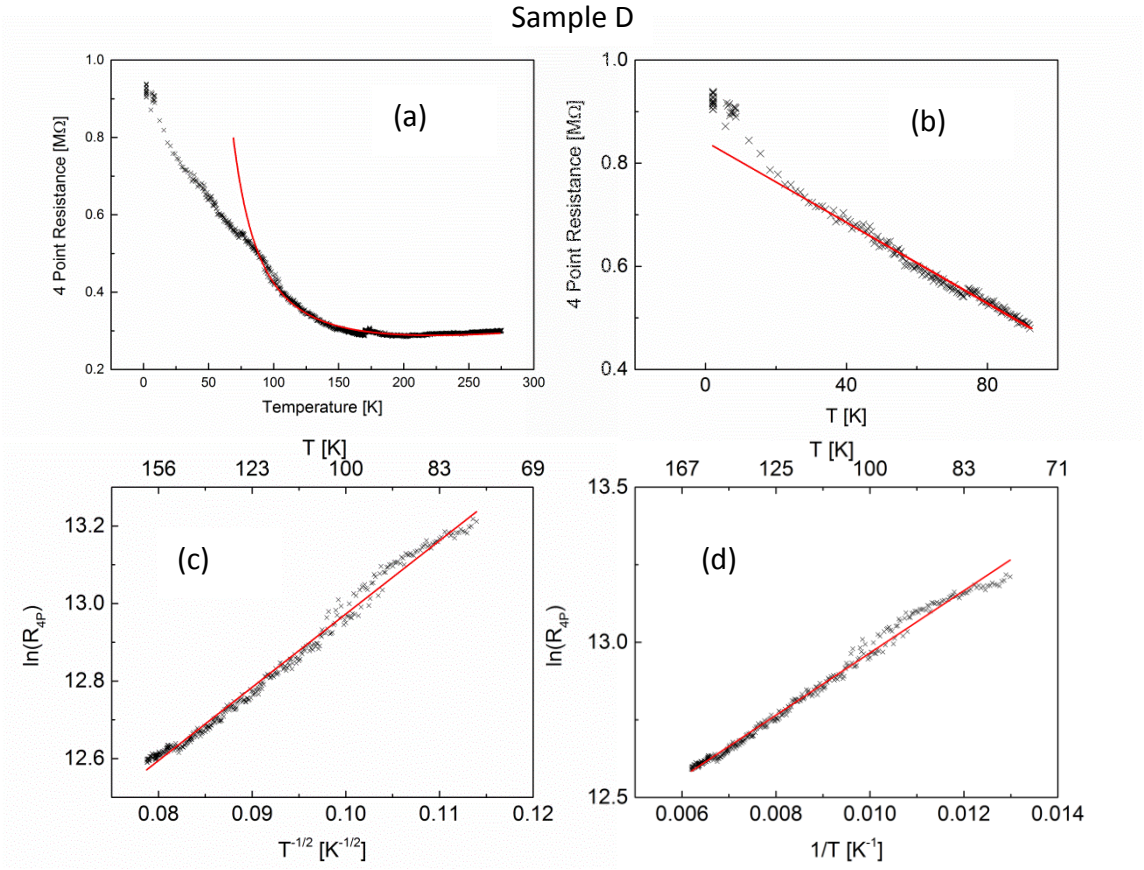

Figure 6.6 4-point resistance of a low resistance sample from batch 2 as a function of temperature. (a) shows the data on a linear scale. Note that the y-axis is linear, not logarithmic as only a factor of three change is seen in the resistance over the entire temperature range. The red line in (a) is a fit to the Blch-Grüneisen equation and the Arrhenius equation. (b) shows the data from 2 K to about 90 K, again on a linear scale. The red line is a linear for to the data above 20 K. (c) and (d) show the natural log of the resistance between the temperatures of 163 K and 80 K plotted against $\boldsymbol{T^{-1/2}}$ and $\boldsymbol{T^{-1}}$ respectively. A good fit is seen in both cases.

immediately apparent that this sample has a qualitatively different behaviour than the previous three samples that we have examined. The first important thing to note is that the resistance increases only by a factor of 3 over the entire temperature range. This is in contrast to the 2 to 3 orders of magnitude change seen in all of the other samples, in spite of the fact that the temperature range measured here is much greater than in samples A to C. The data in Figure 6.6 (a) are presented on a linear scale, not a semi-log scale as in Figure 6.1 (a) and Figure 6.2. It was found that the data cannot be fitted with a single expression, that is, the dominant mechanism controlling the temperature

response is different at different temperatures. Broadly we may divide the response into three separate regions, each of which we shall now discuss.

The first region is from 200 K to 280 K. The resistivity in this region falls with decreasing temperature. As discussed in Section 2.7.1 this is characteristic of metallic systems and results from the suppression of phonon scattering due to the reduction of the phonon population. This is a signature for the quasi-metallic nature of the wires from batch 2, which we first found from room-temperature electrical measurements in Chapter 4. This behaviour can be principally modelled using the Bloch-Grüneisen equation [14], Eq. 2.53.

The second region is from approximately 166 K down to 100 K. Figure 6.6 shows the data in this temperature range plotted as the natural log of the 4-point resistance against the inverse of the temperature in (d) and the inverse of the fourth root of the temperature in (c). The red line is a fit to the data in both instances, and a reasonable fit is obtained for both plots. The fit extends over a wider range in Figure 6.6 (c). The temperature range is not wide enough to distinguish well between the exponential and stretched exponential form. From the slope of the T^{-1} fit an activation energy of 8 meV is obtained, corresponding to a temperature of about 100 K. This is consistent with the experimental observation that the fit does not work well below 100 K, which is true as we have already said. Furthermore it has been reported that the charge neutrality level in germanium lies 9 meV above the valence band [15]. From the slope of the graph in Figure 6.6 (c) we obtain a density of surface states of 2.6×10^{11} cm^{-2}. This is 2 orders of magnitude lower than the density we found in the samples from batch 1, which is unexpected. As we shall discuss shortly at still lower temperatures the sample

continues to show quasi-metallic behaviour. As variable range hopping is an inherently insulating behaviour, its observation here would be inconsistent with the results at lower temperatures. It therefore appears that thermally activated transport provides a better physical model for the behaviour of this sample in this temperature range.

In Figure 6.6 (a) we have fitted the data with the Arrhenius type equation and the Bloch-Grüneisen equation. The main purpose of this is to show that the "missing" region between 166 K and 200 K can be understood as a transition region between the two types of transport. We see that a good fit is obtained from room temperature down to 100 K, as would be expected from our discussion. The activation energy from Figure 6.6 (d) was used. We took the Debye temperature of bulk germanium, 370 K [16] for simplicity, though it is known that this is reduced in nanostructures [17, 18]. The constants A and ρ_0 were left as fitting parameters.

If the transport remained activated or of the variable range hopping type at still lower temperatures we would expect to see a rapid increase in the resistance, until the sample was entirely insulating at 0 K [3]. Instead we see a transition to a region where the resistance rises linearly as the sample temperature is reduced from 100 K down to about 20 K. This can be seen in Figure 6.6 (b). Such dependence is consistent with transport in a disordered metal, sometimes referred to as a dirty metal [19-28]. The exact origins of this response are unclear, but it seems to be related to weak localisation [19-28]. The appearance of this behaviour suggests that the holes are still free to move throughout the wire below 100 K, albeit that they are strongly affected by the large number of interface states. This in turn suggests that the transport is not governed by variable range hopping activated in the 166 K to 100 K region, but must

instead be activated. Below 20 K there appears to be another transport regime, but the temperature range is too small to determine the mode of transport here.

The transport in this sample can be described as follows: At room temperature there is a high carrier concentration and the wire is quasi-metallic, as expected from the observations in Chapter 4. As the temperature is lowered the resistance initially falls due to the reducing phonon number. Eventually the carrier concentration is reduced and so the temperature rises exponentially down to a temperature of approximately 100 K. This is most likely due to the fact that the Fermi level is pinned 8 to 9 meV above the valence band as has been previously reported [15], and so mobile holes in the valence band freeze out at the temperature is lowered to 100 K. Below this temperature the carrier concentration is constant for the reasons discussed in Section 6.1.3. We now have a constant carrier concentration of free holes surrounded by a high density of trapped electrons that act as scattering centres. This displays the properties of a dirty metal, which persists down to 20 K.

References

[1] B.I. Shklovskii, A.L. Efros, Electronic properties of doped semiconductors, Moscow Izdatel Nauka, 1 (1979).
[2] N.W. Ashcroft, N.D. Mermin, Solid State Physics (Holt, Rinehart and Winston, New York, 1976), There is no corresponding record for this reference, (2005).
[3] N. Mott, Metal-Insulator Transitions, Taylor and Francis, New York, 1990.
[4] S.R. Elliott, The physics and chemistry of solids, Wiley, 1998.
[5] S.M. Sze, Physics of Semiconductor Devices, Wiley, New York, 1981.
[6] A.R. Goi, K. Syassen, M. Cardona, Direct-band-gap absorption in germanium under pressure, Physical Review B, 39 (1989) 12921-12924.
[7] B. Welber, M. Cardona, Y.-F. Tsay, B. Bendow, Effect of hydrostatic pressure on the direct absorption edge of germanium, Physical Review B, 15 (1977) 875-879.
[8] R.H. Kingston, Review of Germanium Surface Phenemena, Journal of Applied Physics, 27 (1956) 101.
[9] T. Hanrath, B.A. Korgel, Influence of Surface States on Electron Transport through Intrinsic Ge Nanowires, The Journal of Physical Chemistry B, 109 (2005) 5518-5524.

[10] J. Bardeen, Surface states and rectification at a metal semi-conductor contact, Physical Review, 71 (1947) 717.
[11] Y. Maeda, N. Tsukamoto, Y. Yazawa, Y. Kanemitsu, Y. Masumoto, Visible photoluminescence of Ge microcrystals embedded in SiO2 glassy matrices, Applied physics letters, 59 (1991) 3168-3170.
[12] J. Mitard, K. Martens, B. DeJaeger, J. Franco, C. Shea, C. Plourde, F. Leys, R. Loo, G. Hellings, G. Eneman, Impact of Epi-Si growth temperature on Ge-pFET performance, in: Solid State Device Research Conference, 2009. ESSDERC'09. Proceedings of the European, IEEE, 2009, pp. 411-414.
[13] A. Zabrodskii, K. Zinov'eva, Low-temperature conductivity and metal–insulator transition in compensate n-Ge, Zh. Eksp. Teor. Fiz, 86 (1984) 742.
[14] J. Bass, W.P. Pratt, P.A. Schroeder, The temperature-dependent electrical resistivities of the alkali metals, Reviews of Modern Physics, 62 (1990) 645-744.
[15] A. Dimoulas, P. Tsipas, A. Sotiropoulos, E.K. Evangelou, Fermi-level pinning and charge neutrality level in germanium, Applied Physics Letters, 89 (2006).
[16] C. Bryant, P. Keesom, Low-temperature specific heat of germanium, Physical Review, 124 (1961) 698.
[17] M. Hou, M. El Azzaoui, H. Pattyn, J. Verheyden, G. Koops, G. Zhang, Growth and lattice dynamics of Co nanoparticles embedded in Ag: A combined molecular-dynamics simulation and Mössbauer study, Physical Review B, 62 (2000) 5117-5128.
[18] L. Hong, C. Ahn, B. Fultz, The Debye temperature of nanocrystalline β–Sn measured by x-ray diffraction, Journal of materials research, 10 (1995) 2408-2410.
[19] M. Park, K. Savran, Y.J. Kim, Weak localization and the Mooij rule in disordered metals, physica status solidi (b), 237 (2003) 500-512.
[20] V.F. Gantmakher, Mooij rule and weak localization, JETP letters, 94 (2011) 626-628.
[21] M. Jonson, S.M. Girvin, Electron-Phonon Dynamics and Transport Anomalies in Random Metal Alloys, Physical Review Letters, 43 (1979) 1447-1451.
[22] Y. Imry, Possible Role of Incipient Anderson Localization in the Resistivities of Highly Disordered Metals, Physical Review Letters, 44 (1980) 469-471.
[23] M. Kaveh, N. Mott, Universal dependences of the conductivity of metallic disordered systems on temperature, magnetic field and frequency, Journal of Physics C: Solid State Physics, 15 (1982) L707.
[24] D. Belitz, W. Gotze, Defect-induced tunnelling and the conductivity of strongly disordered systems, Journal of Physics C: Solid State Physics, 15 (1982) 981.
[25] D. Belitz, W. Schirmacher, Transport theory for high-resistivity conductors, Journal of Non-Crystalline Solids, 61–62, Part 2 (1984) 1073-1078.
[26] N. Mott, Conduction in non-crystalline materials, Oxford University Press(UK), 1993, (1993) 157.
[27] A.M. Jayannavar, N. Kumar, Mooij correlation in disordered metals, Physical Review B, 37 (1988) 573-576.
[28] G.-L. Zhao, Y. He, W.Y. Ching, Theory of metallic glasses. II. Transport and optical properties, Physical Review B, 42 (1990) 10887-10898.

7. Conclusions and Future Work

The electrical characteristics of germanium nanowires grown without the use of a seed were examined in detail in this thesis. Self-seeded germanium nanowires have been proposed as an attractive growth method for future electronic devices due to the removal of complications associated with doping from the metallic seed in conventionally grown bottom up nanowires [1, 2]. It has been demonstrated that the electrical response is determined almost entirely by the details of the shell that form on these wires as a by-product of the growth process. This leads to a high level of unintentional doping which greatly reduce the ability to control the electrical response of these wires. In addition the high density of surface states leads directly to high scattering, causing the mobility in these wires to be 4 orders of magnitude lower than in bulk germanium. These low mobility values will prohibit the use of wires grown using this method in future electronic devices.

We have shown that the wires can display a wide variety of characteristics, from *p*-type doping with memristance, to highly doped quasi-metallic behaviours. Analysis of all the observed phenomena points towards the presence of electron traps at the interface between the core and the shell of the nanowire. The variation of device functionality is a direct result of a change in carrier concentration resulting from a difference in the shell morphology and composition caused by a change in the growth conditions of the wires. A very large density of surface states leads to the quasi-metallic behaviour observed, while a reduction in the number of surface states allows the *p*-type behaviour to emerge. A model is developed to explain the presence of an asymmetric curve with a memristive response resulting from the difference the transfer times into and out of the surface states.

The variation of the resistivity with diameter was also examined. The results are modelled and the effect of the electrons trapped at the interface is taken explicitly into account. It was found that upon shrinking from diameters of 40 nm to wires with diameters of 20 nm the resistivity of the wires fell by several orders of magnitude. Below this diameter monotonic behaviour is no longer seen and a peak-like feature in the resistivity for wires with diameters of around 14 nm is measured. The results are modelled and the effect of the surface states is taken explicitly into account. Two separate regimes are found.

For wires with diameters in excess of 20 nm we find that the free holes in the core of the wire exist predominantly in an annular region near to the core/shell interface, with a region devoid of charge carriers at the centre of the wire. For wires with diameters below 20 nm the holes exist throughout the nanowire core. In both regimes the carrier concentration increases due to the difference in scaling between the surface area and the volume in which the free holes are located. For wires with diameters below 20 nm we modelled the change in the hole mobility with diameter using the one-dimensional Kubo-Greenwood formula [3, 4]. The effect of doping solely from interface states both on the carrier concentration and on the mobility was included explicitly in this calculation for the first time. The results of the model suggest that the observed peak-like feature in the resistivity is a result of a competition between the aforementioned increasing carrier concentration and the decreasing mobility that is caused by increased scattering between states in smaller diameter nanowires. A change from regions of mobility-dominated resistivity increase to carrier concentration-dominated resistivity decrease leads to the observed peak-like feature in the resistivity. While good qualitative agreement is found between theory and

experiment, quantitative agreement is lacking. This is due primarily due to the fact that the wire is modelled as an infinite potential well to allow for the wavefunction to be found analytically. A more complete numerical calculation is required to give a more detailed description of the observed phenomena.

Finally we looked at the temperature dependence of the resistivity of the wires. It was found that in the highly resistive samples which showed a gate effect, the variation of the resistance with temperature suggested that the transport mechanism was Efros-Shklovskii variable range hopping, though the measureable temperature range was too small to conclusively rule out Mott variable range hopping. Further measurements either with an improved set up to allow measurement of smaller currents or to allow heating of the sample is required to experimentally determine the mechanism. The density of surface states extracted using the Efros-Shklovskii theory was in excellent agreement with the density of states found from transconductance measurements. The absence of activated transport in these wires indicates that the carriers are not derived from extrinsic dopants or excitation across the band gap. Rather the doping results from charge traps at the interface, in agreement with previous results. The most highly doped samples showed quasi-metallic behaviour, including decreasing resistivity with temperature above 200 K and a linear increase in the resistivity with temperature from 90 K to 20 K suggesting dirty metal behaviours. At intermediate temperatures activated transport is found, again underlining the difference between the two sets of samples. The results from both sets of samples reinforce the difference in the electrical response seen in the room temperature electrical measurements. Measurements to lower temperatures need to be made in order to determine the transport mechanism below 20 K.

The results in this thesis show that the control of the shell and in particular of the core/shell interface is essential to the production of functional devices based on self-seeded nanowires and shed light on the important role of interface states on the electrical properties of germanium nanowires. Work is needed primarily in three areas. Firstly a fuller analysis of the shell material should be undertaken. This should involve measuring wires grown with a greater range of growth conditions. In each case TEM images of the wires from that growth should be taken in an effort to quantify the density of germanium crystals in the shell and spectroscopic analysis should be performed to find the composition of the shell. This should be compared to the electrical results in order to better relate the properties of the hell to the electrical characteristics observed. Secondly the calculation should be carried out numerically. This would involve firstly solving the Schrödinger and Poisson's equations self-consistently. The results of this calculation should subsequently be used to calculate the momentum relaxation rates. Such a calculation would require rewriting the code entirely, but should yield better quantitative agreement with experiment.

References

[1] R.G. Hobbs, S. Barth, N. Petkov, M. Zirngast, C. Marschner, M.A. Morris, J.D. Holmes, Seedless growth of sub-10 nm germanium nanowires, Journal of the American Chemical Society, 132 (2010) 13742-13749.
[2] O. Lotty, R. Hobbs, C. O'Regan, J. Hlina, C. Marschner, C. O'Dwyer, N. Petkov, J.D. Holmes, Self-seeded growth of germanium nanowires: Coalescence and Ostwald Ripening, Chemistry of Materials, 25 (2013) 215-222.
[3] R. Kubo, Statistical-mechanical theory of irreversible processes. I. General theory and simple applications to magnetic and conduction problems, Journal of the Physical Society of Japan, 12 (1957) 570-586.
[4] D. Greenwood, The Boltzmann equation in the theory of electrical conduction in metals, Proceedings of the Physical Society, 71 (1958) 585.

Appendices

A. Derivation of the Kubo Formula

Let us rewrite Eq. 2.4 from the main text as [1]:

$$J_\alpha(\boldsymbol{r},t) = \sum_\beta \sigma_{\alpha\beta}(\boldsymbol{q},\omega)E_\beta(\boldsymbol{r},t). \quad \text{A. 1}$$

$$E_\alpha(\boldsymbol{r},t) = \Xi_\alpha e^{i(\boldsymbol{q}.\boldsymbol{r}-\omega t)} \quad \text{A. 2}$$

where $\alpha = x, y, z$ labels the direction of the applied field and $E_\alpha(\boldsymbol{r},t)$is the total field at a point $\boldsymbol{r}$ at a time t. $E_\alpha(\boldsymbol{r},t)$ contains contributions not only from any applied fields, but also the electric field within the crystal. Ξ_α is the magnitude of the field. It should be noted that the conductivity is constant in space and time, but is not the same at all wavelengths or frequencies of the field.

The Hamiltonian for the system is taken to be:

$$H + H' \quad \text{A. 3}$$

where H' contains the interaction between the total electric field and the particles in the system. The electric field is a vector potential, so we may write [1]:

$$H' = -\frac{1}{c}\int d^3r j_\alpha(\boldsymbol{r})A_\alpha(\boldsymbol{r},t) \quad \text{A. 4}$$

$$A_{\alpha(\boldsymbol{r},t)} = -\frac{ic}{\omega}E_\alpha(\boldsymbol{r},t), \quad \text{A. 5}$$

where c is the speed of light in vacuum, $j_\alpha(\boldsymbol{r})$ is the current operator, and $A_\alpha(\boldsymbol{r},t)$ is the vector potential. Putting A. 5 into A. 4 and using A. 2 we can write:

$$H' = \frac{i}{\omega}j_\alpha(\boldsymbol{q})\Xi_\alpha e^{-i\omega t} \quad \text{A. 6}$$

where $j_\alpha(\boldsymbol{q}) = \int d^3r j_\alpha(\boldsymbol{r},t)e^{i\boldsymbol{q}.\boldsymbol{r}}$ is the Fourier transform of the current operator.

The velocity vector of a particle i, $v_{i\alpha}$, depends on the momentum and the vector potential as [1]:

$$v_{i\alpha} = \frac{1}{m}\left(p_{i\alpha} - \frac{e}{c}A_\alpha(\boldsymbol{r}_i)\right). \quad \text{A. 7}$$

The current density in the direction α is found by summing the expectation value of the velocity of each particle, and multiplying by the charge divided by the volume (c.f. with Eq 2.3 in the main text):

$$J_\alpha(\boldsymbol{r},t) = \frac{e}{mV}\sum_i \langle p_{i\alpha}\rangle - \frac{e^2}{mcV}\sum_i A_\alpha(\boldsymbol{r}_i), \quad \text{A. 8}$$

where $p_{i\alpha}$ is the momentum operator of the particle i. The momentum operator is related to the current operator as $j_\alpha = ep_\alpha$/m. Using this fact and A. 5 we can rewrite A. 8 as:

$$J_\alpha(\boldsymbol{r},t) = \langle j_\alpha(\boldsymbol{r},t)\rangle + \frac{in_0e^2}{m\omega}E_\alpha(\boldsymbol{r},t) \quad \text{A. 9}$$

where we have replaced the sum over all particles divided by volume with the particle density, n_0.

The expectaiotn value of the current operator as a function of time is [1]:

$$\langle j_\alpha(\boldsymbol{r},t)\rangle = \langle \Psi'|e^{i(H+H')t}j_\alpha(\boldsymbol{r})e^{-i(H+H')t}|\Psi'\rangle, \quad \text{A. 10}$$

where Ψ' is the wavefunction of the full Hamiltonian, $H + H'$. We may now define an operator $U(t) = e^{iHt}e^{-i(H+H')t}$ which allows us to rewrite A. 10 as [1]:

$$\langle j_\alpha(\boldsymbol{r},t)\rangle = \langle \Psi'|U^\dagger(t)e^{iHt}j_\alpha(\boldsymbol{r})e^{-iHt}U(t)|\Psi'\rangle. \quad \text{A. 11}$$

[1] Note that $e^Ae^B = e^{A+B}$ only if $[A,B] = 0$. As it is not necessarily true that $[H,(H+H')] = 0$ we cannot simplify the propagator further.

The operator $U(t)$ is known as the propagator of the system. It can be shown that it may be written as [1]:

$$U(t) = Texp\left(-i\int_0^t dt' H'(t')\right), \qquad \text{A. 12}$$

where T is the time order operator and $H'(t) = e^{iHt}H'e^{-iHt}$. We now define the wavefunction $|\Psi\rangle$ as the wavefunction of the unperturbed Hamiltonian, H. It can be shown that the relationship between the wavefunctions of the perturbed and unperturbed system is [1]:

$$|\Psi'\rangle = Texp\left(-i\int_{-\infty}^0 dt' H'(t')\right)|\Psi\rangle. \qquad \text{A. 13}$$

Note that the limits of integration are different in A. 12 and A. 13. The operator given by A. 12 tells us how the system evolves in time, while the in the presence of the electric field. A. 13 simply says that to find the state of the system at the time $t = 0$ we must propagate the system from $t = -\infty$. From A. 12 and A. 13 we find:

$$\begin{aligned} U(t)|\Psi'\rangle &= Texp\left(-i\int_0^t dt' H'(t') - i\int_{-\infty}^0 dt' H'(t')\right)|\Psi\rangle \\ &= Texp\left(-i\int_{-\infty}^t dt' H'(t')\right)|\Psi\rangle. \end{aligned} \qquad \text{A. 14}$$

We now use the fact that we are only interested in the linear response of the system. We therefore Taylor expand the final term in A. 14 and keep only the terms linear in H'. This results in [1]:

$$U(t)|\Psi'\rangle = \left(1 - i\int_{-\infty}^t dt' H'(t')\right)|\Psi\rangle. \qquad \text{A. 15}$$

Substituting this back into A. 11 we can rewrite the right hand side as:

$$\langle\Psi|\left(1-i\int_{-\infty}^{t}dt'H'(t')\right)j_\alpha(\boldsymbol{r},t)\left(1-i\int_{-\infty}^{t}dt'H'(t')\right)|\Psi\rangle \qquad \text{A. 16}$$

where we have defined $j_\alpha(\boldsymbol{r},t)=e^{itH}j_\alpha(\boldsymbol{r})e^{-iHt}$. Multiplying this out and again keeping only terms linear in H' we find [1]:

$$\langle j_\alpha(\boldsymbol{r},t)\rangle=\langle\Psi|\left(j_\alpha(\boldsymbol{r},t)-i\int_{-\infty}^{t}dt'[j_\alpha(\boldsymbol{r},t),H'(t')]\right)|\Psi\rangle. \qquad \text{A. 17}$$

where $[a,b]=ab-ba$ is the commutator of a and b. The first term is the expectation value of the current in the α direction of the unperturbed system, and is assumed to vanish [1]:

$$\langle\Psi|j_\alpha(\boldsymbol{r},t)|\Psi\rangle=0. \qquad \text{A. 18}$$

Using A. 6 the commutator is found to be:

$$[j_\alpha(\boldsymbol{r},t),H'(t')]=\frac{i}{\omega}\Xi_\beta e^{-i\omega t}\left[j_\alpha(\boldsymbol{r},t),j_\beta(\boldsymbol{q},t')\right] \qquad \text{A. 19}$$

and then using A. 2 to substitute for Ξ_β we find:

$$[j_\alpha(\boldsymbol{r},t),H'(t')]=\frac{i}{\omega}E_\beta(\boldsymbol{r},t)e^{i\boldsymbol{q}.\boldsymbol{r}}e^{i\omega(t-t')}\left[j_\alpha(\boldsymbol{r},t),j_\beta(\boldsymbol{q},t')\right]. \qquad \text{A. 20}$$

Substituting this back into A. 17 and using A. 18 we find:

$$\begin{aligned}&\langle j_\alpha(\boldsymbol{r},t)\rangle\\&=\frac{1}{\omega}E_\beta(\boldsymbol{r},t)e^{-i\boldsymbol{q}.\boldsymbol{r}}\int_{-\infty}^{t}dt'e^{i\omega(t-t')}\langle\Psi|\left[j_\alpha(\boldsymbol{r},t),j_\beta(\boldsymbol{q},t')\right]|\Psi\rangle.\end{aligned} \qquad \text{A. 21}$$

Putting this equation back into A. 9 we find the final form for the current density:

$$J_\alpha(\boldsymbol{r},t) = \frac{1}{\omega}E_\beta(\boldsymbol{r},t)e^{-i\boldsymbol{q}.\boldsymbol{r}}\int_{-\infty}^{t} dt' e^{i\omega(t-t')}\langle\Psi|\big[j_\alpha(\boldsymbol{r},t), j_\beta(\boldsymbol{q},t')\big]|\Psi\rangle. + \frac{in_0e^2}{m\omega}E_\alpha(\boldsymbol{r},t) \quad \text{A. 22}$$

We can now factor out the electric field, which leaved us with an equation of the form of A. 1, allowing us to write the final expression for the conductivity [1]:

$$\sigma_{\alpha\beta}(\boldsymbol{q},\omega) = \frac{1}{\omega}e^{-i\boldsymbol{q}.\boldsymbol{r}}\int_{-\infty}^{t} dt' e^{i\omega(t-t')}\langle\Psi|\big[j_\alpha(\boldsymbol{r},t), j_\beta(\boldsymbol{q},t')\big]|\Psi\rangle. + \frac{in_0e^2}{m\omega}\delta_{\alpha\beta,} \quad \text{A. 23}$$

where the delta function ensures that the last term only plays a role when the current is in the same direction as the field, as required by A. 9. We must now average over the space variable $\boldsymbol{r}$ in order to eliminate atomic fluctuations. We do this by integrateing over the volume, d^3r and then dividing by the volume V [1]. The only terms affected are:

$$\frac{1}{V}\int d^3r\, e^{-i\boldsymbol{q}.\boldsymbol{r}} j_\alpha(\boldsymbol{r},t) = \frac{1}{V}j_\alpha(-\boldsymbol{q},t) = \frac{1}{V}j_\alpha^\dagger(\boldsymbol{q},t) \quad \text{A. 24}$$

The final step is to make the replacement $t - t' = t$, giving the final form of the Kubo formula, as given in Section 2.5 [1, 2]:

$$\sigma_{\alpha\beta}(\boldsymbol{q},\omega) = \frac{1}{\omega V}\int_0^\infty dt\, e^{i\omega t}\langle\psi\big|\big[j_\alpha^\dagger(\boldsymbol{q},t), j_\beta\,(\boldsymbol{q},0)\big]\big|\psi\rangle + i\frac{n_0e^2}{m\omega}\delta_{\alpha\beta}. \quad \text{A. 25}$$

References

[1] G.D. Mahan, Many-particle physics, Springer, 2000.
[2] R. Kubo, Statistical-mechanical theory of irreversible processes. I. General theory and simple applications to magnetic and conduction problems, Journal of the Physical Society of Japan, 12 (1957) 570-586.

B. No Energy Discharge from a Memristive System

In this appendix we wish to prove the statement that there is no energy discharge in a memristive system, which we made in Section 2.6. All of the arguments in this appendix are adapted from [1]. We start with the following definitions:

1. A memrisrive system is defined by: $v = R(x, i, t)i$, as in Eq 2.52 of the main text.
2. A memeristive system is passive.
3. The state variable $x(t)$ is a continuous function of t and the resistance $R(x, i, t)$ is a continuous function of x, i and t.
4. $R(x, i, t) = 0$ only when $i = 0$.

We will first prove that $R(x, i, t)$ is always positive. Let us define a state x^* which is the minimum energy state. That is to say that when the system is in the state x^* no energy can be extracted from the system by definition. Let us now assume that $R(x^*, i_0, t_0) < 0$ for some current, i_0 at some time t_0. Due to definition 3 we can now say that $R(x, i, t) < 0$ for some set of values for x, i and t near to x^*, i_0 and t_0. It will therefore be possible to construct a finite waveform $i(t)$, such that $R(x, i(t), t) < 0$ at all times. Total power dissipated by the memrisive system from a time t_0 to a time t is:

$$\int_{t_0}^{t} v(\tau)i(\tau)d\tau = \int_{t_0}^{t} R(x(\tau), i(\tau), \tau)\, i^2(\tau)d\tau. \qquad \text{Eq. B.1}$$

It can be seen that if $R(x, i, t)$ is negative that the total dissipated by the system is negative. That is to say that there has been a net output of energy from the memristive system. As we have assumed that we started in the minimum energy state this energy must come from an external source. This contradicts definition 2 that the memrisive

system is passive. We therefore conclude that if the system is in its minimum energy state $R(x^*, i, t) \geq 0$ for all i and t.

Now let us assume that the $R(x_A, i_A, t_A) < 0$ for an arbitrary x_A, i_A and t_A. The system can be evolved from the state $\{x^*, i_0, t_0\}$ to the state $\{x_A, i_A, t_A\}$ by the application of a current with a specific waveform. It is always possible to find a continuous waveform such that the sign of $i(t)$ does not change. This follows from the fact that the state variable x must be contineouos – if i changes sign dx/dt must also change sign, as discussed in Section 2.6 of the main text. Therefore by definition 4 $R(x, i, t)$ will not be equal to 0, as the system evolves from the minimum energy state to any other state, except possibly at the endpoints. As we have already proved that $R(x^*, i_0, t) \geq 0$ we can now say that $R(x_A, i_A, t) \geq 0$ due to the fact that $R(x, i, t)$ is continuous.

We have now proven that for any possible current when the system is in any possible state $R(x, i, t) \geq 0$. Therefore from Eq. B.1 the memristive system always dissipates energy, thus proving that there is no way to usefully extract stored energy from a memristive system.

References

[1] L.O. Chua, S.M. Kang, Memristive devices and systems, Proc. IEEE, 64 (1976) 209-223.

C.Solution of Schrödinger for an Infinite Cylindrical Well

The Schrödinger equations is cylindrical coordinates is [1, 2]:

$$-\frac{\hbar^2}{2m^*}\left(\frac{\partial^2\Psi(\mathbf{r})}{\partial \mathrm{r}^2}+\frac{1}{r}\frac{\partial\Psi(\boldsymbol{r})}{\partial r}+\frac{1}{r^2}\frac{\partial^2\Psi(\boldsymbol{r})}{\partial\theta^2}-\frac{\partial^2\Psi(\boldsymbol{r})}{\partial z^2}\right) = E\Psi(\boldsymbol{r}) \quad \text{Eq. C.1}$$

where $\hbar$ is Planck's reduced constant, and the wavefunction $\Psi(\boldsymbol{r})$ can be decomposed into its radial, $R(r)$, angular $\Theta(\theta)$, and longitudinal parts, $Z(z)$ as:

$$\Psi(\boldsymbol{r}) = R(r)\Theta(\theta)Z(z). \quad \text{Eq. C.2}$$

Putting Eq. C.2 into Eq. C.1 and multiplying across by $-r^2 2m^*/\hbar^2$ gives:

$$r^2\Theta(\theta)Z(z)\frac{\partial^2\mathrm{R(r)}}{\partial \mathrm{r}^2}+r\Theta(\theta)Z(z)\frac{\partial\mathrm{R(r)}}{\partial r}+\mathrm{R}(r)Z(z)\frac{\partial^2\Theta(\theta)}{\partial\theta^2} - r^2\mathrm{R(r)}\Theta(\theta)\frac{\partial^2\mathrm{Z(z)}}{\partial z^2} = -\frac{2r^2m^*}{\hbar^2}ER(r)\Theta(\theta)Z(z). \quad \text{Eq. C.3}$$

Dividing across by $\Theta(\theta)Z(z)$ and rearranging we find:

$$r^2\frac{\partial^2\mathrm{R(r)}}{\partial \mathrm{r}^2}+r\frac{\partial\mathrm{R(r)}}{\partial r} + \left(\frac{1}{\Theta(\theta)}\frac{\partial^2\Theta(\theta)}{\partial\theta^2} + r^2\left(\frac{1}{\mathrm{Z(z)}}\frac{\partial^2\mathrm{Z(z)}}{\partial z^2}-\frac{2m^*E}{\hbar^2}\right)\right)R(r) = 0. \quad \text{Eq. C.4}$$

We now realise that the first term in the brackets is the only term with dependence on θ and that the first term inside the second set of brackets is the only equation with a dependence on z. We may therefor write:

$$\frac{1}{\Theta(\theta)}\frac{\partial^2\Theta(\theta)}{\partial\theta^2} = -m^2, \qquad \text{Eq. C.5}$$

and

$$\frac{1}{\mathrm{Z(z)}}\frac{\mathrm{Z(z)}}{\partial z^2} = -k^2 \qquad \text{Eq. C.6}$$

where m and k are constants. These equations can be solved in the usual way to give:

$$\Theta(\theta) = \frac{e^{im\theta}}{\sqrt{2\pi}} \qquad \text{Eq. C.7}$$

and

$$Z(z) = \frac{e^{ikz}}{\sqrt{L}}, \qquad \text{Eq. C.8}$$

where L is the length is the wire. Returning now to Eq. C.4 we see that this is the defining equation of a Bessel function. The General solution is:

$$R(r) = AJ_m(Br), \qquad \text{Eq. C.9}$$

where A and B are constants to be determined by the boundary conditions and $J_m(r)$ is a Bessel function of the first kind. We note that mathematically Bessel functions of the second kind also solve the problem, but we reject them on physical grounds as they have a singularity at $r = 0$.

To determine B we use the fact that at the edge of the wire, $r = R$, the wavefunction must vanish as the potential goes to infinity at this point. This implies:

$$BR = j_{mn}, \qquad \text{Eq. C.10}$$

where j_{mn} is the nth 0 of the mth Bessel function. This gives:

$$B = \frac{j_{mn}}{R}. \qquad \text{Eq. C.11}$$

To find A we use the normalisation condition. We normalise the wavefunction over the cross sectional area of the cylinder. We write this as:

$$\int |R(r)\Theta(\theta)|^2 dA = 1. \qquad \text{Eq. C.12}$$

We now replace dA by $2\pi r dr$, using the fact that $A = 2\pi r^2$. We also realise from Eq. C.7 that $\Theta(\theta) = 1/2\pi$. Putting these equations and Eq. C.11 into the normalisation condition we find:

$$A^2 \int_0^R r J_m\left(\frac{j_{mn}r}{R}\right)^2 dr = 1. \qquad \text{Eq. C.13}$$

The solution to this integral is given by [3]:

$$A^2 \left[\frac{r^2}{4}\left(2J_m^2\left(\frac{j_{mn}r}{R}\right) - J_{m-1}\left(\frac{j_{mn}r}{R}\right)J_{m+1}\left(\frac{j_{mn}r}{R}\right) - J_{m+1}\left(\frac{j_{mn}r}{R}\right)J_{m-1}\left(\frac{j_{mn}r}{R}\right)\right)\right]_0^R = 1 \qquad \text{Eq. C.14}$$

which can be rearranged as:

$$A^2 \left[\frac{r^2}{2}\left(J_m^2\left(\frac{j_{mn}r}{R}\right) - J_{m-1}\left(\frac{j_{mn}r}{R}\right)J_{m+1}\left(\frac{j_{mn}r}{R}\right)\right)\right]_0^R = 1. \qquad \text{Eq. C.15}$$

Putting in the upper limit, $r = R$, we find that the squared Bessel function vanishes as j_{mn} is defined to be the zero of this function. With $r = 0$ the left hand side vanises due to the r^2 inside the square bracket. This gives:

$$\frac{-A^2R^2J_{m-1}(j_{mn})J_{m+1}(j_{mn})}{2} = 1. \qquad \text{Eq. C.16}$$

We now use the identity [3]:

$$J_{m+1}(j_{mn}) = -J_{m-1}(j_{mn}), \qquad \text{Eq. C.17}$$

to solve Eq. C.16 to find A:

$$A = \frac{\sqrt{2}}{RJ_{m+1}(j_{mn})}. \qquad \text{Eq. C.18}$$

Putting A from Eq. C.18 and B from Eq. C.11 back into Eq. C.9 we find the final expression for $R(r)$ to be:

$$R(r) = \frac{\sqrt{2}}{RJ_{m+1}(j_{mn})}J_m\left(\frac{j_{mn}r}{R}\right)$$

which is the same as Eq 5.9 in the main text.

We note that the normalisation factor is proportional to R^{-1} and not $R^{-1/2}$ as is often the case for component parts of the total wavefunction. This is necessary to ensure that the units of the total wavefunction are correct. The unit of $Z(z)$ is $[m]^{-1/2}$, but $\Theta(\theta)$ is dimensionless. $R(r)$ must therefore have the units of $[m]^{-1}$ in order to ensure that $\Psi(\boldsymbol{r})$ has the units of $[m]^{-3/2}$. Looked at a different way we can say that there is a factor of $R^{-1/2}$ in the normalisation factor for every dimension of confinement. So long as cylindrical symmetry is assumed there is no way to confine the electron any further in the θ direction, the electron is always free to move through the full circle. As we are working in 3 dimensions there must be 3 degrees of confinement. One is along the length, as characterised by $Z(z)$ and the other two must both be contained in $R(r)$, leading to the $R^{-1} = \left(R^{-\frac{1}{2}}\right)^2$ term in the normalisation factor.

References

[1] J. Hattori, S. Uno, K. Nakazato, N. Mori, Scaling consideration and compact model of electron scattering enhancement due to acoustic phonon modulation in an ultrafine free-standing cylindrical semiconductor nanowire, Journal of Applied Physics, 107 (2010) 033712-033712-033717.
[2] S. Jin, M.V. Fischetti, T. Tang, Modeling of electron mobility in gated silicon nanowires at room temperature: Surface roughness scattering, dielectric screening, and band nonparabolicity, Journal of Applied Physics, 102 (2007) 083715-083715-083714.
[3] M. Abramowitz, I.A. Stegun, Handbook of mathematical functions, Dover New York, 1972.

D. Derivation of Momentum Relaxation Rate due to Phonon Scattering

Let us first define the collision integral S as [1]:

$$S_m(k) = \sum_{n,k'} \Gamma_{nm}(\boldsymbol{k},\boldsymbol{k}')f_m(k)\big(1 - f_n(\boldsymbol{k}')\big) - \Gamma_{mn}(\boldsymbol{k}',\boldsymbol{k})f_n(\boldsymbol{k}')(1 - f_m(\boldsymbol{k})) \quad \text{Eq. D.1}$$

where $\Gamma_{nm}(\boldsymbol{k},\boldsymbol{k}')$ is the probability of scattering from state in the subband n with a wave-vector $\boldsymbol{k}$ to a state in the subband m with a wavector $\boldsymbol{k}'$, and $f_m(\boldsymbol{k})$ is the distribution function for carriers in the subband m at a wave-vector of $\boldsymbol{k}$ [1].This equation simply states that rate of change of the density of a state $\boldsymbol{k}$ in the subband m is equal to the number of carriers scattering into the state minus the number that are scattering out. In equilibrium Eq. D.1 must be equal to 0 for all values of $\boldsymbol{k}$. It therefore follows that [1]:

$$\Gamma_{nm}(\boldsymbol{k},\boldsymbol{k}')f_m^0(\boldsymbol{k})\big(1 - f_n^0(\boldsymbol{k}')\big) = \Gamma_{nm}(\boldsymbol{k})f_n^0(\boldsymbol{k}')\big(1 - f_m^0(\boldsymbol{k})\big), \quad \text{Eq. D.2}$$

where $f_m^0(k)$ is the equilibrium distribution function. We now assume that the system is close to equilibrium so that we may write the distribution function as [1]:

$$f_m(\boldsymbol{k}) = f_m^0(\boldsymbol{k}) + \delta f_m(\boldsymbol{k}). \quad \text{Eq. D.3}$$

Putting Eq. D.3 into Eq. D.1 and using Eq. D.2 it can be shown that [1]:

[1] In the main text the subbands were labelled i and i', We switch to n and m here to avoid confusion with the complex number $i = \sqrt{-1}$ which we will need later on.

$$S_m(\boldsymbol{k}) = \sum_{n,k'} \Gamma_{mn}(\boldsymbol{k}, \boldsymbol{k}') \left(\frac{f_m^0(\boldsymbol{k})}{f_n^0(\boldsymbol{k}')} \delta f_n(\boldsymbol{k}') - \frac{1 - f_n^0(\boldsymbol{k}')}{1 - f_m^0(\boldsymbol{k})} \delta f_m(\boldsymbol{k}) + \frac{f_n^0(\boldsymbol{k}') - f_m^0(\boldsymbol{k})}{f_n^0(\boldsymbol{k}')\left(1 - f_m^0(\boldsymbol{k})\right)} \delta f_n(\boldsymbol{k}') \delta f_m(\boldsymbol{k}) \right). \quad \text{Eq. D.4}$$

To find the momentum relaxation rate we must multiply $S_m(\boldsymbol{k})$ by the momentum in every state and sum over all states [1]. That is:

$$\frac{dp(\boldsymbol{k})}{dt} = \sum_{m,k} p_m(\boldsymbol{k}) S_m(\boldsymbol{k}). \quad \text{Eq. D.5}$$

In the relaxation time approximation this is equal to:

$$\frac{dp(\boldsymbol{k})}{dt} = -\frac{p(\boldsymbol{k})}{\tau_m(\boldsymbol{k})} \quad \text{Eq. D.6}$$

where $\tau_m(\boldsymbol{k})$ is the momentum relaxation time that we are looking for. Putting in Eq. D.4 to Eq. D.5 we find and again using Eq. D.2 we find [1]:

$$\frac{dp(\boldsymbol{k})}{dt} = \sum_{mn,k,k'} [p(\boldsymbol{k}') - p(\boldsymbol{k})] \Gamma_{mn} \frac{1 - f_n^0(\boldsymbol{k}')}{1 - f_m^0(\boldsymbol{k})} \delta f_m(\boldsymbol{k}). \quad \text{Eq. D.7}$$

The other terms cancel due to the fact that we are including both the scattering from $\boldsymbol{k}$ to $\boldsymbol{k}'$ and from $\boldsymbol{k}'$ to $\boldsymbol{k}$ within each subband. The numerator in the final term will be equal and opposite for these two cases and so cancel when we add them [1].

We now use the test particle approximation by setting $\delta f_n(\boldsymbol{k}) = \delta_{\boldsymbol{k},\boldsymbol{k_0}}$ [1], where $\delta_{\boldsymbol{k},\boldsymbol{k_0}}$ is the Kronikar delta and $\boldsymbol{k_0}$ is the initial wave-vector of the test particle. Putting this into Eq. D.7 it follows that [1]:

$$\tau_m(\boldsymbol{k})^{-1} = \sum_{n,k'} \Gamma_{mn} \left[1 - \frac{\boldsymbol{k}'}{\boldsymbol{k}}\right] \frac{1 - f_n^0(\boldsymbol{k}')}{1 - f_m^0(\boldsymbol{k})} \qquad \text{Eq. D.8}$$

where we have used Eq. D.6.

To determine the scattering rate of both acoustic and optical phonons first order perturbation theory is used [2, 3]. That is to say that the phonon is assumed to add a small term to the Hamiltonian, H_{Ph} which gives rise to the scattering. The main assumption is that this term is small compared to the Hamiltonian of the rest of the system. Perturbation theory gives rise to Fermi's golden rule [2, 3]:

$$\Gamma_{nm}(\boldsymbol{k}, \boldsymbol{k}') = \frac{2\pi}{\hbar} |M_{nm}(\boldsymbol{k}, \boldsymbol{k}')|^2 \delta\left(E_{\boldsymbol{k}} - E_{\boldsymbol{k}'} \pm \hbar\omega_q\right), \qquad \text{Eq. D.9}$$

where $\hbar$ is Planck's reduced constant, $M_{nm}(\boldsymbol{k}, \boldsymbol{k}')$ is the scattering matrix, $\hbar\omega_q$ is the energy of the scattering phonon and the delta function ensures energy conservation. The next two sections shall show the derivation of the scattering rate from Eq. D.9 and the momentum relaxation rate from Eq. D.8 for acoustic phonons in Section C. 1 and optical phonons in Section C. 2 .

C. 1 Acoustic phonon scattering.

We are now going to derive the momentum relaxation time for carriers in a one-dimensional channel. We will assume that he carriers are confined in the y and z directions and free in the x direction. As such we will drop the vector notation for $\boldsymbol{k}$ and use k_x from now on. The perturbing Hamiltonian for acoustic phonon scattering is [2, 4-6]:

$$H_{AC} = \mathrm{E}_1 \boldsymbol{\nabla}.\boldsymbol{u} \qquad \text{Eq. D.10}$$

where E_1 is the average deformation potential and $\boldsymbol{u}$ is the displacement vector. This gives rise to the matrix element for acoustic phonon scattering [4]:

$$\begin{aligned} & M_{AC}(k_x, k_x') \\ & = qE_1^2 \sqrt{\left(\frac{\hbar}{2\rho_{Ge} V \omega_q}\right)\left(N_q + \frac{1}{2} \mp \frac{1}{2}\right)} \\ & \times \int\int \left[\psi_i(x,y) e^{i(q_y y + q_z z)} \psi_{i'}(x,y)\right] dy dz \\ & \times \frac{1}{L_x} \int e^{i(k_x - k_x' \pm q_x)x} dx, \end{aligned} \qquad \text{Eq. D.11}$$

ρ_{Ge} is the density of germanium, V is the volume of the sample, N_q is the phonon number, and $\psi_n(x,y)$ is the x and the y components of the wavefunction of the charge carrier.

The number of phonons is given by the Bose Einstein distribution function :

$$N_q = \frac{1}{e^{\frac{\hbar\omega_q}{k_B T}} - 1} \qquad \text{Eq. D.12}$$

where k_B is Boltzmann's constant and T is the temperature. The energy of an acoustic phonon is close to zero at the Brillion zone centre. In the limit as $\hbar\omega_q \to 0$ the number of phonons goes to infinity and we may write after Taylor expanding the exponential [2, 4]:

$$N_q \approx N_q + 1 \approx \frac{k_B T}{\hbar\omega_q}. \qquad \text{Eq. D.13}$$

Near to the zone centre the dispersion is approximately linear and is well approximated by [4, 7]:

$$\omega_q = uq \qquad \text{Eq. D.14}$$

where u is the speed of sound in the material. We now define the overlap integral to be [4]:

$$I_{nm}(q_y, q_z) = \int\int \left[\psi_i(x,y) e^{i(q_y y + q_z z)} \psi_{i'}(x,y)\right] dydz. \qquad \text{Eq. D.15}$$

Putting Eq. D.13 to Eq. D.15 into Eq. D.11, performing the integral over x and and taking the absolute value squared gives [4]:

$$|M(\boldsymbol{k}, \boldsymbol{k}')|^2 = \frac{E_1^2 k_B T}{2\rho_{Ge} V u^2} \left|I_{nm}(q_y, q_z)\right|^2 \delta(k_x - k_x' \pm q_x). \qquad \text{Eq. D.16}$$

Putting this into Eq. D.9 and integrating over all possible final states gives the scattering rate [4]:

$$\Gamma_{nm}^{AC}(k_x, k_x') = \frac{2\pi E_1^2 k_B T}{\hbar \rho_{Ge} V u^2} \int\int \left|I_{nm}(q_y, q_z)\right|^2 \left(\frac{dq_y dq_z}{4\pi^2}\right) \times \int \delta(k_x - k_x' + q_x)\delta(E_n - E_m) \frac{dk_x'}{2\pi}. \qquad \text{Eq. D.17}$$

Using Eq. D.15 and the fact that:

$$\frac{1}{2\pi} \int dq_y e^{iq_y y} = \delta(y). \qquad \text{Eq. D.18}$$

we can rewrite the double integral in Eq. D.17 as [4]:

$$\int\int \left|I_{nm}(q_y, q_z)\right|^2 \left(\frac{dq_y dq_z}{4\pi^2}\right) = \int\int |\psi_n(y,z)|^2 |\psi_m(y,z)|^2 dydz. \qquad \text{Eq. D.19}$$

We now use the fact that $\psi(x,y)$ is the same as $\psi(r,\theta) = R(r)\Theta(\theta)$ from the main text. Both are just the total wavefunction divided by its longitudinal part. Next we note that he double integral over dy and dz is equivelnt to a single integral over the area, $dA = dydz$. Putting all this back into Eq. D.19 gives:

$$\int |R_n(r)\Theta_{\rm n}(\theta)|^2 |R_m(r)\Theta_{\rm m}(\theta)|^2 dA. \qquad \text{Eq. D.20}$$

$R_n(r)$ is given by Eq 5.9 in the main text, and it can also be shown that:

$$\Theta_n(\theta) = \frac{1}{\sqrt{2\pi}} e^{in\theta}. \qquad \text{Eq. D.21}$$

If we assume a cylindrical wire the cross sectional area is given by: $A = \pi r^2$. Differentiating this we find $dA = 2\pi r dr$. Using this and Eq. D.21 we can write Eq. D.20 as:

$$F_{nm} = \frac{1}{2\pi} \int R_n(r)^2 R_m(r)^2 r dr \qquad \text{Eq. D.22}$$

This is the form factor for scattering from a state n to a state m given as Eq 5.12 in the main text [8].

We rewrite the final integral in Eq. D.17 as an integral over energy, using the definition of the density of states given in Section 2.2.5 of the main text:

$$\begin{aligned} &\int \delta(k_x - k_x' + q_x)\delta(E_n - E_m)\frac{dk_x'}{2\pi} \\ &\qquad = \frac{1}{2\pi}\int \delta(k_x - k_x' + q_x)\delta(E_n - E_m) V g_m(E') dE \\ &\qquad = \frac{V g_m(E)}{2\pi} \end{aligned} \qquad \text{Eq. D.23}$$

Finally putting Eq. D.22 and Eq. D.23 into Eq. D.17 and summing over all the final states leads to the rate of scattering out of state n:

$$\Gamma_n^{(AC)} = \frac{\pi E_1^2 k_B T}{2\hbar \rho_{Ge} u^2} \sum_m g_m(E) F_{nm}. \qquad \text{Eq. D.24}$$

We now use Eq. D.8 to find the momentum relaxation time. We first realise that for a given k_x in a given subband there will be a well-defined energy. We can therefore

replace $f_m^0(k)$ with $f(E)$. As we are assuming that the energy of the acoustic phonons is 0 the energy of the initial and final states must be equal. The final term in Eq. D.8 is then:

$$\frac{1-f(E)}{1-f(E)}=1. \qquad \text{Eq. D.25}$$

For acoustic phonons only backscattering is taken into account, $k_x \to -k_x{}'$, giving [8]:

$$1-\frac{k_x'}{k_x}=2. \qquad \text{Eq. D.26}$$

Putting Eq. D.24 to Eq. D.26 into Eq. D.8 gives the momentum relaxation time as [8]:

$$\frac{1}{\tau_n^{(AC)}}=\frac{\pi E_1^2 k_B T}{\hbar \rho_{Ge} u^2}\sum_m g_m(E)F_{nm}. \qquad \text{Eq. D.27}$$

which is the same as Eq. 5.11 in the main text with i and i' replaced by n and m.

C. 2 Optical Phonon Scattering

For optical phonon scattering the perturbing Hamiltonian is given by [2, 4-6]:

$$H_{op}=(DK)\boldsymbol{e_q}.\boldsymbol{u} \qquad \text{Eq. D.28}$$

where DK is the average deformation potential for optical phonons and $\boldsymbol{e_q}$ is the polarisation vector. This leads to a matrix element of [4]:

$$M_{op}(k_x,k_x')=DK\sqrt{\frac{\hbar}{2\rho_{Ge}V\omega_0}}\left(N_{op}+\frac{1}{2}\pm\frac{1}{2}\right)^{\frac{1}{2}} \times I_{nm}(q_x,q_y)\delta(k_x-k_x'\pm q_x). \qquad \text{Eq. D.29}$$

Optical phonons do have a significant energy at the zone centre [7]. It is usual to assume that it is dispersion less and to write that the energy is $\hbar\omega_0$, where ω_0 is a

constant. That is what is done in this case [4]. This also means that we can no longer use the approximation given by Eq. D.13. With these changes the steps in deriving the scattering rate are exactly the same as in the acoustic case, and so we will simply give the answer here:

$$\Gamma_n^{(op)} = \frac{\pi(DK)^2}{2\rho_{Ge}\omega_{op}} \sum_m g_m\left(E \pm \hbar\omega_{op}\right) F_{nm} \left(N_{op} + \frac{1}{2} \mp \frac{1}{2}\right). \qquad \text{Eq. D.30}$$

As the phonons now have energy Eq. D.25 no longer holds and we must write:

$$\frac{1 - f(E')}{1 - f(E)} = \frac{1 - f(E - \hbar\omega_0)}{1 - f(E)}. \qquad \text{Eq. D.31}$$

Putting this into Eq. D.8 along with Eq. D.30 gives the final result [8]:

$$\frac{1}{\tau_n^{(op)}(E)} = \frac{\pi(DK)^2}{2\rho_{Ge}\omega_{op}} \sum_m g_m\left(E \pm \hbar\omega_{op}\right) \times \frac{F_{nm}\left(1 - f\left(E \pm \hbar\omega_{op}\right)\right)}{1 - f(E)} \left(N_{op} + \frac{1}{2} \mp \frac{1}{2}\right). \qquad \text{Eq. D.32}$$

References

[1] N. Bannov, V. Aristov, V. Mitin, M. Stroscio, Electron relaxation times due to the deformation-potential interaction of electrons with confined acoustic phonons in a free-standing quantum well, Physical Review B, 51 (1995) 9930.
[2] D.K. Ferry, S.M. Goodnick, Transport in nanostructures, Cambridge university press, 1997.
[3] D. Ferry, Semiconductor transport, CRC Press, 2000.
[4] E. Ramayya, D. Vasileska, S. Goodnick, I. Knezevic, Electron transport in silicon nanowires: The role of acoustic phonon confinement and surface roughness scattering, Journal of Applied Physics, 104 (2008) 063711-063711-063712.
[5] M.V. Fischetti, S.E. Laux, Band structure, deformation potentials, and carrier mobility in strained Si, Ge, and SiGe alloys, Journal of Applied Physics, 80 (1996) 2234-2252.
[6] P. Lawætz, Low-field mobility and galvanomagnetic properties of holes in germanium with phonon scattering, Physical Review, 174 (1968) 867.
[7] N.W. Ashcroft, N.D. Mermin, Solid State Physics (Holt, Rinehart and Winston, New York, 1976), There is no corresponding record for this reference, (2005).

[8] R. Kotlyar, B. Obradovic, P. Matagne, M. Stettler, M. Giles, Assessment of room-temperature phonon-limited mobility in gated silicon nanowires, Applied physics letters, 84 (2004) 5270-5272.